UNIVERSIDAD DE CANTABRIA
Departamento de Física Moderna

y

C.S.I.C. - U.C.
Instituto de Física de Cantabria

Fenómenos Complejos en sistemas extendidos en el espacio

Marta Sánchez de La Lama
Tesis doctoral
2009

UNIVERSIDAD DE CANTABRIA
Departamento de Física Moderna

y

C.S.I.C. - U.C.
Instituto de Física de Cantabria

Fenómenos Complejos en sistemas extendidos en el espacio

Memoria presentada por la Licenciada
Marta Sánchez de La Lama
para optar al título de Doctor en Ciencias Físicas

Realizada bajo la supervisión del
Dr. **Juan Manuel López Martín**
2009

Dr. Juan Manuel López Martín, Científico titular del Consejo Superior de Investigaciones Científicas, certifica:

> Que la presente Memoria, titulada **"Fenómenos Complejos en sistemas extendidos en el espacio"**, ha sido realizada, bajo mi dirección, por Marta Sánchez de La Lama, y constituye su Tesis para optar al grado de Doctor por la Universidad de Cantabria. Asimismo emito mi conformidad para que dicha memoria sea presentada y tenga lugar, posteriormente, la correspondiente lectura.

Santander, a 20 de Abril de 2009

Fdo.: Dr. Juan Manuel López Martín

A mi familia.

Agradecimientos

Ante todo, quiero agradecer a Juanma, el director de esta Tesis, su dedicación y su tiempo. Me ha enseñado y me ha guiado a lo largo del proceso. También quiero dar las gracias a Horacio, José y Miguel. Trabajar con todos ellos ha sido un verdadero privilegio. Gracias también al resto de los integrantes del grupo de Física Estadística y No Lineal del IFCA y, en especial, a los compañeros y amigos del día a día del despacho S-114.

Agradecer también a todas aquellas personas que este doctorado me ha brindado la oportunidad de conocer, tanto en el ámbito profesional como personal, en trabajos de colaboración y durante estancias, escuelas y congresos.

Gracias también a los amigos: a los Físicos, a los históricos, a los viajeros, a las amigas que son como una piña (de la cual tengo la suerte de formar parte) y, cómo no, a las buenas amigas en la distancia.

A Mikel, que a lo largo de estos años me ha acompañado en los distintos momentos, y es casi como si él hubiera hecho también un poquito de esta Tesis.

A mis hermanos, porque seguimos formando un buen equipo aunque estemos distribuidos a lo largo y ancho de la Península (y a veces mucho más lejos).

Y, por supuesto, a mis padres. Que me han acompañado, me han apoyado y han sido- y seguirán siendo siempre- un punto de referencia.

Finalmente, agradecer al Ministerio de Ciencia e Innovación (España) la concesión de la beca de Formación de Profesorado Universitario (AP-2004-5118) para la realización de la presente Tesis doctoral.

Complex Phenomena in spatially extended systems

A dissertation submitted in partial fulfillment of the
requirements for the degree of Philosophy Doctor in Physics

by

Marta Sánchez de La Lama

Departamento de Física Moderna
Universidad de Cantabria
&
Instituto de Física de Cantabria
Consejo Superior de Investigaciones Científicas-Universidad de Cantabria

2009

Contents

CHAPTER

1

Complex Systems

1.1 More is different

This Thesis deals with different systems- interfaces in random media, social models, and complex networks- that, at first glance, have nothing to do with each other. What may an expanding oil stain, a discussion group of individuals, or the Internet network have in common? Apparently very little. However, a closer look reveals that all of them are dynamical systems with a large number of discrete units (molecules, agents, and routers). The microscopical interactions between such many elements make these systems to develop a level of organization often reflected as certain structure on scales much larger than that of their individual components. This effect gives rise to emergent properties of the whole system that fall into the realm of the *Physics of Complex Systems*.

Complexity may be defined as the global behavior of many interacting units that evolve toward self-organized steady states whose properties are largely independent of the interaction details. Nonlinear interactions are responsible for this coherent collective behavior, or *emergent properties*, that cannot be described at the level of the individual units. In this sense the whole is more than the sum of its parts- a characteristic shared with other nonlinear systems. This point of view was first exposed in the famous article of P.W. Anderson , titled ”More is different” [Anderson 1972], which had a deep impact in the development of complexity ideas and in the way scientists tackle the analysis of *many-particle* systems.

In his paper Anderson questioned the generality of the *reductionistic approach*, that considers simple systems to analyze them in detail focusing on their constituent elements. According to this traditional point of view, the fundamental laws are only those associated with elementary particles. The reductionistic vision can be certainly applied to a great deal of situations but it necessarily assumes the existence of characteristic scales: the size of an atom, of a molecule or of some macroscopic object. However, there are many situations in which the knowledge of the individual elements is not sufficient to characterize the properties of the whole system. As previously pointed out, when many elements interact in a nonlinear way, they can lead to complex structures and fundamental laws which cannot be directly related to the individual elements. This phenomenon is rooted in at the hierarchical organization of Nature, which gives rise to collective emergent properties every time one moves from a level of the hierarchy to the next one. Examples of these various levels can be quarks and nucleus, atoms, molecules, proteins, the emergence of life and on up to the macroscopic scales and the entire universe. The idea is that each discipline (particle physics, nuclear physics, molecular physics, and so on) refers to the step between one level and the next one. In this process, the essential concepts are the basic elements and their interactions. These lead to emergent properties and collective behaviors that cannot be identified from the original elements. From these collective properties one can then identify the basic elements of the next level of the hierarchy, and each of these steps is characterized by its own fundamental laws. Therefore, there are no absolute fundamental laws which, starting form the smallest scale, permit the derivation of all the other properties at all other scales. In this perspective, the various scientific disciplines become part of the same global system with much more possibilities to be integrated among them.

1.2 Scaling and Universality

The science of Complexity arises naturally from Statistical Mechanics which, in the late 1960s, introduced a fundamental change of paradigm with respect to the reductionistic scientific vision. It was in the context of critical systems where the first manifestations of complexity were observed and mathematically described. At the equilibrium point between order and disorder one can observe fluctuations at all scales that cannot be explained at the level of elemental components; the system cannot be described any more with the usual formalism, in which one tries to write simple equations for average quantities. During this conceptual revolution many new ideas were developed: *scaling*, *renormalization group*, *fractal geometry*, and *universality*.

The scaling hypothesis, originally proposed by Widom, Domb and Hunter [Widom 1965, Domb and Hunter 1965] basically tell us that the lack of any characteristic length scale at criticality (observed later in many other complex systems) implies a power law functional form for some of the magnitudes that characterize the system behavior. Strictly speaking, the original statement of the hypothesis asserts that the thermodynamical potentials and their derivatives are *generalized homogeneous functions* in the proximities of the critical point. This assumption leads to several *scaling laws* that relate the various critical exponents and to *scaling functions* in which data from very different systems- sharing some common global properties (symmetries and dimensionality)- collapse.

The predictions of the Scaling Theory were confirmed and expanded later by the *Renormalization Group Theory*, a rigorous conceptual construction from the mathematical point of view developed by Wilson and Fisher [Wilson and Kogut 1974, Fisher 1974] [1]. Basically, RG works by changing the length scale of the system by removing degrees of freedom and considering that the properties of the system remain unaltered. This leads to a systematic procedure to obtain the scaling functions and exponents at criticality. More recently, these general principles of scale invariance have proved useful in interpreting not only critical systems but a number of other complex phenomena. The concepts of scaling and universality are now applied to several complex systems that exhibit universal properties independently of the specific form of their interactions. Topics of research are not restricted to physical systems, but also include other fields as complex social, economic, and biological systems.

1.3 The extent of Complexity

Complex Systems research tries to discover the nature of the emerging behavior of complex systems, basically derived from the non-linear interaction of their many constituent elements. Such individual components may be atoms or macromolecules in a physical or biological context, but also people, machines or companies in a socio-economic context.

More than a new scientific discipline, the physics of Complex Systems provides a change of perspective in dealing with collective phenomena observed in Nature.

---

[1] These references are probably the most influential early reviews on Renormalization Group Theory. Other interesting reviews antedating Renormalization Group concepts are [Kadanoff et al. 1967, Stanley 1971].

Emergent behavior can be identified not only in physical systems but also in many other systems, from Ecology to the immune system, from social behavior to Economics. To provide a rapid perspective of the extent of Complexity, we enumerate here some examples which may appear, in principle, far away from physics.

Earthquakes

Because of convective flow generated from internal fission processes, the tectonic plates that compose the outermost layer of the Earth suddenly stick and slip giving rise to events commonly known as earthquakes. This stick-slip response of the Earth's crust is highly non-linear and gives rise to earthquakes that have no characteristic size. The duration of an earthquake varies from fractions of a second to minutes, and the relative displacement of the tectonic plates can be of the order of centimeters to metres. The annual number of events with a size S larger than a given size is consistent with a power-law decay $N(S > s) \propto s^{-B}$, with $B \approx 0.95$. This is the famous Gutenberg-Richter law for the earthquake-size frequency [Gutenberg and Richter 1944].

Cosmic structures

In Cosmology, the standard theories of structure formation describe the early universe as a homogeneous and isotropic distribution of matter whose fluctuations gave rise, through a complex dynamical evolution, to the emergence of a scale-free distribution of matter. The smooth microwave background radiation observed at large scales is considered as a trace of the initial conditions from which complex cosmic structures have emerged through gravitational dynamics. On smaller scales, evidences of an heterogeneous and correlated distributions of matter have been observed. Galaxy structure is just an example. Early angular surveys and more recent three dimensional maps evidence regions with a high concentration of galaxies and also some randomly distributed areas, called *voids*, which are almost empty [*cf.* Fig. 1.1]. This fractal galaxy distribution can be described in terms of the radial density $N(< R) \propto R^D$, where $N(< R)$ is the average number of galaxies within radius R from a given galaxy. The exponent D has been measured by several authors, with $D \approx 1.2 - 2.2$ [Guzzo et al. 1991], $D \approx 2.25 - 2.77$ [Martínez and Coles 1994], $D \approx 2$ [Labini et al. 1996], and $D \approx 2.93$ [Scaramella et al. 1998].

Financial markets

Financial markets are complex dynamical systems with many interacting elements that can be grouped into two categories: *traders*- such as investors, firms,

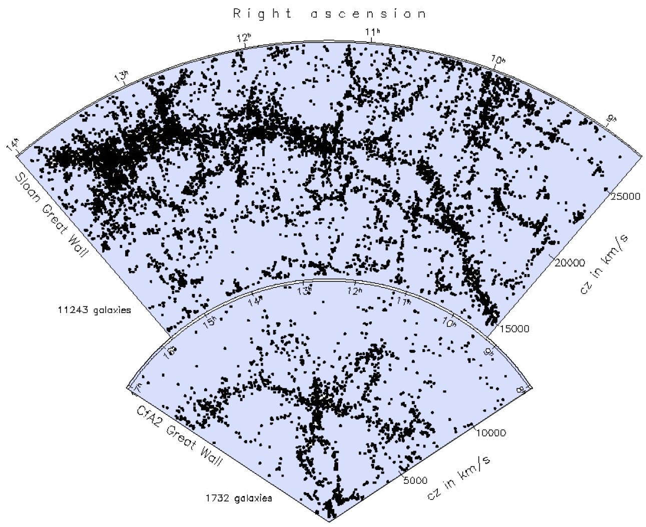

Figure 1.1: Galaxy distribution of the SLOAN (*top*) and CfA2 Great Walls, the first and second largest known super-structures in the Universe, respectively. The *red-shift* distances are determined by Hubble's law (given by $cz/100\ Mpc/h$) and angular distances across the sky are measured by *right ascension*. A proportional breadth of *declination*, the second angular coordinate, is considered for each slice. Scale invariance is evidenced as both structures exhibit the same statistical properties, challenging the traditional conjeture of a homogeneous distribution of matter. After Ref. [Pietronero and Labini 2004].

banks- and *assets*- such as stocks, futures and options. Interactions between these elements are highly non-linear and generate large fluctuations in observables as the stock price, trading volume, and the number of trades. The analysis of extensive financial databases shows that such fluctuations are well described by power-law functions whose exponents are similar for different types and sizes of market trends and even for different countries [Stanley et al. 1996, Liu et al. 1999, Takayasu and Takayasu 2003]. The emergence of this universal behavior is in contradiction to the "Efficient Market Hypothesis", traditionally evoked in economics [Fama 1970], which assumes that the movements of financial prices are an immediate and unbiased reflection of incoming news about future earning prospects. However, this hypothesis could be still valid considering that the emergence of scaling in financial markets

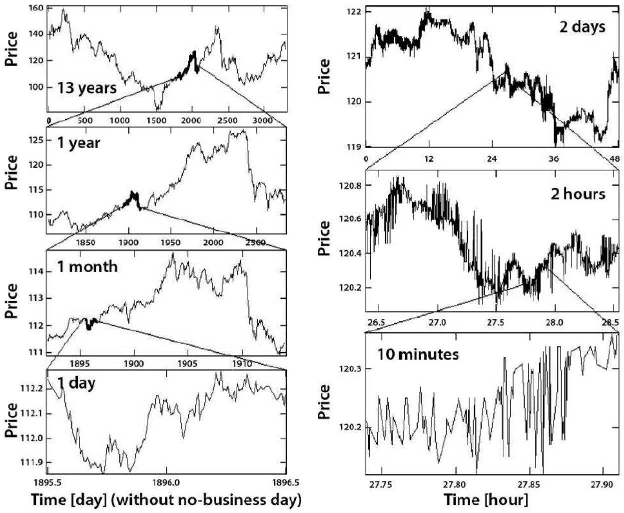

Figure 1.2: Example of scale invariance in financial data. The panels show the exchange rate Yen/USD variation for various time scales. Up to the time scale of hours, the panels show similar behavior, but this self-similarity changes drastically at every short times (minute scale of right panel at bottom). From Ref. [Pietronero 2008].

would simply reflect similar scaling in the *input* signals that the traders manage during their mutual interaction [Lux and Marchesi 1999].

Extinction events in Ecology

Ecosystems have become paradigmatic examples of complex systems, showing organization and collective dynamics across very different temporal and spatial scales. The analysis of fossil records reveals global patterns in the evolution of biodiversity that emerge from localized interactions and selection processes that occur at lower scales. The lifetime distribution of species provides clear evidence of the hierarchical structure of ecosystems. Although species lifetime is reported to be exponentially distributed, higher orders of taxa lifetimes, such as families or genera, exhibit power law decay emerging from interactions between the different species [Sneppen et al. 1995, Pigolotti et al. 2005]. Such recurrence of scale-free distributions have been measured over many orders of magnitude and exhibit similar patterns across very different living ecosystems and also in different quantitative studies of fossil records.

1.4 Outline of the Thesis

The examples mentioned above describe typical situations in which complex features appear particularly relevant. The ubiquity of complexity in Nature provides examples of a huge variety of systems to be analyzed by means of Statistical Mechanics and leads to the interconnection among various scientific disciplines. This Thesis focuses on three highlight topics of spatially extended complex systems: *Interface Growth*, *Sociophysics*, and *Complex Networks*. The document has been partitioned in three separated parts according to those topics.

The first part deals with far-from-equilibrium growing interfaces. This subject represents one of the main fields in which fractal geometry has been widely applied, and is nowadays of great interest in Condensed Matter Physics. For a review of this topic, see [Barabási and Stanley 1995, Vicsek 1989].

The Chapter 2 provides a brief and basic introduction to interface growth. We introduce some fractal and scaling concepts, as well as the main universality classes in presence of annealed disorder (EW and KPZ) in terms of both growth equations and discrete models.

In Chapter 3 we focus on the elastic interface dynamics in disordered media, *i.e.*, in presence of quenched randomness. This Chapter contains original research based on cellular automata simulations. We carry out a novel study of the dynamics by focusing on the discrete activity patterns that the interface sites describe during the relaxation toward the steady state. We analyze the spatio-temporal correlations of such patterns as the temperature is varied. We observe that, for some range of low temperatures, the out-of-equilibrium relaxation can be understood in the context of creep dynamics.

Figure 1.3: Fractal patterns are widespread in Nature. I observed these nice snow patterns during a walk in the mountains of the Campoo valley (Cantabria, Spain).

The second part of the Thesis focus on Sociophysics. This discipline attends to the social interactions among individuals -most often mapped onto networks to provide them a topological structure- and has recently attracted much interest in the physics community. Social interactions give rise to adaptive systems that exhibit complex features as self-organization and cooperation. Therefore, Statistical Mechanics provides the necessary tools to analyze the behavior of such groups of agents in a first level of simplification. A good review of the *state-of-art* in this topic is given in Ref. [Castellano et al. 2007].

The topics that Sociophysics deals with are quite a number, and we particularly focus on processes of opinion formation. The Chapter 4 presents a basic classification of the different opinion formation models present in the literature. In Chapter 5 we provide some analytical and numerical own results to describe the effect that the social temperature- understood as a simplified description of the interplay between an agent, its surroundings, and a collective climate parameter- may exert on such opinion formation processes. The thermal effect can be implemented in different ways. In the first part of the Chapter we work on a simple opinion formation model that, according to some procedural rules, reproduces the Sznajd dynamics. We include the thermal effect by means of some probability that the agents adopt the opposite opinion that the one indicated by such rules. In the second part of the Chapter we consider a system with three different interacting groups of individuals, where the thermal effect is implemented as certain probability of spontaneous changes of the agents opinion. We exploit the van Kampen's expansion approach to analyze the macroscopic behavior of the different supporter group densities as well as the fluctuations around such macroscopic behavior.

The third and last part of the document concerns Complex Networks, which have recently prompted the scientific community to investigate the mechanisms that determine their topology and dynamical properties.The rapid development of networks like the Internet and the World-Wide-Web, which represent today the basic substrate for all sort of communications at planetary level, has given rise to a number of interdisciplinary studies with highly technological applications. The analysis of Complex Networks is a relatively incipient but very active topic, and there are excellent books and reviews about this new discipline [Bornholdt and Schuster 2003, Newman 2003, Albert and Barabási 2002].

We first provide an introduction to complex networks in Chapter 6, where we introduce some basic concepts as scale-free graphs, mixing patterns, clustering coefficient, and small-world effect. In Chapter 7 we deal with traffic processes on networks, and specifically we focus on optimization of the routing protocols that define the connecting paths among all the pair of nodes. Such optimization pursues to avoid the traffic jams that emerge for huge quantities of matter or information flowing in the graph. We propose an optimization algorithm that, in order to avert jamming, minimizes the number of paths that go through the most visited node (maximal betweenness) while keeping the path length as short as possible, *i.e.*, in the proximities of the length distribution of the initial shortest-path protocol.

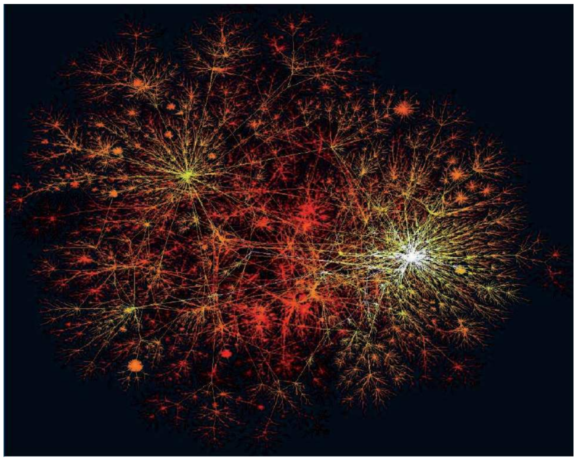

Figure 1.4: Internet network structure. Each node represents an autonomous system, *i.e.*, a group of computers under a single administrative control, and the edges are direct relations between them. This structure emerges as a self-organized distribution since new servers are continuously added to or eliminated from the network with no global supervision. From Ref. [Pietronero 2008].

Part I

Interface Growth

CHAPTER

2

Introduction and theoretical models

According to the definition, an *interface* is *the place at which different systems, bodies or phases meet and act or communicate with each other*. There are interfaces whose properties determine many important aspects of our life. For instance, the transport of sustenance that arrives to a biological cell is highly influenced by the features of its surface membrane that acts as a selective barrier of substances. And also the formation of clouds and rain due to nucleation of matter around small dust particles is dominated by surface effects.

The interest of surfaces characterization is greatly motivated by the fact that they are closely related to a wide range of phenomena. In some of them the interface is the result of either a deposition process or, in contrast, erosion or etching. A clear example is the *molecular beam epitaxy* technology employed to manufacture some semiconductor devices like computer chips. It basically consists in a slow rate deposition of single atoms onto a thin film. The atoms diffuse on the substrate and tend to stick together, giving rise to rough patterns as the ones shown in Fig 2.1. Another method commonly used in film growth is called *sputter deposition*, in which the material is bombarded with an ion beam that hits the surface and kicks out the atoms. In order to develop deposition processes of practical interest engineers usually aspire to make a smooth film, since rough surfaces have poor contact properties. Then, to avoid roughness it is first required to understand the basic mechanisms that

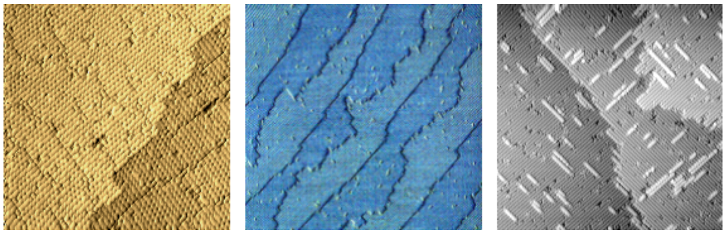

Figure 2.1: Several patterns obtained by atomic deposition onto a thin substrate. When deposited, atoms make contact with the surface, then migrate, meet, and stick. They often end up settling into particular patterns, forming dots, lengthy strands, distinctively shaped islands, vacancies, and terraces [pictures copyrighted to the Max Lagally group].

generate it and to characterize the morphology and dynamical processes that lead to these rough interfaces.

An interface may also be defined as the frontier between two different phases that propagates through an inhomogeneous material. Let us think, for instance, of the advance of a burning front in a piece of paper. Due to the heterogeneity of the medium the interface acquires certain roughness in time. Another illustrative example could be the oil extraction method based on pumping water through the rock porosities. The effectiveness of this method is influenced by the properties of the viscous water-oil interface.

There are also other processes that do not exhibit a surface at all, but with a natural choice of variables they can be described in terms of an interface. This is, for instance, the method employed to study the correlations of DNA code for protein structures. The building blocks for coding the information, called *base pairs*, can be classified in two classes called purines and pyrimidines. In order to study the purine-pyrimidine correlations in the code one can introduce a graphical representation of the sequence. A “DNA walk” is defined in terms of a variable that increases or decreases when a purine or a pyrimidine is found in the lecture of the sequence. This artificial surface, shown in Fig 2.2, allows one to visualize directly the fluctuations of the purine-pyrimidine concentration in the sequence by means of an increasing or decreasing drift of the surface height.

To characterize all these interfaces we are interested not only in their formation or their morphology, but also in how they grow and behave in time. However, their characterization is not easy since we find interfaces at very different scales, from the cellular membrane to the coastline or even the Earth surface. Furtheremore, the interface shape often depends on the scale at which it is observed. Let us think of the Earth surface: whereas we clearly appreciate its mountains and valleys when we

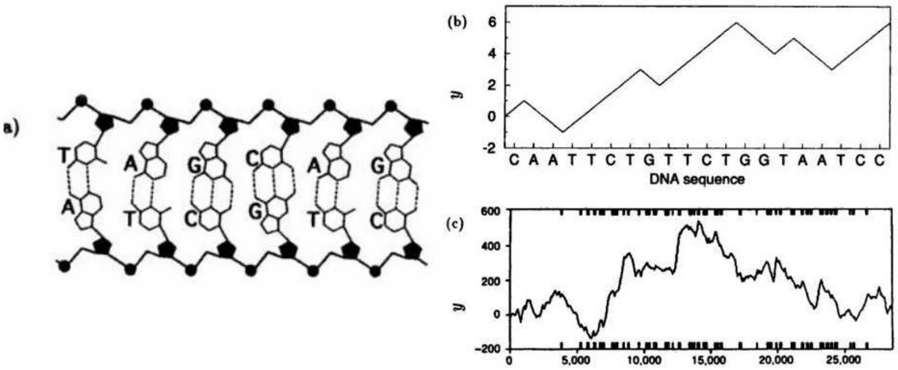

Figure 2.2: Schematic representation of DNA structure as a sequence of base pairs composed by pyrimidines (C or T) and purines (A or G). The "DNA walk" is defined by means of an auxiliary variable $y(i)$ that steps 'up' if a pyrimidine occurs at position i along the DNA chain and steps 'down' if a purine is at position i. At the bottom the "walk" for a DNA sequence of 25000 pase pairs is shown [Barabási and Stanley 1995].

move on it, an astronaut only appreciates it as a smooth ball when observed from outter space. However, there are certain surfaces that exhibit scale invariance and present analogous properties whatever scale we observe them. The coastline is just an example of this: the shape of Gulf of Mexico does not differ to much from the shape of a little creek. These are the interfaces we are interested in, and due to their scale invariance we can describe them in terms of fractality.

2.1 Fractal concepts

2.1.1 Self-similar fractality

A fractal is a geometrical structure that looks alike on all length scales. This feature makes them to be described as *scale-invariant* or *self-similar* objects. There is no a priori way of identifying a characteristic scale nor is it possible to determine at which scale a fractal is being viewed.

The term *fractal* was coined by Mandelbrot in 1975 and derives from the Latin *"fractus"*, that means "broken" or "fractured". This name refers to the striking feature of these mathematical entities that cannot be described in the traditional Euclidean geometric language. Instead, they are described by the *fractal dimension* d_f, a dimension that corresponds in a unique fashion to the geometrical shape and is often a non-integer number.

To illustrate this concept lets turn to the box-counting method traditionally employed in Euclidean geometry. Consider an object embedded in a d_e-dimensional space. To measure its volume we can cover it with $N(l)$ spheres of dimension d_e and linear size l. In ordinary metrics $N(l) \sim l^{-d_e}$ when $l \rightarrow 0$ and then the volume $V \sim N(l)l^{d_e}$ does not depend on the length l employed to carry out the measurement. However, this is not what occurs when one tries to measure the volume of a fractal object. For fractals we have, in general, $N(l) \sim l^{-d_f}$ where $d_f < d_e$. Let us turn again to the coastline example given in the introduction of the chapter. We could consider the shore as a one-dimensional object embedded into a plane. By measuring its total length we would find that it tends to grow almost indefinitely with the decreasing length of our measuring sticks. Koch Island, shown in Fig 2.3, is also a clear example of this paradoxical measurement, for which $V(l) \sim l^{2-d_f}$.

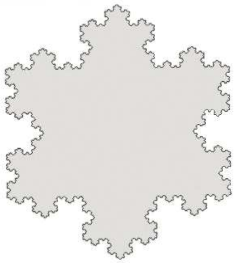

Figure 2.3: The Koch island, also known as *snowflake*, is a fractal of dimension $d_f = 1.262$ [Mandelbrot 1998].

In practice, the fractal dimension of a geometrical structure is determined by measuring $N(l)$ as a function of the linear scale

$$d_f = \lim_{l \to 0} \frac{\log(N(l))}{\log(1/l)}. \qquad (2.1)$$

A typical example of a self-similar fractal is the so-called Sierpinski gasket, whose construction is illustrated in Fig. 2.4. We can cover the whole structure at level k with $N(l) = 3^k$ triangles of linear size $l = (1/2)^k$. Then, the fractal dimension is $d_f = \log(3)/\log(2) = 1.585$, smaller than the Euclidean dimension of the embedding space $d_e = 2$.

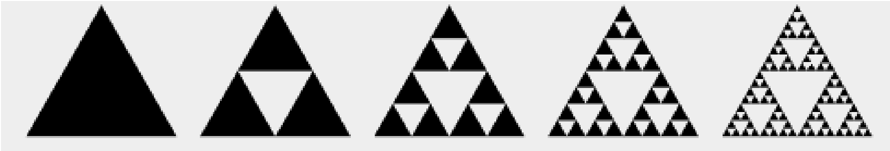

Figure 2.4: Construction of the Sierpinski gasket. Starting from a filled triangle, remove from the middle a triangle whose area is one fourth of the total. In the next step, we repeat the same procedure for the remaining three filled triangles, and this process is iterated indefinitely.

2.1.2 Self-affine random fractals

Up till now we have considered geometrical structures that present scale invariance under isotropic transformations, *i.e.*, they remain invariant when the scale is changed equally in all directions.

However, in Nature one can find situations where the dimensions of the embedding space are not equivalent. In this case the geometrical objects must be rescaled using an anisotropic transformation. If one axis is rescaled with a factor b, ($x_1 \rightarrow bx_1$), then the rest of dimensions must be rescaled as ($x_i \rightarrow b^{\alpha_i} x_i$), where the exponents α_i are called *Hurst exponents*.

Other important feature to take into account is randomness. Koch island or Sierpinski gasket are examples of fractals constructed from the simple iteration of a growth rule. However, what is commonly found in Nature- and what we are interested in this work- are objects that are not fractals by themselves but exhibit fractality from a statistical point of view.

This kind of fractals are called *random-fractals*. The simplest random self-affine fractal is generated by a one-dimensional random walk on a lattice. Consider a particle at $x = 0$. At every moment, the particle moves one site randomly up or down with equal probability $p = 1/2$. Although the trajectory $x(t)$ for a single realization does not strictly exhibit scale invariance, its statistical properties stay unaltered under scale transformations [*cf.* Fig. 2.5].

2.2 Scaling of interfaces

Interfaces are random self-affine fractals defined by the height profile $h(\mathbf{x}, t)$ over certain d-dimensional substrate $\mathbf{x}$. The surface usually grows from a flat initial configuration. For simplicity we focus on growth processes for which overhangs are

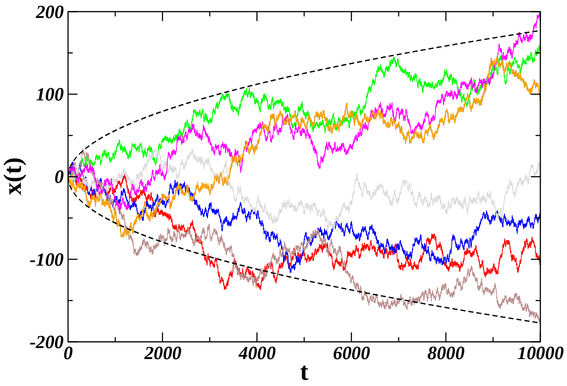

Figure 2.5: Several realizations of typical trajectories of a random walker. In the continuous approximation the probability distribution of the random variable is a simple Gaussian distribution $P(x,t) = \frac{1}{\sqrt{2\pi t}}\exp(-x^2/2t)$, whose standard deviation $\sigma(t) \sim t^{1/2}$ is marked with dashed lines.

not permitted. In these cases, $h(\mathbf{x}, t)$ is a single valuated function that exhibits self-affinity where all spatial dimensions but one are equivalent, which is the growth direction. If the substrate coordinate is rescaled as $b\mathbf{x}$ the system keeps invariant by the transformation $h(\mathbf{x}) \sim b^{-\alpha} h(b\mathbf{x})$, where the Hurst exponent α is also called *roughness exponent*. Furthermore, the whole dynamics of the system exhibits self-affinity and the time coordinate also rescales with an exponent z, called *dynamical exponent*. This means that the complete transformation under which the system remains invariant is

$$\mathbf{x} \to b\mathbf{x} \Longleftrightarrow t \to b^z t \Longleftrightarrow h \to b^\alpha h \; . \tag{2.2}$$

As previously pointed out, all surface growth processes in Nature are characterized by certain degree of randomness. Therefore it is not interesting to focus on a single interface but to analyze the statistical properties of the set of interfaces that result from different realizations of a given experiment. In other worlds, we attend to their statistical properties to describe them quantitatively. We will now shortly introduce typical measures employed to characterize surface growth.

The ***global width*** $W(L,t)$ is defined as the squared-mean root of the surface height

$$W(L,t) = \{\langle [h(\mathbf{x},t) - \langle h\rangle(t)]^2\rangle\}^{1/2} \; , \tag{2.3}$$

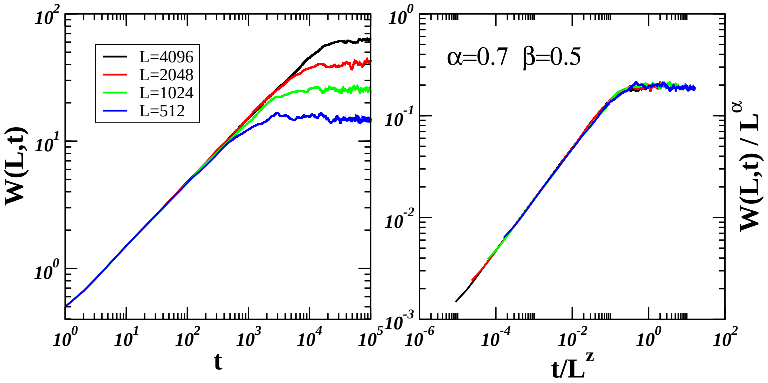

Figure 2.6: Width curves resulting from simulations of a given growth model. Different colours correspond to different system sizes $L = 4096, 2048, 1024, 512$. They collapse by plotting $W(L,t)/W_{sat}$ as a function of $(t/t_\times)$.

where $\langle ... \rangle$ denotes spatial mean over the whole system size and $\{...\}$ represents the average over a set of different height profiles. If the growth starts from a flat substrate, $h(\mathbf{x}, t = 0) = 0$, the global width is zero. Then the system evolves and the interface gradually roughens. The lack of a characteristic scale implies that the global width grows as a power law of time, $W(L,t) \sim t^{\alpha/z}$, where $\alpha/z = \beta$ is also called *growth exponent*. As the interface width grows, correlations in the height profile expand over the system and the correlation length grows as $\xi(t) \sim t^{1/z}$. When the whole system is correlated, that is $\xi \sim L$, the interface reaches a stationary state due to finite size effects. This occurs at certain time, called *saturation time*, that scales as $t_\times \sim L^z$. The interface width then reaches its saturation value $W_{sat} \sim L^\alpha$. This complex behavior of the interface width can be expressed by a unique formula:

$$W(L,t) = t^\beta f(t/t_\times) = t^\beta f(t/L^z) \; , \tag{2.4}$$

where the scaling function $f(u)$ is defined as

$$f(u) \sim \begin{cases} \text{const} & \text{if } u \ll 1, \\ u^{-\beta} & \text{otherwise.} \end{cases} \tag{2.5}$$

This compact expression allows to indistinctly deal with different systems if they are described by the same universal exponents (α, z, β). Indeed, different width curves can be collapsed by plotting $W(L,t)/L^\alpha$ as a function of t/L^z. An example is shown in Fig. 2.6, where these curves are depicted for different system sizes.

Height fluctuations can also be analyzed in a smaller region ℓ of the whole interface L, and then we obtain the ***local width***

$$w(\ell,t) = \{\langle [h(\mathbf{x},t) - \langle h\rangle_\ell(t)]^2\rangle_\ell\}^{1/2} \; . \tag{2.6}$$

Although there are many systems in which these two quantities, *i.e.* global and local surface fluctuations, scale in the same way, we will see that the behavior of global and local width will not be, in general, the same.

As we have already mentioned, spatial correlations have an important role in the interface evolution. To analyze them we define the ***spatial correlation function***

$$C(\ell,t) = \{\langle \Delta h(\mathbf{x}+\ell,t)\cdot \Delta h(\mathbf{x},t)\rangle\} \; , \tag{2.7}$$

where $\Delta h(\mathbf{x},t) = h(\mathbf{x},t) - \langle h\rangle(t)$. In the following we employ this notation for simplicity. For $\ell = 0$ this function equals the square of the global width. As ℓ increases correlations decay exponentially till they become negligible above the correlation length $\ell = \xi(t) \sim t^{1/z}$.

The analysis of correlations can also be carried out in the Reciprocal Space. We can easily define the Fourier transform of $C(\ell,t)$ as the product of the Fourier transform of $\triangle h$, and then we define the ***structure factor*** as

$$S(q,t) = \langle \widehat{h}(\mathbf{q},t)\widehat{h}(-\mathbf{q},t)\rangle \; , \tag{2.8}$$

where

$$\widehat{h}(\mathbf{q},t) = \frac{1}{L^{d/2}}\sum_x \Delta h(\mathbf{x},t)\exp[-i(\mathbf{qx})] \; . \tag{2.9}$$

Working in Fourier space has many advantages and the structure factor is usually employed to analyze the correlations. This quantity scales as

$$S(q,t) = \frac{1}{q^{2\alpha+d}}\, s(q/q^*) \quad \text{where} \quad s(u) \sim \begin{cases} u^{2\alpha+d} & \text{if } u \ll 1, \\ \text{const} & \text{otherwise.} \end{cases} \tag{2.10}$$

At correlated scales $q > q^*$, $S(q)$ decays as a power-law with exponent $-(2\alpha+d)$. This power law extends until certain value q^* that decreases with time. In fact, this is an obvious evidence of the correlation length growth, as $q^* \sim \xi^{-1} \sim t^{-1/z}$. At saturation the whole spectrum decays as $S(q) \sim q^{(-2\alpha+d)}$. This behavior is illustrated in Fig 2.7. The spectral power density of the interface is connected to the global width by the Parseval identity

$$W^2(L,t) = \int dq S(q,t) \; . \tag{2.11}$$

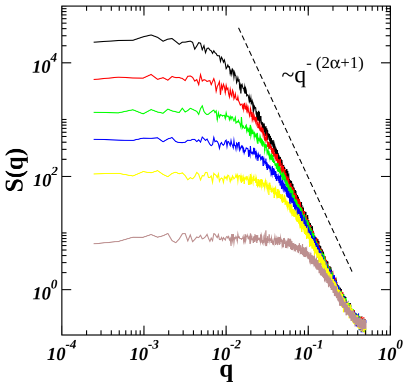

Figure 2.7: Structure factor of a given one-dimensional interface at different times. Correlated scales are observed at large values of q at which $S(q)$ decays as a power-law with exponent $-(2\alpha+1)$. This power law fashion extends until certain value $q^* \sim \xi^{-1} \sim t^{-1/z}$. At saturation the whole spectrum decays as $S(q) \sim q^{-2\alpha+1}$.

Finally, we introduce an useful tool in the analysis of surface roughness, the ***height-height correlation function*** given by

$$G(\ell, t) = \{\langle(\Delta h(\mathbf{x}+\ell, t) - \Delta h(\mathbf{x}, t))^2\rangle\} \ . \tag{2.12}$$

Since it scales in the same way as the local width $G(\ell, t) \sim w^2(\ell, t)$, the height-height correlation function is commonly employed to analyze the local fluctuations of the height profile. $G(\ell, t)$ is related with the spatial correlation function and the structure factor as

$$G(\ell, t) = 2W^2(L, t) - 2C(\ell, t) \ , \tag{2.13}$$

$$G(\ell, t) \propto \int dq[1 - cos(\mathbf{q}\boldsymbol{\ell})]S(q, t) \ . \tag{2.14}$$

The scaling presented up till now does not embrace all the cases described in the literature. In previous descriptions we have focused on the Family-Vicsek scaling [Family and Vicsek 1985], for which global and local fluctuations scale in the same way. In this case, the behavior of $W(L, t)$ and $S(q, t)$ is correctly given by Eqs.(2.4) and (2.10). However, there are many other systems whose dynamics does not satisfy the Family-Vicsek scaling. All the possible behaviors that can be found in surface growth processes are captured by the generic scaling ansatz introduced by Ramasco et al. [2000]. Here we briefly describe its main conclusions to give a general outline of interface scaling.

In Ref. [Ramasco et al. 2000] three different roughness exponents are considered: the global exponent, α; the local exponent, α_ℓ; and the exponent obtained from the analysis of the structure factor, α_s. In fact only two of them are really independent. However, as local fluctuations cannot grow faster than the local scale ℓ [Leschhorn and Tang 1993], it is not possible to observe roughness exponents $\alpha_\ell > 1$ and then the introduction of this third exponent is useful to distinguish all the possible cases.

The generic scaling ansatz is expressed in terms of the structure factor as follows

$$S(q,t) = \frac{1}{q^{2\alpha+d}}\, s(qt^{1/z})\ , \tag{2.15}$$

where now the general scaling function is

$$s(u) \sim \left\{ \begin{array}{ll} u^{2\alpha+d} & \text{if } u \ll 1, \\ u^{2(\alpha-\alpha_s)} & \text{if } u \gg 1, \end{array} \right. \tag{2.16}$$

instead of Eq. (2.10).

From Eq. (2.11) one obtains the counterpart scaling for the global width

$$W^2(L,t) \sim \left\{ \begin{array}{ll} t^{2\alpha/z} & \text{if } t \ll t_\times, \\ L^{2\alpha} & \text{if } t \gg t_\times, \end{array} \right. \tag{2.17}$$

and from the expression given in Eq. (2.13) the height-height correlation function, usually employed to analyze local fluctuations

$$G(\ell,L,t) \sim \left\{ \begin{array}{ll} t^{2\alpha/z} & \text{if } t \ll t_\times(\ell), \\ t^{2(\alpha-\alpha_\ell)/z}\ell^{\,2\alpha_\ell} & \text{if } t_\times(\ell) \ll t \ll t_\times, \\ \ell^{2\alpha_\ell}L^{2(\alpha-\alpha_\ell)} & \text{if } t \gg t_\times. \end{array} \right. \tag{2.18}$$

According to the behavior of these quantities during the growth process, different relationships are established between the three roughness exponents α, α_ℓ, and α_s. This gives rise to four different forms for the scaling behavior, schematized in Table 2.1

- **Family-Vicsek scaling**

  In this case we have $\alpha = \alpha_s = \alpha_\ell < 1$. From Eq. (2.16) is easily recovered the structure factor scaling expressed in Eq. (2.10). There is no real distinction between local and global fluctuations in this case. This means that correlations at scale ℓ saturate at time scales $t_\times(\ell) \sim \ell^z$, analogously the whole system saturates at $t_\times(L) \sim L^z$. Interfaces showing this kind of scaling behavior are then self-affine fractals and the only characteristic length scale is the system size L.

- **Intrinsic anomalous scaling**

  The global and local roughness exponents differ and we have $\alpha \neq \alpha_s = \alpha_\ell < 1$. From Eq. (2.18) this means that local fluctuations at scale ℓ do not become independent of time at $t_\times(\ell) \sim \ell^z$, *i.e.* they do not saturate, but they keep evolving till the whole system saturates at $t_\times(L)$. Furthermore, the saturation value of local fluctuations depends on the system size as $w_{sat}(\ell) \sim \ell^{\alpha_\ell} L^{(\alpha-\alpha_\ell)}$. The behavior of local fluctuations also affects to the structure factor. At early times, $t < t_\times$, $S(q,t)$ depends on a factor $t^{2(\alpha-\alpha_s)/z}$. On the other hand, at saturation the structure factor dependens on the system size $S(q, t > t_\times) \sim L^{2(\alpha-\alpha_s)} q^{-(2\alpha+d)}$.

- **Super-roughening scaling**

  In this case the system exhibits global roughness exponent $\alpha = \alpha_s > 1$ while $\alpha_\ell = 1$. As in the previous case, this implies that local fluctuations scale with the system size L and they do not saturate until correlations have spread over the whole interface. However, the reason for this case of scaling is quite different from the intrinsic anomalous one: as local fluctuations cannot grow faster than ℓ [Leschhorn and Tang 1993], local roughness exponent is bounded by $\alpha_\ell = 1$, while the global α is not limited by such restriction. Nevertheless, the structure factor $S(q)$ scales according to (2.10), in contrast to the intrinsic anomalous case.

- **Faceted surfaces scaling**

  This scaling is associated with the formation of facets or structures. Then $\alpha_s > 1$, which differs from the global exponent α. The Sneepen model [Sneppen 1992], associated with the formation of triangular structures, is a clear example. However, there are many other examples of interface growth that give rise to different facets as parabolic mounds [Ballestad et al. 2001],conical [Cates and Ball 1988] or triangular shapes [Szendro et al. 2008].

Table 2.1: Generic scaling ansatz summary

If $\alpha_s < 1 \Rightarrow \alpha_\ell = \alpha_s$	$\alpha_s = \alpha$ Family-Vicsek scaling $\alpha_s \neq \alpha$ Intrinsic anomalous
If $\alpha_s > 1 \Rightarrow \alpha_\ell = 1$	$\alpha_s = \alpha$ Super-roughening $\alpha_s \neq \alpha$ Faceted interfaces

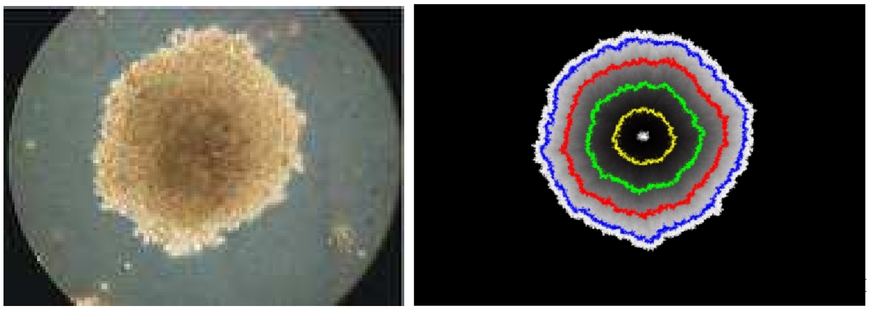

Figure 2.8: Two dimensional Eden model applied to the formation of cell colonies. *Left:* In vitro generated sample of insulin producing cells [Photo by Aldo Rozzo at European Neuroscience Institute Goettingen, Germany]. *Right:* Sample obtained by iteration of the Eden model [from the website of the Department of Computer Science at the University of Calgary]. The colours indicate the state of the structure at different times. Similarity with the real sample is clear.

2.3 Theoretical models

As we have discussed above, interfaces are relevant in many process in Nature. Examples are found in biological systems (cell colonies formation), deposition processes (molecular beam epitaxy technology), or interface motion in disordered media (fluid flow in porous media and propagation of flame fronts).

To study these phenomena physicists create models which describe through specific rules the surface growth. These are *cellular automaton models* that reproduce the main microscopical features and interactions which are responsible for the growth of the complex macroscopic shapes that result. Results obtained by means of simulations provide a relatively simple approximation to the phenomenon. One of the simplest models of surface growth was introduced by Eden [1961] to reproduce the formation of cell colonies, such as bacteria or biological tissues. This simple model starts from a single particle placed at a lattice site. A new particle is added on any randomly-chosen perimeter of the seed. When iterated, it generates a cluster with compact overall shape, *i.e*, an object whose fractal dimension is equal to the Euclidean dimension of the embedding space. However, the whole shape has a rough perimeter, and the surface of the growth zone has a nontrivial behavior [Plischke and Rácz 1984]. A sample structure obtained with this model is shown in Fig. 2.8.

Growth processes can also be described through *growth equations*, which are nothing but Langevin equations for the spatially extended height field $h(\mathbf{x}, t)$

$$\frac{\partial h(\mathbf{x}, t)}{\partial t} = G(h, \mathbf{x}, t) + \eta \,, \tag{2.19}$$

where G includes all the deterministic terms, while the noise term η incorporates the stochastic character of the growth process. The explicit form of function G depends on the symmetries of the system and the conservation laws acting during the growth. This description is particularly useful as we know that different microscopical systems sharing symmetry properties can be grouped in universality classes. So one can define a stochastic growth equation that contains all the relevant features of a given universality class. The rest of terms, which are not relevant in determining the scaling exponents, can be neglected to study the asymptotic properties of the growth process. However, they may determine the short length scale morphology, and also the short time scale behavior.

In the following we introduce the most important universality classes with non-conserved annealed disorder, that is, time-depending noise with correlations

$$\langle \eta(\mathbf{x}, t)\eta(\mathbf{x}', t')\rangle = 2D\delta^d(\mathbf{x} - \mathbf{x}')\delta(t - t') \,. \tag{2.20}$$

This kind of randomness reproduces, for instance, the effect of thermal fluctuations. In next chapter we will see that noise can also depend of the medium where the growth process takes place. In this case noise is quenched on the lattice, $\eta(\mathbf{x}, h)$, and represents the inhomogeneities or disorder of the medium.

2.3.1 Edwards-Wilkinson universality class

This universality class corresponds to the simplest linear growth process with conserved dynamics and non-conserved annealed noise. The“Random deposition with surface relaxation” model is probably the simplest example. It was proposed by Family [1986] as a simplified representation for vapor deposition on a cold substrate. Particles are deposited onto a perpendicular substrate in a randomly chosen place and then diffuse until a local minima on the surface is reached, as shown in Fig. 2.9.

The continuous version of the model was first derived by Edwards and Wilkinson [1982]. The equation of motion is

$$\frac{\partial h(\mathbf{x}, t)}{\partial t} = \nu\nabla^2 h + f + \eta(\mathbf{x}, t) \tag{2.21}$$

in the small gradient approximation $(\nabla h) \ll 1$. Diffusion is here represented by the linear term $\nabla^2 h$, which tends to smoothen the interface. The parameter ν uses to be

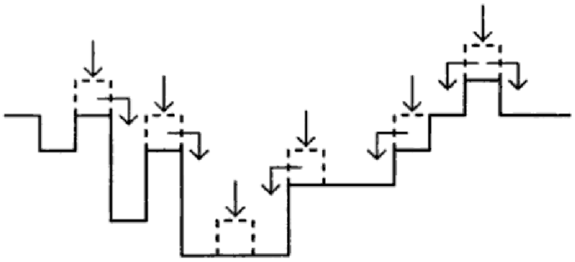

Figure 2.9: Random deposition with surface relaxation model. Each particle falls along a single column toward the surface until reaching it. Then , they relax to the neighbor site with lower height.

called *surface tension*. As it is a conserved term, the smoothing effect redistributes the irregularities of the interface maintaining the average height unchanged. Therefore, the contribution of this term to the average velocity of the interface is zero. The driving force f represents the constant influx of particles on the surface and can be transformed away by a Galilean transformation $h \to h + ft$. Since both $\langle \nabla^2 h \rangle = 0$ and $\langle \eta \rangle = 0$, the average surface velocity is given by $\langle \partial_t h \rangle = f$.

The scaling exponents of EW universality class can be obtained easily by rescaling the variables according to Eq. (2.2). Then Eq. (2.21) becomes

$$\frac{\partial h}{\partial t} = \nu b^{z-2} \nabla^2 h + b^{\frac{z-d}{2} - \alpha} \eta(x,t) + f \; . \tag{2.22}$$

Scale invariance of this equation implies

$$\alpha = \tfrac{2-d}{2} \quad \beta = \tfrac{2-d}{4} \quad z = 2 \; . \tag{2.23}$$

Such scaling exponents depend on the dimension of the interface. Indeed, from these expressions one can deduce a critical dimension $d_c = 2$ at which diffusion dominates. For dimensions $d \geq d_c$ the exponent $\alpha = 0$, this implies that the model leads to flat interfaces above d_c.

One can also obtain these results by solving Eq. (2.21) exactly in the Reciprocal Space [Nattermann and Tang 1992]. By Fourier transformation of space and time one obtains

$$h(\mathbf{q},\omega) = \frac{\eta(\mathbf{q},\omega)}{\nu q^2 - i\omega} \; , \tag{2.24}$$

where $h(\mathbf{q},\omega) = \int d\mathbf{x}dt \;\, e^{[-i(\mathbf{qx}-\omega t]} h(\mathbf{x},t)$ and $\eta(\mathbf{q},\omega) = \int d\mathbf{x}dt \;\, e^{[-i(\mathbf{qx}-\omega t]} \eta(\mathbf{x},t)$. The noise correlator in Fourier space then takes the form $\langle \eta(\mathbf{q},\omega)\eta(\mathbf{q}',\omega') \rangle = 2D(2\pi)^d \delta^d(\mathbf{q}+\mathbf{q}') \int_0^\infty d\tau \exp[i(\omega+\omega')\tau]$, with $\langle \eta(\mathbf{q},\omega) \rangle = 0$.

From this expression it is possible to obtain the amplitude of modes $\widehat{h}(\mathbf{q},t)$ by performing the inverse Fourier transformation of frequencies, and then

$$\langle h(\mathbf{q},t)h(\mathbf{q}',t)\rangle = (D/\nu q^2)(1-\exp[-2\nu q^2 t])(2\pi)^d\delta^d(\mathbf{q}+\mathbf{q}')\ . \tag{2.25}$$

Thus the interface width and the structure factor can be obtained easily as

$$W^2(L,t) = \int \frac{d^2q}{(2\pi)^d}\frac{d^2q'}{(2\pi)^d}\langle h(\mathbf{q},t)h(\mathbf{q}',t')\rangle \tag{2.26}$$

$$S(q,t) = \int \frac{d^2q}{(2\pi)^d}\langle h(\mathbf{q},t)h(-\mathbf{q},t)\rangle\ , \tag{2.27}$$

from which the exponents (2.23) are recovered.

2.3.2 KPZ universality class

Consider now a deposition model in which falling particles are able to stick onto any perpendicular surface to their trajectory. A particle sticking in this way provides a lateral growth contribution that can be represented as a non-linear term in the growth equation. This description corresponds to the so-called “Ballistic Deposition Model”.

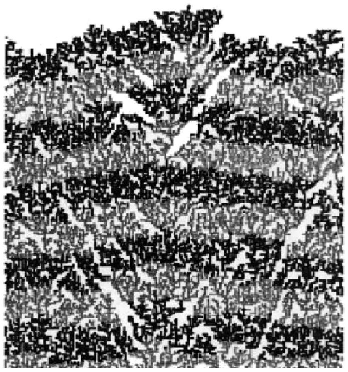

Figure 2.10: Sample of linear size $L = 200$ containing 35000 particles deposited onto a substrate by ballistic deposition. Greyscale differences are included as a guide of time measuring each 2500 depositions [Barabási and Stanley 1995].

The continuous limit of this model was first proposed by Kardar, Parisi and Zhang [Kardar et al. 1986] giving rise to a different universality class from the Edward-Wilkinson one. As growth occurs locally normal to the interface, only the projection of the local velocity onto the vertical axis will contribute to the growth equation. This implies a height increase $\delta h = [f+\eta] cos\,\theta = [f+\eta]/(1+(\nabla h)^2)^{1/2}$ [*cf.* Fig. 2.11]. In the small gradient approximation, $|\nabla h| \ll 1$, we have $(1+(\nabla h)^2)^{1/2} \approx (1 - \frac{1}{2}(\nabla h)^2 + \frac{3}{8}(\nabla h)^4] + ...)$. Considering only the first term at the lowest order in (∇h) and adding the diffusive term, we obtain the KPZ equation of motion

$$\frac{\partial h(x,t)}{\partial t} = \nu \nabla^2 h + \frac{\lambda}{2}(\nabla h)^2 + f + \eta(x,t) \ , \tag{2.28}$$

where ν, λ and f are constants, and the noise term again represents the presence of uncorrelated random fluctuations.

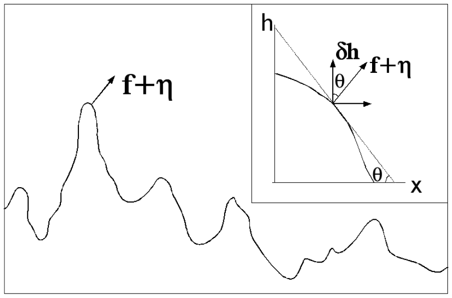

Figure 2.11: Growth occurs locally normal to the surface. This is the origin of the nonlinear term in the KPZ growth equation.

Due to the lateral growth, the up-down symmetry of the interface height is broken, unlike in the EW case. This can be clearly observed in the sample shown in Fig. 2.10. On the other hand, the presence of this non-linear term leads to non-conserved dynamics, producing an excess of velocity even in the absence of driving force. If $\lambda > 0$ non-linearities generate a height increment by adding material to the interface (or just the opposite if $\lambda < 0$). This behavior may be contrasted with the effect of the linear term, which reorganizes the interface height maintaining the total mass unchanged (conserved dynamics).

Useful information on KPZ scaling can be obtained mapping Eq. (2.28) to the Burgers equation via the transformation $\mathbf{v} = -\nabla h$,

$$\frac{\partial \mathbf{v}}{\partial t} + \lambda(\mathbf{v}\cdot\nabla)\mathbf{v} = \nu\nabla^2\mathbf{v} - \nabla\eta(\mathbf{x},t) \ . \tag{2.29}$$

This *Noisy Burgers Equation* describes the vorticity-free dynamics ($\nabla \times \mathbf{v} = 0$) of a turbulent fluid, where $\mathbf{v}(\mathbf{x},t)$ is the velocity of the fluid, ν is the viscosity and

$\nabla\eta(\mathbf{x},t)$ is a random force. The parameter λ is included here only for convenience and we particularize $\lambda = 1$. This equation is invariant under the Galilean transformation $\mathbf{v}(\mathbf{x},t) \rightarrow \mathbf{v}_0 + \mathbf{v}'(\mathbf{x} - \mathbf{v}_0 t, t)$. In terms of KPZ this means an invariance under tilt of the interface an angle ε. This result is finally expressed as a scaling relation between the exponents [Krug 1987]

$$\alpha + z = 2\,. \tag{2.30}$$

For dimension $d = 1$ another scaling relation can be obtained from the application of the fluctuation-dissipation theorem, which relates the system response to external perturbations with its spontaneous fluctuations. We can associate with Eq. (2.28) a Fokker-Planck equation describing the time evolution of the probability $\Pi(h,t)$ of having height h at time t

$$\frac{\partial \Pi}{\partial t} = -\frac{\partial}{\partial h}[G(h)\Pi] + D\frac{\partial^2 \Pi}{\partial h^2} \tag{2.31}$$

where $G(h)$ is the deterministic contribution of the KPZ equation of motion, $G(h) = \nu\nabla^2 h + \frac{\lambda}{2}(\nabla h)^2 + f$. For one dimension the stationary solution of this equation is known, and it results to be the same solution as for the linear case (EW universality class). Therefore, the value of the KPZ roughness exponent for $d = 1$ is $\alpha = 1/2$ [Barabási and Stanley 1995].

Combined with Eq. (2.30) this result leads to the exact values of the KPZ exponents for dimension $d = 1$

$$\alpha = 1/2 \quad \beta = 1/3 \quad z = 3/2\,. \tag{2.32}$$

Although the Galilean invariance is valid in any dimension, the stationary solution of Eq. (2.31) is only known in one dimension. In order to determine higher-dimensional exponents one could solve the KPZ equation in the Reciprocal Space, as was done in previous section for the linear model. However, parameters do not rescale independently in the non-linear case. Consequently, this method does not lead to an exact solution as in the Edwards-Wilkinson regime. By Fourier transformation Eq. (2.28) becomes

$$\begin{gathered}(-i\omega)h(\mathbf{q},\omega) = -\nu(i\mathbf{q})^2 h(\mathbf{q},\omega) + \eta(\mathbf{q},\omega) - \\ -\frac{\lambda}{2}\int\!\!\int h(\mathbf{k},\Omega)h(\mathbf{q}-\mathbf{k},\omega-\Omega)i\mathbf{k}i(\mathbf{q}-\mathbf{k})\frac{d\mathbf{k}d\Omega}{(2\pi)^{d+1}}\end{gathered} \tag{2.33}$$

The integrals involved in the previous equation diverge at first order in λ. Therefore, it is necessarily to solve the equation perturbatively around the exact linear solution. A bare propagator is defined as $G_0(\mathbf{q}, \omega) = (\nu q^2 - i\omega)^{-1}$. Then the general solution $h(\mathbf{q}, \omega) = G(\mathbf{q}, \omega)\eta(\mathbf{q}, \omega)$ is written in terms of the linear solution $h(\mathbf{q}, \omega) = G_0(\mathbf{q}, \omega)\eta(\mathbf{q}, \omega) + \lambda\mathcal{N}[h(\mathbf{q}, \omega)]$, where $N[h(\mathbf{q}, \omega)]$ is a nonlinear integral functional of the height. Assuming that λ is a small parameter the solution can be approached as

$$\widetilde{h}(\mathbf{q}, \omega) \approx G_0(\mathbf{q}, \omega)\eta(\mathbf{q}, \omega) + a_1\lambda\mathcal{N}_1[h(\mathbf{q}, \omega)] + a_2\lambda^2\mathcal{N}_2[h(\mathbf{q}, \omega)] + ... \tag{2.34}$$

The expression (2.34) still contains non-linear integrals over the phase space $(\mathbf{q}, \omega)$ that diverge for small momenta, so the terms of the perturbation expansion are not arbitrarily small. However, we are interested in the hydrodynamic behavior of the system, which gives the scaling behavior in the large system size and long time limits. In Fourier Space this corresponds to the $\mathbf{q} \to 0$ and $\omega \to 0$ limit. In order to avoid this problem, Renormalization Group analysis divide the Brillouin zone of momenta, $q \in [0, \Lambda]$, to handle separately small and large values, $q^< \in [0, \Lambda/b]$ and $q^> \in [\Lambda/b, \Lambda]$. Fast modes are easily integrated out from the equation, which simply corresponds to coarse-graining of the lattice spacing. On the other hand, small modes contribution is rescaled in order to recover the whole space $(\mathbf{q}, \omega)$ of the original system. As the interface is self-affine, an invariant system is obtained by means of rescaling both height and time according to $h \to b^\alpha h$ and $t \to b^z t$. The change in the parameters under the RG transformation is described by the flow equations. For KPZ the flow equations up to the lowest order λ of the RG approximation are

$$\frac{d\nu}{dl} = \nu[z - 2 + K_d g^2 \frac{2-2}{4d}] \tag{2.35a}$$

$$\frac{dD}{dl} = D[z - d - 2\alpha + K_d \frac{g^2}{4}] \tag{2.35b}$$

$$\frac{d\lambda}{dl} = \lambda[\alpha + z - 2]\ , \tag{2.35c}$$

where $g = (\lambda^2 D)/(\nu^3)$ is the *coupling constant* that establishes the relationship between parameters. The parameter l is related with the rescaling factor as $dl = d\log b$ and the constant K_d comes from the integration of the solid-angle element in the d-dimensional unit sphere. In a scale-invariant system the parameters of the rescaled equation do not change any more upon further applications of the RG transformation. Then, the exponents are obtained by searching the fixed points of the flow equations,

$$\frac{d\nu}{dl} = \frac{dD}{dl} = \frac{d\lambda}{dl} = 0\ . \tag{2.36}$$

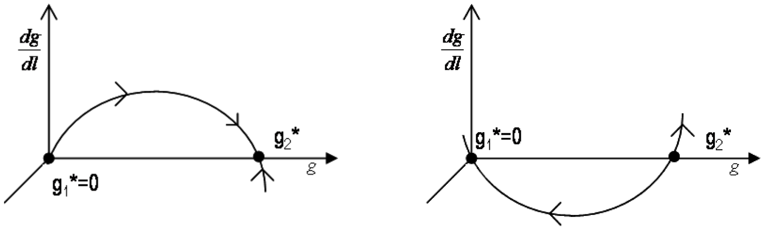

Figure 2.12: Coupling constant flow for KPZ system. *Left:* In the 1-dimensional case the attractive nonzero fixed point g_2^* determines the scaling exponents while the lineal fixed point $g_1^* = 0$ is repulsive. *Right:* For higher dimensions the nonzero fixed point g_2* is repulsive. For $g < g_2^*$ the system flows toward the linear solution $g_1^* = 0$. On the other hand, for $g > g_2^*$ the system is in the strong coupling regime and the coupling constant diverges.

From Eq. (2.35c) we recover the Galilean invariance $\alpha + z = 2$. As the λ parameter rescales independently from the rest of parameters, this scaling relation is always fulfilled whatever the dimension d is. From Eqs. (2.35a) and (2.35b) we can observe that the parameters ν and D do not rescale independently. Both equations can be compacted in a unique flow equation for the coupling constant

$$\frac{dg}{dl} = \frac{2-d}{2} g + K_d \frac{2d-3}{4d} g^3 \tag{2.37}$$

and the system behavior can then be analyzed for different values of the dimension d:

- *For $d = 1$ a nonzero attractive fixed point determines the scaling exponents.*

  The dynamics exhibits two fixed points $g_1^* = 0$ and $g_2^* = (2/K_d)^2$. The first one is repulsive and implies $\lambda = 0$, that is, the system behaves according with the linear EW regime. The second one is attractive and implies $z = 3/2$ and $\alpha = 1/2$, in agreement with the previously discussed arguments.

- *For $d \geq 2$ the coupling constant flows to infinity (strong coupling regime).*

  The dynamics is again determined by two fixed points $g_1^* = 0$ and $g_2^* \neq 0$. Now the former is attractive while the latter is repulsive. If $g < g_2^*$ the system flows, under renormalization approach, towards the attractive fixed point $g_1^* = 0$. However, for $g > g_2^*$ the coupling constant diverges and the system is in the *strong coupling regime*. Particularly, for $d = 2$ only the repulsive fixed point $g_1^* = 0$ exists and the coupling constant grows indefinitely under rescaling.

Since perturbative methods fail in the strong coupling regime, considerable efforts have been invested to attain higher-dimensional analysis of the KPZ universality

Table 2.2: Numerical results for the KPZ exponents in the strong coupling regime for $d \geq 2$. These values are obtained by means of simulations of the ballistic deposition and Eden models, as well as numerical integration of the KPZ growth equation.

Model	d	α	β	Ref
Ballistic	2	0.33	0.24	[Meakin et al. 1986]
Ballistic	2	0.3	0.22	[Baiod et al. 1988]
Ballistic	2	0.35	0.21	[Family 1990]
Eden	2	0.20		[Jullien and Botet 1985]
Eden	2	0.33	0.22	[Wolf and Kertész 1987]
Eden	2	0.39	0.22	[Devillard and Stanley 1989]
KPZ	2	0.18	0.10	[Chakrabarti and Toral 1989]
KPZ	2	0.24	0.13	[Guo et al. 1990]
KPZ	2	0.39	0.25	[Amar and Family 1990]
Eden	3	0.08		[Jullien and Botet 1985]
Eden	3	0.24	0.146	[Wolf and Kertész 1987]
Eden	3	0.22	0.11	[Devillard and Stanley 1989]
KPZ	3		0.17	[Moser et al. 1991]

class. Numerical simulations have been employed to determine the scaling exponents in dimension $d \geq 2$. Some results are shown in table 2.2. In the same way new approaches to determine analytically the exponents in $d \geq 2$ have been also introduced. For instance, Schwartz and Edwards [1992] developed a perturbative method to solve the Fokker-Planck equation associated with the KPZ dynamics. On the other hand, some authors predict a critical dimension d_c over which the strong coupling fixed point vanish and the system is dominated by the $\lambda = 0$ fixed point. However, the existence of this critical dimension remains controversial. Functional renormalization group calculations to two-loop order suggest $d_c \simeq 2.5$ [Doussal and Wiese 2003]. A set of related theories as replica symmetry breaking [Mézard and Parisi 1991] and variational studies [Garel and Orland 1997] predict $d_c = 2$, while mode-coupling equations predict $d_c = 4$ [Colaiori and Moore 2001] . On the contrary, real space calculations find no evidence at all for a finite d_c [Castellano et al. 1998]. Finally, more recent mode-coupling calculations predict two branches of solutions, one existing only for dimensionalities $d < d_c = 2$ and the other one existing up to $d_c = 4$ [Canet and Moore 2007].

CHAPTER

3

Interfaces in random media

Quenched randomness gives rise to a new type of complex phenomena. Interface growth in disordered media has attracted much attention in many branches of physics. In this chapter we particularly focus on the problem of a moving elastic interface in the presence of quenched disorder. Understanding the dynamics of elastic manifolds in disordered media has been the focus of intense activity in the last two decades, both from a theoretical and experimental point of view. The reason for such an interest is that these models are well adapted to describe, in a first approximation, non linear collective transport in many disordered systems as diverse as charge density waves [Grüner 1988], vortex lines in type-II superconductors [Blatter et al. 1994, Cohen and Jensen 1997], domain wall in magnetic materials [Lemerle et al. 1998, Repain et al. 2004, Tybell et al. 2002, Paruch et al. 2005] or crack propagation [Ponson et al. 2006]. The outline of the chapter is as follows. First we make a general introduction to quenched disorder phenomena. Later we particularize the different regimes observed in the elastic manifold dynamics. In the last section we focus on the non-equilibrium relaxation of the string when a low external driving and finite temperatures are considered.

3.1 Quenched phenomena

Models presented in previous chapter have randomness embodied by an annealed-noise term, $\eta(\mathbf{x}, t)$, that varies in time in every point of the interface. It represents, for instance, the randomness in the influx of atoms onto the interface. However, many other interface growth processes are not described by this kind of noise. A typical example may be the propagation of a driven fluid through a porous medium. In this case the resistance against the interface motion is different at each site of the medium due to its inhomogeneities. On the other hand this resistance does not depend on time. This kind of randomness is called *quenched disorder*, $\eta(\mathbf{x}, h)$, and explicity depends on the surface position inside the medium.

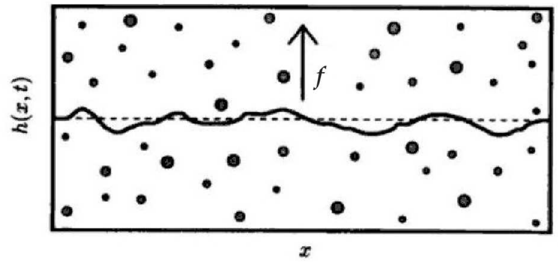

Figure 3.1: Schematic representation of a driven interface in a random environment. The pinning strength and position of the medium inhomogeneities are independent on time. Their effect is then modeled by means of quenched disorder $\eta(x, h)$.

Let us consider an elastic string driven through a disordered medium. Its dynamics results from the competition between the inhomogeneities of the background (modeled by means of a quenched disorder) and the elasticity degrees of freedom of the manifold. The former induce wandering in order to take advantage of the low energy regions in the medium, while the latter tends to smoothen the interface. The Hamiltonian of a d-dimensional elastic manifold $h(\mathbf{x}, t)$ in the limit $|\nabla h| \ll 1$ is

$$H = \int d^d\mathbf{x}[\frac{\nu}{2}(\nabla h)^2 + V(\mathbf{x}, h) - f \cdot h], \tag{3.1}$$

where ν is the surface tension parameter and f represents the external driving force. $V(\mathbf{x}, h)$ describes the random potential, which gives rise to the pinning force $\eta(\mathbf{x}, h) = -\partial V/\partial x$ acting on the interface.

From Eq. (3.1) the equation of motion can be inferred:

$$\frac{\partial h}{\partial t} = \nu\nabla^2 h + f + \eta(\mathbf{x}, h) + \varepsilon(\mathbf{x}, t). \tag{3.2}$$

The thermal noise, $\varepsilon(\mathbf{x}, t)$, is Gaussian with zero average and delta correlation, $\langle \varepsilon(\mathbf{x}, t)\varepsilon(\mathbf{x}', t')\rangle = T\delta^d(\mathbf{x} - \mathbf{x}')\delta(t - t')$, where T is the temperature. The quenched noise can be considered in different ways depending on the nature of the medium inhomogeneities. Correlations of both potential and pinning force are given by

$$\langle V(\mathbf{x}, h) \cdot V(\mathbf{x}', h')\rangle = -2\delta^d(\mathbf{x} - \mathbf{x}')R(h - h') \tag{3.3}$$

$$\langle \eta(\mathbf{x}, h) \cdot \eta(\mathbf{x}', h')\rangle = \delta^d(\mathbf{x} - \mathbf{x}')\Delta(h - h') \;, \tag{3.4}$$

where R and Δ may be short or long ranged depending on the microscopic origin of the disorder. The functional form of these correlators give rise to two different classes of quenched noise [*cf.* Fig. 3.2]

- Random Bond Disorder

  This corresponds to finite-size impurities that do not couple to the order parameter, but directly attract or repel the interface. The total energy depends only on the disorder in the immediate neighborhood of certain interface position. Then, correlations of both disorder potential and pinning force are short ranged. $R(h)$ range distance is typically given by the size of the impurities. Therefore, $R'(h)$ decreases to zero at infinity and the integral $\int \Delta(h)\; dh = 0$. Due to the local coupling with the disorder, the random potential is directly included in the Hamiltonian as in Eq. (3.1).

- Random Field Disorder

  This case corresponds to physical situations where a random disordered field couples differently to each of the two phases separated by the interface. Thus the energy resulting from the coupling involves an integral over the bulk. Random field disorder describes, for instance, a fluid invading a porous medium, where the final form of the interface is affected by all impurities in the region previously invaded by the fluid. In contrast with the random-bond case, R(u) has long-range correlations and therefore $\int \Delta(h)\; dh$ does not vanish. The Hamiltonian can be now expressed in terms of the pinning force to include the coupling between the noise and the order parameter

  $$H_{RF} = \int d^d\mathbf{x}[\frac{\nu}{2}(\nabla h)^2 + \int^h dy\; \eta(\mathbf{x}, y) - f \cdot h] \;, \tag{3.5}$$

  where $\int^h dy\; \eta(\mathbf{x}, y)$ is the random potential $V(\mathbf{x}, h)$.

The dynamics of elastic manifolds in disordered media exhibits a rich static and dynamical behavior, as we briefly discuss in the following.

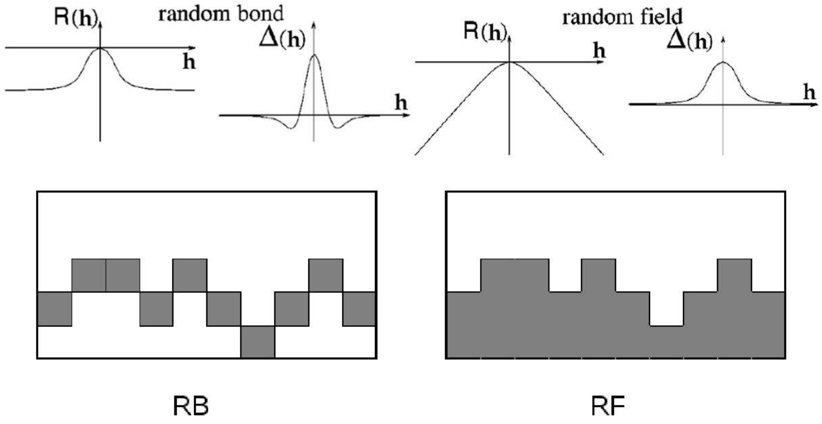

Figure 3.2: Difference between random-bond (RB) and random-field (RF) disorder. For the former one (*left*) the pinning effect depends only on the noise at the interface (grey sites). For the latter the energy of the interface is determined by the entire area swept by the manifold during its motion (grey area). On the top correlators of potential, $R(h)$, and pinning force, $\Delta(h)$, are depicted for both quenched noise classes [Chauve et al. 2000].

3.1.1 Statics

In absence of driving force ($f = 0$) the state of the system results from the competition between elasticity, pinning, and thermal fluctuations. In this case Eq. (3.2) is equivalent to the equilibrium problem at temperature T. There exists a trivial critical temperature $T = 0$ such that, for higher temperatures, the interface swings with zero global velocity around an average height $\langle h \rangle = 0$ due to thermal fluctuations. For dimension $d > 4$ the diffusion term dominates making the interface flat. For lower dimensions than this, $d < d_c = 4$, the interface follows rough optimal paths through the disordered medium. Thermal fluctuations make the system continually change its configuration and readapt itself to the disorder, adopting one of the infinitely many optimal paths in agreement with the balance between elasticity and disorder. The geometry of these optimal paths is characterized by the roughness of the manifold. At large distances the roughness $w(\ell) = \{\langle (h - \langle h \rangle)^2 \rangle_\ell\}^{1/2}$ scales as $w \sim (\ell / L_c)^{\alpha_{\rm eq}}$, where α_{eq} is the equilibrium roughness exponent and L_c is a characteristic scale called *Larkin length* [Larkin and Ovchinnikov 1979]

$$L_c \sim \left(\frac{\nu^2 {r_f}^2}{\Delta(0)} \right)^{\frac{1}{4-d}} , \tag{3.6}$$

where ν is the surface tension parameter, r_f is the size of the impurities, and $\Delta(0)$ is the height-autocorrelation of the pinning force $\eta(\mathbf{x}, h)$.

This pinning length defines the minimum average energy barrier between neighboring metastable configurations of the string. The energy barriers are expected to be randomly distributed as $P(U) \sim e^{-U/U_c}$ [Vinokur et al. 1996], where U_c is the amount of energy required to cause the minimum coherent movement of the interface at the scale L_c. However, the actual form of the distribution of energy barriers is still matter of debate [Kolton et al. 2005a]. The string can be considered as a sequence of Larkin domains independently pinned [1]. On the other hand, thermal fluctuations can give rise to larger displacements of the string. In this case the energy required to provoke the correlated movement of certain region ℓ of the interface is assumed to scale as $U(\ell) \sim \ell^{\theta_{eq}}$, with θ_{eq} some exponent that will be discussed in more detail later [*cf.* Eq. (3.11)].

Up till now, we have provided a general insight into the static regime of elastic interfaces in random media. However, the equilibrium problem at $T = 0$ is an extraordinary rich subject that concerns diverse manifolds of different dimensionalities. A unified picture of the static regime of such diverse manifolds in quenched random media was given by Halpin-Healy [1989]. He introduced a general Landau Hamiltonian for an n-component vector field $\mathbf{h}(\mathbf{x})$ with d dimensional support subject to correlated disorder $V(\mathbf{x}, \mathbf{h})$

$$H = \int d^d\mathbf{x}\{(\nu/2)(\mathbf{\Delta h} + \sigma \mathbf{V}(\mathbf{h}))\}\ , \tag{3.7}$$

where correlations of the pinning potential can be long or short ranged depending on the functional form of $R(\mathbf{h} - \mathbf{h}')$

$$\langle V(\mathbf{x}, \mathbf{h}) \cdot V(\mathbf{x}', \mathbf{h}')\rangle = \delta^d(\mathbf{x} - \mathbf{x}')R(\mathbf{h} - \mathbf{h}')\ . \tag{3.8}$$

Clearly, if $n = 1$ the system corresponds to an interface moving in a random media of $d + 1$ dimensions. On the other hand, the $d = 1$ case corresponds to a directed polymer in $n + 1$ dimensions. *Directed polymers in random media* (DPRM) are considered as a model for physical processes such as tearing or cracks, and are essentially directed walks biased along a single preferred direction that fluctuate along the n transverse dimensions due to the thermal coupling to a short-correlated quenched disorder (RB). In Fig. 3.3 we show the typical wedge geometry for the one-dimensional DPRM discrete model. For further information on DPRM see Ref. [Halpin-Healy and Zhang 1995].

---

[1] This simple picture can explain the system behavior above the critical dimension $d_c = 4$. From Eq. (3.6) it can be inferred that the Larkin length diverges for $d > 4$ and, consequently, the flat interface can be considered as a unique pinning domain of size L.

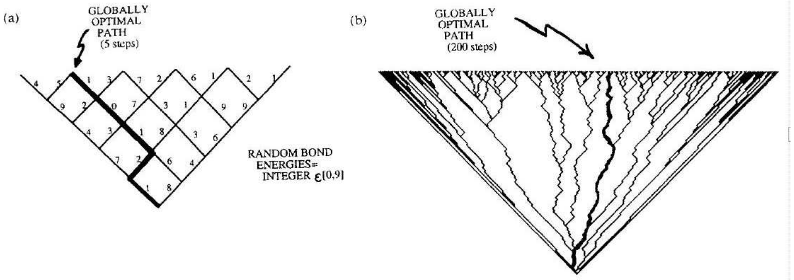

Figure 3.3: The wedge geometry for the 1+1 DPRM. Time evolves upwards and the path energy is the sum over the bond energies along the polymer length. At each time slice the path is reconfigured to have the minimum energy. On the left the globally optimal path after 5 time steps in shown. On the right the ensemble of locally optimal paths to the time slice $t = 200$ for the same realization of randomness are shown [Halpin-Healy and Zhang 1995].

For $d = 1$ the interface and directed polymer problems become equivalent. In these conditions the interface configuration is simply the path $h(x)$ described by the random polymer. Without disorder, the matter is simple. Transverse fluctuations of the polymer scale with longitudinal length as $|h| \sim x^{\alpha}$, with the trivial random-walk exponent $\alpha = 1/2$. If finite impurities are present the polymer behaves as an interface subject to a random-bond disorder. For this case, Huse and Henley [1985] provided an exact solution based on the relationship between the DPRM problem and the KPZ interface [see also Huse et al. 1985, Kardar 1985]. In their seminal paper, the authors considered the partition function of the directed polymer paths at finite temperature T,

$$Z(x,h) = \int_{\Gamma} \mathcal{D}h \exp\Big\{ -\frac{1}{T}\int_{L} dx[\frac{\nu}{2}\nabla^2 h + V(x,h)]\Big\} , \tag{3.9}$$

where Γ denotes the ensemble of all directed paths starting at $(x = 0, h(0))$ and ending at $(x = L, h(L))$.

This function satisfies the following functional differential equation with quenched multiplicative noise

$$\frac{\partial Z(x,h)}{\partial x} = \frac{1}{2}\frac{T}{\nu}\frac{\partial^2 Z(x,h)}{\partial h^2} - \frac{1}{T}V(x,h)Z(x,h) , \tag{3.10}$$

which can be mapped into KPZ via Hopf-Cole transformation $Z(x,h) \sim \exp[\widetilde{h}]$. As the free energy of the directed polymer is defined as $F = -k_b T \ln Z$, the transformation links the energy of the polymer path to the height, $\widetilde{h}$, of a KPZ interface. In the same way, the position x of the elastic manifold plays the role of time for the KPZ interface. From this equivalence it is possible to extract the exact values of the exponents that define the energy and roughness fluctuations of the 1-dimensional elastic interface

$$\begin{aligned}\Delta E &= \langle (E - \langle E \rangle)^2 \rangle^{1/2} \sim x^{\theta_{eq}} \\ \Delta h &= \langle (h - \langle h \rangle)^2 \rangle^{1/2} \sim x^{\alpha_{eq}} \ ,\end{aligned} \tag{3.11}$$

with

$$\alpha_{eq} = \frac{1}{z_{KPZ}} = 2/3 \quad \theta_{eq} = \beta_{KPZ} = 1/3 \ , \tag{3.12}$$

and both exponents satisfy the scaling relation $2\alpha_{eq} - \theta_{eq} = 1$. The DPRM and the random-bond elastic interface are not equivalent in $d > 1$. To obtain the exponents in higher dimensions one has to resort to a FRG expansion in $\epsilon = 4 - d$, which approaches $\alpha_{eq} \approx 0.208(4 - d)$. In such dimensionalities the generalized scaling relation $2\alpha_{eq} - \theta_{eq} = 2 - d$ is still valid. For $d = 2$ numerical tests were done by Kardar and Zhang [1989], who found $\alpha_{eq} = 0.50 \pm 0.08$ using the transfer matrix method.

On the other hand, FRG calculations also provide useful approximations for the random-field disorder problem. In this case the roughness exponent has been estimated to be $\alpha_{eq} \sim (4 - d)/3$ [Fisher 1986]. This approach has been validated by numerical simulations, which found $\alpha_{eq}(d = 1) = 1$ in excellent agreement with FRG results [Kardar and Zhang 1987]. Similarly, the transfer matrix method extended to two dimensions gave $\alpha_{eq} = 0.59 \pm 0.07$, which is compatible with the prediction $\alpha_{eq}(d = 2) \sim 2/3$ [Kardar and Zhang 1989].

3.1.2 Depinning at $T = 0$

At zero temperature Eq. (3.2) becomes the simplest representation of the quenched Edwards-Wilkinson universality class (QEW), first introduced by Bruinsma and Aeppli [1984]

$$\frac{\partial h}{\partial t} = \nu \nabla^2 h + f + \eta(\mathbf{x}, h) \ . \tag{3.13}$$

Due to the competition between elasticity and quenched disorder the system undergoes a critical transition at a threshold driving force, $f = f_c$, from a moving to a pinned phase. For an external driving $f < f_c$ (*pinned phase*) the interface moves until it finds the closest configuration where the energy has a local minimum, whereupon it becomes pinned. For $f \gg f_c$, however, random pinning forces are overcome by the external driving and the average position of the front moves at finite velocity $v \sim f$. In these conditions the quenched noise is washed out and the noise term reduces to an annealed one, $\eta(\mathbf{x}, h) \approx \eta(\mathbf{x}, vt)$. Then, Edwards-Wilkinson universality class of Eq. (2.21) is recovered (*flow phase*). In the critical region $f \lesssim f_c$ the interface consists of pinned and unpinned sections. Once the combined effect of the driving and elastic forces overcome the pinning forces in a particular area, the interface 'jumps' ahead, but is eventually trapped again by an another region of strong pinning sites. Thus the interface exhibits a slow, smooth motion interspersed with avalanches, which present a critical size distribution $p(s) \sim s^{-\tau}$. In connection with the previously discussed static regime, pinned regions of the interface can be considered as a sequence of pinned Larking domains. Then, the critical force f_c may be estimated as the minimal applied force able to depin one of these Larkin domains L_c at $T = 0$.

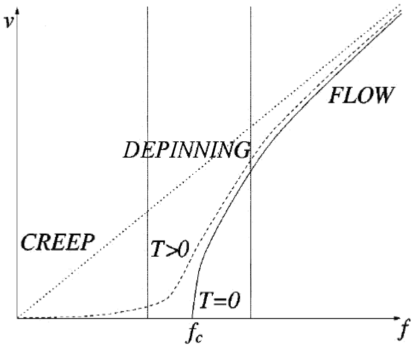

Figure 3.4: Typical force-velocity characteristics [Chauve et al. 2000], exhibiting pinning at $T = 0$ with a threshold force f_c. At large drive, the system flows as if there were no quenched disorder. When finite temperatures are considered creep dynamics is observed at $T > 0$ and $f < f_c(T = 0)$ [*cf.* Sec. 3.1.3].

This critical transition is well characterized as $f \to f_c^+$ by a diverging correlation length $\xi \sim (f - f_c)^{-\nu_{\text{dep}}}$, which corresponds to the average size of the pinned regions. Also the asymptotic velocity has the form $v \sim (f - f_c)^{\theta_{\text{dep}}}$. The critical exponents are $\nu_{\text{dep}} = 1/(2 - \alpha_{\text{dep}})$ and $\theta_{\text{dep}} = (z_{\text{dep}} - \alpha_{\text{dep}})\nu_{\text{dep}}$ where α_{dep} and z_{dep} are the roughness and dynamical exponents of a pinned interface at $f = f_c$. FRG calculations give estimates for the values of these exponents in the form of series expansions in the variable $\epsilon = 4 - d$ [Narayan and Fisher 1993, Nattermann et al. 1992]:

$$\alpha_{dep} \approx \frac{\epsilon}{3} \quad z_{dep} \approx 2 - \tfrac{2\epsilon}{9} \quad \nu_{dep} \approx \frac{3}{6 - \epsilon}\,. \tag{3.14}$$

In principle, one could expect different values of the depinning exponents depending on the nature of the quenched disorder, as occurs in the statics regime. However, Chauve et al. [2000] showed by means of FRG calculations that the RB quenched noise correlator evolves during the flow towards a RF disorder. This leaves only one universality class for the elastic manifold at depinning, in contrast with the two classes RB and RF that appear in the static regime.

Such an expansion in $\epsilon = 4 - d$ provides trustworthy results only for sufficiently small values of the expansion parameter, *i.e.*, in the vicinity of the critical dimension $d_c = 4$. To study the system in lower dimensionalities one must resort to numerical simulations [Dong et al. 1993, Jensen 1985]. Probably, the most accurate estimation of the exponents comes from a cellular automaton proposed by Leschhorn [1993; 1996], which is based on a simplification of the continuous equation (3.13). The model is defined on a square lattice where each cell is assigned a random force $\eta_{i,h}$, which takes the value 1 with probability p and $\eta_{i,h} = -1$ with probability $1-p$. The surface height is an integer $h_i(t)$ starting from a flat initial condition. At each time step the function $v_i(t) = \kappa\,(h_{i+1} + h_{i-1} - 2h_i) + g\eta_i(h_i)$ is evaluated for all sites $i = 1, ..., L$. The surface advances at site i, $h_i(t+1) = h_i(t) + 1$, whenever the condition $v_i(t) > 0$ is hold. The parameter g measures the strength of the disorder, while the driving force is determined by the difference $p - (1-p) = 2p - 1$. The exponents measured by Leschhorn at the critical point were $\alpha \approx 1.25$, $\beta \approx 0.88$, $\theta \approx 0.25$ and $\nu \approx 1.33$ for dimension $d = 1$. He also measured the exponents for $d = 2$, such were $\alpha \approx 0.74$, $\beta \approx 0.47$, $\theta \approx 0.65$ and $\nu \approx 0.8$.

If nonlinear corrections are included in the growth equation one arrives at the quenched-KPZ (QKPZ) equation [Galluccio and Zhang 1995]

$$\frac{\partial h}{\partial t} = \nu \nabla^2 h + \frac{\lambda}{2}(\nabla h)^2 + f + \eta(x,h)\;, \tag{3.15}$$

which gives rise to a different universality class. Such nonlinearity may be kinetically generated and thus λ is proportional to the global velocity of the interface, $\lambda \propto v$. However, it has been shown to be irrelevant at the depinning threshold, as v goes to zero and the QEW universality class is recovered [Narayan and Fisher 1993]. On the other hand, the nonlinear effect may be originated by the anisotropy of the quenched disorder, which yields a nonvanishing λ at the depinning transition [Tang et al. 1995]. If the medium randomness has different correlations in the directions perpendicular and parallel to the growth direction, there exists an overall slope $\langle(\nabla h)\rangle$ that constributes to the interface velocity $\langle \delta_t h\rangle \sim \lambda \langle(\nabla h)\rangle^2$ even at

$f \to f_c$ [2]. Such contribution modifies the critical behavior of the system with regard to the QEW universality class.

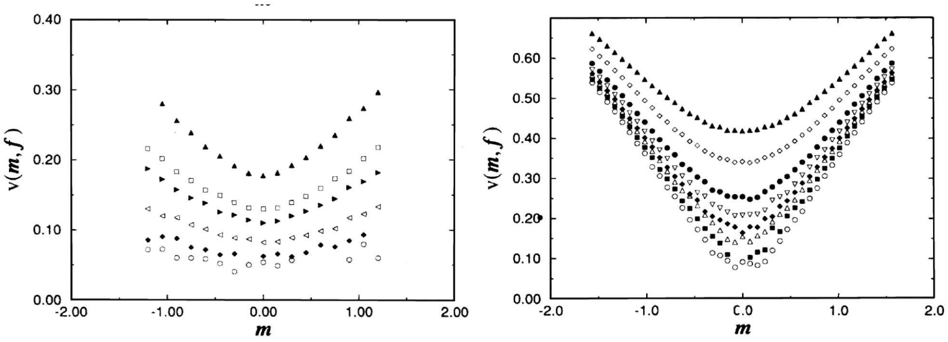

Figure 3.5: Dependence on the tilt $m = \langle(\nabla h)\rangle$ of the average velocity, in one-dimensional models belonging to QEW (left) and QKPZ (right) universality classes. Data from different forces are indicated by different symbols, approaching to f_c from top to bottom [Amaral et al. 1994].

The different scaling properties of this new universality class have also been demonstrated by means of simulations of simple automaton models (see Fig. 3.5 from [Amaral et al. 1994]). Tang and Leschhorn [1992] and Buldyrev et al. [1992] proposed simple models based on directed percolation to show depinning mechanisms according to Eq. (3.15). These algorithms are known as directed percolation depinning (DPD) models. They basically consist on a lattice with certain fraction p of blocked cells that put up resistance to the interface advance. At certain critical density p_c, the blocked sites are enough to form a continuous directed path that spans across the whole system. Under these circumstances the interface is stopped by the pinning path. In $d = 1$ the path of blocked sites can be mapped onto a directed percolation path that leads to infer the scaling exponents $\alpha = 0.63$, $z = 1$, and $\theta = 0.636$. Higher dimensional generalization of directed percolation considers directed paths embedded in higher dimensional spaces. Such analysis is of general interest, in particular because many experimentally relevant interfaces are two-dimensional. The problem can still be mapped onto a percolation problem, but the pinning cluster must be considered as a directed surface instead of a directed path. For $d = 2$ Amaral et al. [1995] observed the exponents $\alpha = 0.48$, $z = 1.15$, and $\theta = 0.8$.

---

[2] This hallmark dependence of the global velocity with the average slope $m = \langle(\nabla h)\rangle$ was expressed by Tang et al. [1995] as $v(0) \approx v(0) + \frac{\lambda}{2}m^2$, with λ diverging at the critical point. Further analysis of such dependence suggests that the velocity goes as $v(m) \approx [v(0) + \lambda m^2]/\sqrt{1+m^2}$ and not as a single parabola [Neshkov 2000]. This result washes away the divergence of the nonlinear parameter at the critical point.

3.1.3 Creep

In between the two limits ($f \neq 0, T = 0$) and ($f = 0, T \neq 0$) there is a region of very rich dynamics when low temperatures and well below zero-temperature depinning threshold forces are considered, called *creep regime*. In this scenario motion occurs at any drive since thermal fluctuations help the interface advance even at low driving forces $f < f_c(T = 0)$. As shown in Fig 3.4 the velocity does not vanish for small values of f, in contrast to the $T = 0$ depinning case. The dynamics of the manifold can be understood as quasi-pinned configurations that move to more favorable metastable states due to the effect of thermal fluctuations. The relaxation toward the steady state is extremally slow and the system exhibits properties of glassy systems as aging, memory effects, and violation of the fluctuation-dissipation theorem [Young 1998, Duemmer and Le Doussal 2007, Ramasco et al. 2006]. Based on the sluggish motion of the interface, a qualitative understanding of the problem has been made considering thermal activations over the energy barriers of the equilibrium problem, for which the velocity is strictly zero [*cf.* Sec. 3.1.1]. A quite successful scaling theory can be constructed assuming this quasi-equilibrium hypothesis.This approach predicts a creep velocity for the steady-state that links the statics with the nonlinear transport of the disordered elastic system [Ioffe and Vinokur 1987, Nattermann 1990, Scheidl and Vinokur 1996]

$$v_\infty(f, T) \sim \exp\left[-\frac{U_c}{T} \cdot \left(\frac{f_c}{f}\right)^{-\mu} \right], \tag{3.16}$$

where the exponent μ is given by the equilibrium exponents:

$$\mu = (d - 2 + 2\alpha_{eq})/(2 - \alpha_{eq}). \tag{3.17}$$

This approach also suggests that there is a typical length scale $L_{opt} \sim (f/f_c)^{-\nu_{eq}}$ that separates scales controlled by thermal activated motion ($\ell \ll L_{opt}$) from large scales ($\ell \gg L_{opt}$) that slide freely with $\nu_{eq} = 1/(2 - \alpha_{eq})$.

The creep law (3.16) has been observed to be in good agreement with various experiments [Blatter et al. 1994] and the scaling relation (3.17) has also been confirmed experimentally for magnetic domain walls [Lemerle et al. 1998] and vortices [Fuchs et al. 1998]. On the theoretical side, functional renormalization group calculations based on a $\epsilon = 4 - d$ expansion have confirmed and expanded the conclusions of the scaling theory [Le Doussal et al. 2006]. Also, the recent introduction of fast-convergent algorithms to reach the steady-state [Rosso and Krauth 2002] has allowed to test the validity of the creep velocity with great accuracy [Kolton et al. 2005a].

The quasi-equilibrium hypothesis also provides an interesting approach to understand the relaxation mechanism toward the steady state. This relaxation is governed by a growing characteristic length, $L(t)$, separating the equilibrated short length scales from the long distance ones that keep a memory of the initial condition [Kolton et al. 2005b]. It can be inferred that $L(t)$ evolves logarithmically with time [Fisher and Huse 1988]

$$L(t) \approx L_c \Big[\frac{T}{U_c} log\Big(\frac{t}{t_0}\Big)\Big]^{1/\theta_{eq}} , \tag{3.18}$$

where L_c is the Larkin length , $U_c(L_c)$ is the associated energy scale that characterizes the equilibrium barrier distribution, and t_0 is a microscopic time scale. Below this growing length $L(t)$ one expects that the dynamics is governed by thermally activated jumps over the equilibrium energy barriers $U(\ell) \sim \ell^{\theta_{eq}}$, which have to be overcome to equilibrate the system up to the scale ℓ. Thermal fluctuations make the system move from certain quasi-pinned configuration to a more favorable one, and the system visits different metastable states in its evolution to the steady state.

As corresponds to a thermally activated process, the average waiting time for a barrier $U(\ell)$ to be overcome is given by an Arrhenius law, $\langle\tau(\ell)\rangle \sim \tau_0 \exp\left[U(\ell)/T\right]$, where τ_0 is a microscopic time scale. These events are supposed to be uncorrelated and follow a Poissonian distribution in time. Then, the corresponding probability density of waiting times over a given barrier $U(\ell)$ is

$$\mathcal{P}_U(\tau) \sim \langle\tau(\ell)\rangle^{-1} \cdot \exp[-\tau/\langle\tau(\ell)\rangle] . \tag{3.19}$$

Considering the whole distribution of barriers $P(U)$ that conform the equilibrium energy landscape of our system we have a distribution of waiting times $\Psi(\tau)$ given by $\Psi(\tau) \sim \int P(U)\mathcal{P}_U(\tau)dU$. From Sec. 3.1.1 such equilibrium barriers are expected to be distributed as $P(U) \sim \exp\left(-aU/U_c\right)$ [Vinokur et al. 1996], where U_c is the minimum average energy barrier between neighboring metastable configurations at the Larkin microscopic pinning length scale L_c, and a is some dimensionless constant. With this choice for $P(U)$ one then arrives at the distribution of waiting times between two consecutive metastable states

$$\Psi(\tau) \sim T\Big(\frac{\tau_0}{\tau}\Big)^{1+aT/U_c} . \tag{3.20}$$

This power-law distribution is bounded from above by the maximum time $\tau_{max} \sim \tau_0 \exp[U(L_{opt})/T]$ corresponding to the typical scale L_{opt}. As previously mentioned, this characteristic length scale separates scales controlled by thermal activated motion ($\ell \ll L_{opt}$) from large scales ($\ell \gg L_{opt}$) that slide freely. In other words, L_{opt} gives us the upper bound above which thermally activated processes are no longer relevant. This characteristic scale has been demonstrated via FRG calculations [Chauve et al. 2000]. It corresponds to the optimal excitation that minimizes the free energy cost to equilibrate the system, $U(L_{opt}) \sim \min[U_c(\ell/L_c)^{\theta_{eq}}]$.

As exposed up till now, the quasi-equilibration hypothesis leads to a quite successful scaling theory of the creep regime. However, these arguments are based on strong assumptions. This physical picture of creep motion is still very phenomenological, and many important questions remain open.The fact that dynamical barriers can be determined purely from the statics is not clear. Moreover, the assumption that the energy landscape is characterized by a unique scale U_c that describes differences between energy barriers does not directly imply that this unique scale may also characterize the energy differences between neighboring metastable states. The fact that static barriers and valleys scale with the same exponent is already a non trivial hypothesis. The second and more delicate assumption is the validity of the Arrhenius description of the thermally activated jumps between metastable states. Recent studies prove clear deviations from this quasi-equilibrium picture. For instance, strong violation of the creep formula is observed at low enough temperatures in [Kolton et al. 2005a]. Although the creep velocity law is still valid, Kolton et al. observed that the exponents μ and α clearly deviate from their equilibrium values as $T \rightarrow 0$ .The surprising conclusion is that only for moderately low temperatures the expected values of the exponents $\alpha = \alpha_{eq}$ and $\mu = (d-2+2\alpha_{eq})/(2-\alpha_{eq})$ are found. On the other hand, deviations from the Eq. (3.18) for the equilibrium length $L(t)$ have also been observed [Kolton et al. 2005b]. An alternative form $L(t) \sim t^{1/z}$ is obtained at short time scales of the relaxation process toward the stationary creep regime. This would suggest a thermally activated motion over barriers scaling logarithmically with the system size, instead of $U(\ell) \sim \ell^{\theta_{eq}}$.

3.2 Forced Relaxation at finite temperatures

In this section we present original research work for this Thesis. As shown before, considerable progress has been made in last few years in our understanding of the steady-state of the driven elastic string. However, the nonequilibrium relaxation dynamics toward the stationary state has received comparatively much less attention. Particularly, many questions remain still open for the elastic string relaxation at finite temperatures. Understanding such nonstationary physics is clearly crucial since it gives complementary information on the energy landscape of barriers that determine the manifold dynamics and, for experiments, is needed to describe the many systems that are quenched in the glassy state and then have to relax (*e.g.*, by changing rapidly the temperature). Theoretical attempts to describe the dynamics during relaxation has been made using mean-filed and renormalization group approaches [Ioffe and Vinokur 1987, Nattermann 1987, Vinokur et al. 1996, Cugliandolo et al. 1996, Chauve et al. 2000, Balents and Le Doussal 2004, Schehr and Le Doussal 2004; 2005]. However, direct application of these results (valid close to the critical dimension) to one dimensional domain walls is difficult. Numerical studies in low dimensions provide hints on this difficult problem, although they are also difficult since they have to deal with ultra long time scales. Recently, Schehr and Le Doussal [2004; 2005] investigated the relaxation regime for an interface initially flat by analyzing two-time correlation functions, as $f \to f_c$, showing by functional renormalization group methods that the transient dynamics displays universal behavior. This strongly suggests that some degree of universality is also present in the intermediate nonsteady regime.

In this section we consider the non-equilibrium relaxation of the one-dimensional *forced* elastic string in a random-field disorder for driving forces well below the $T = 0$ depinning force. As we discussed previously, these conditions give rise to a slow creep regime where the interface dynamics can be described by thermally activated jumps of spatially correlated regions over the energy barriers separating different metastable states. A novel type of study is carried out by focusing on the local activity statistics as the temperature is varied. At variance with most existing studies of the creep regime of the elastic line, the model we consider does not allow for backward movements of the interface. This up/down asymmetry is relevant in some type of experimental systems like for instance in forced fluid imbibition, paper wetting, advancing cracks in solids, and flux lines in superconductors when an electric field is applied. This asymmetry could also illustrate the dynamics of an elastic string on ratchet-like potentials, which facilitate movement in a preferred direction.

Our numerical model for the elastic string is discrete, which allows us to characterize properly the activity. The lack of up/down symmetry is responsible for new phenomenology at very low temperatures, which is different from the equilibrium-like behavior typically observed in previous studies of the zero-temperature limit of the driven string.

A key quantity we look at is the return probability, $\mathcal{P}_{\mathrm{r}}(\tau)$, for the activity to be back at a particular site after a time τ. We show that this probability is directly connected with the interface velocity, the power spectrum $S(\omega) \sim 1/\omega^{\alpha}$ of velocity fluctuations, and the structure of avalanches of activity. Our analysis provides global dynamical information from a local observable, which may be useful in experiments. By means of scaling arguments we show that local activity statistics in the region of moderate temperatures can be interpreted as thermally activated jumps of spatially correlated regions over the energy barriers separating different metastable states. However, as temperature is decreased this picture breaks down, since our model is a genuinely out-of-equilibrium system in the limit $T \to 0$.

3.2.1 Description of the model

Our model is inspired in Leschhorn cellular automaton [Leschhorn 1993; 1996] for the string at zero temperature, which was introduced in Sec. 3.1.2. Here we study the one-dimensional case; generalization to higher dimensions is straightforward. We consider semi-infinite square lattice $L \times \infty$, and the string position h_i at each point i takes integer values. A random pinning force $\eta_i(h_i)$ is assigned to each lattice site. As corresponds to random-field disorder η is an uncorrelated Gaussian variable with zero mean and unit variance. The surface height is a single-valued integer function $h_i(t)$ and the model is evolved at a fixed temperature T as follows. Starting from a flat initial state, the function

$$\begin{aligned} v_i(t) &= \kappa\,(h_{i+1} + h_{i-1} - 2h_i) + \Delta^{1/2}\,\eta_i(h_i) + \\ &\quad + T^{1/2}\,\varepsilon_i(t) + f \end{aligned} \tag{3.21}$$

is evaluated at time $t > 0$ for all sites $i = 1, \cdots, L$. Site i moves forward, $h_i(t{+}1) \rightarrow h_i(t) + 1$, if and only if $v_i(t) > 0$, otherwise it remains pinned. Periodic boundary conditions in the substrate direction, $h_{L+1} = h_1$ and $h_0 = h_L$, are used. After evaluation of Eq. (3.21) for all i the update is carried out in parallel for the whole front. Note that backward movements are not permitted.

Following Ref. [Leschhorn 1996], both stiffness κ and noise strength parameters are chosen to have the same order of magnitude, so the interface can become rough on length scales of the order of the lattice spacing. We fix $\kappa = 10$ and $\Delta^{1/2} = 20$. To analyze the slowly driven regime we employ a very small applied force $f \approx 5 \times 10^{-3} \times f_c(T = 0)$, although other values have been also tested. The equation of motion can be rescaled and the dynamics of the system can be described in terms of the dimensionless temperature $\widetilde{T} = T(\kappa/\Delta^2)^{1/3}$.

3.2.2 Dynamical regimes

First we focus on how the average velocity of the interface, $v(t) = \langle \Delta h/\Delta t \rangle$, behaves with time. In Fig. 3.6, we have represented $v(t)$ for different values of temperature that can be identified with different dynamical regimes: high, low and ultra-low temperatures. For high values of T, the system rapidly relaxes toward an steady-state with constant velocity [see Fig. 3.6(a)]. When temperature decreases, as mentioned before, the relaxation time becomes longer and longer, eventually diverging in our limited time window simulations. In the range of times displayed in Fig. 3.6(b) the relaxation of the velocity decays toward a stationary velocity $v_\infty(f, T)$ as a power-law $v(t) - v_\infty \sim t^{\gamma(T)}$ for low temperatures $0.15 \lesssim \widetilde{T} \lesssim 0.40$. We find the exponent to be $\gamma = 0.82(4)$, $0.76(4)$, and $0.72(3)$ for temperatures $\widetilde{T} = 0.20, 0.24$, and 0.28, respectively. Surprisingly, when temperature is lowered even further, $\widetilde{T} \ll 0.15$, the velocity exhibits a series of plateaus separated by well defined and sudden drop-offs at which the interface motion is rapidly slowed down [Fig. 3.6(c)]. We suggest that this distinct ultra-low regime arises due the lack of up/down symmetry of our *forced* elastic string, and it is absent in the continuous model of the driven string (QEW) [Kolton et al. 2005a].

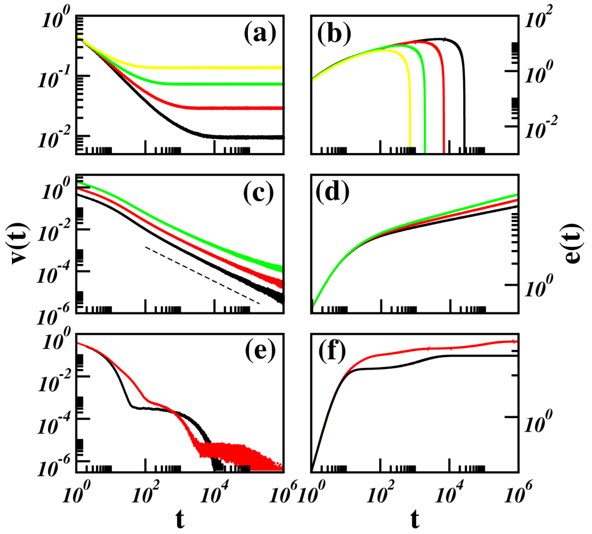

Figure 3.6: Interface velocity (left) and energy per site (right panels) averaged over 500 runs for a system of size $L = 16384$. Different dynamical regimes are shown. High temperature regime *(a-b)* for $\widetilde{T} = 2$ (yellow), 1.2 (green), 0.8 (red), and 0.6 (black). Low temperature regime *(c-d)* for $\widetilde{T} = 0.28$ (green), 0.24 (red), and 0.20 (black). Curves are vertically shifted for clarity. The dashed line has a reference slope -0.85. Ultra-low temperature regime *(e-f)* for $\widetilde{T} = 2 \times 10^{-2}$ (red) and 4×10^{-3} (black). The relative error of the velocity data is $\overline{v}/\sigma \sim 10^{-2}$ at any temperature.

As this model has a well defined Hamiltonian, we can also study how the average energy of the system evolves in time. According to Eq. (3.5) the energy per site can be estimated as

$$e(t) = \frac{1}{L} \sum_i \left\{ \frac{\kappa}{2} \left[\frac{h_{i+1} - h_{i-1}}{2} \right]^2 - f \cdot h_i + \Delta^{1/2} \sum_{j=0}^{h_i} \eta_i(j) \right\}, \tag{3.22}$$

where L is the lateral size of the substrate. The resulting $e(t)$ is shown in the right panels of Fig. 3.6.

During the relaxation time the system explores configurations accordant with the strength of the disorder, therefore the energy per site increases during this transitory evolution toward the steady state. In the high temperature regime, it can be observed how this initial increase finishes when the system is in the vicinity of the equilibrium point and then the energy decreases, according to the Langevin equation. In this particular case the energy, referred to the initial flat surface at zero height, keeps decreasing *ad infinitum* due to the presence of the driving force term,$-f \cdot h$, in the Hamiltonian.

In the low and ultra-low dynamical regimes the relaxation of the system continues during the time span considered, so $e(t)$ increases continuosly. It is interesting to underline that the behavior of $e(t)$ is always consistent with the functional form of $v(t)$.

In order to better characterize these dynamical regimes we can also attend to other features as the roughness and spatial correlations of the interface.

The structure factor is defined in one dimension as $S(q,t) = \langle \widehat{h}(q,t)\widehat{h}(-q,t)\rangle$, where $\widehat{h}(q,t) = L^{-1/2}\sum_{n=1}^{L} h_n(t)\exp(2\pi iqn)$ is the Fourier transform of the string profile. As $S(q,t)$ is the Fourier transform of the autocorrelation function of the interface height, it scales as $q^{-(2\alpha+1)}$ with the roughness exponent α. In Fig. 3.7 we show $S(q,t)$ for typical temperatures $\widetilde{T} = 0.02, 0.24$ and 1.2, corresponding to the three different dynamical regimes.

At high temperatures we are able to obtain the stationary structure factor $S(q)$ due to the fast convergence to the system toward the steady-state. In this regime we observe a roughness exponent $\alpha_{\rm th} \approx 0.5$ that falls into the so called Edwards-Wilkinson universality class [*cf.* Sec. 2.3.1]. This result is in agreement with the expected behavior of the system at high temperatures, as thermal fluctuations wash out the effect of quenched randomness and the front moves freely trough the disordered medium.

When temperature is decreased the picture is totally different. In the low temperature regime, $0.15 \lesssim \widetilde{T} \lesssim 0.40$, random forces are able to locally pin the interface and the relaxation time increases considerably, giving rise to a non stationary $S(q,t)$ in the considered time span. However thermal fluctuations are able to equilibrate the line at short scales. We observe a characteristic wavenumber $q^*(t)$ over which the interface exhibits the equilibrium random-field roughness exponent, $\alpha_{eq} = 1$. This result is consistent with the picture of creep dynamics as a thermally activated motion at scales below the equilibration length $L(t) \approx [q^*(t)]^{-1}$ [Vinokur et al. 1996, Chauve et al. 2000] . These two regimes and roughness exponents, *i.e.*, roughness α_{th} and α_{eq} for high and low temperatures respectively, are also observed in numerical simulations of the one-dimensional continuous model QEW [Kolton et al.

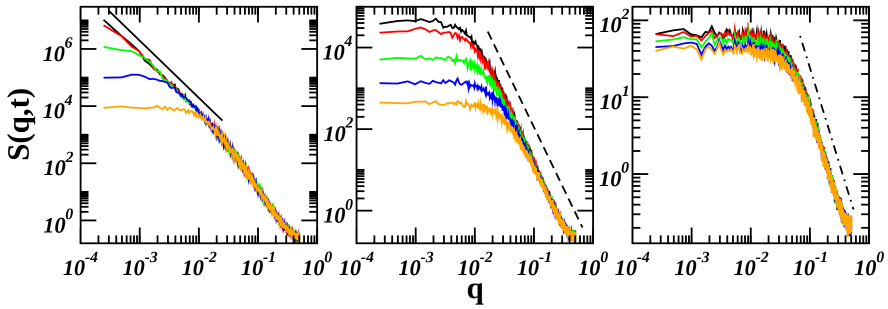

Figure 3.7: Evolution of the structure factor for temperatures $\widetilde{T} = 1.2, 0.24$ and 0.02 (from left to right) at different times $t = 10^4, 10^5, 10^6, 2 \cdot 10^6 mct$ (from bottom to top). Lines with exponent $-(2\alpha + 1)$ are plotted as a guide with $\alpha_{th} = 0.5$ *(solid)*, $\alpha_{eq} = 1$ *(dashed)*, and $\alpha = 0.75$ *(dot-dashed)*.

2005a], for which random-bond disorder is considered and thus $\alpha_{eq} = 2/3$ at equilibrated scales. This picture changes in the ultra-low temperature regime, at which the structure factor is also non-stationary but with a roughness exponent $\alpha \approx 0.75 \neq \alpha_{eq}$ below certain equilibration scale that grows extremely slowly in time. In this regime the movement of the interface is so slow that the discreteness of the model and the lack of up-down symmetry of the front motion in our model become relevant. Therefore, in the ultra low T regime, the behavior of the system is not expected to be described in terms creep relaxational dynamics.

To characterize the interface we can also attend to its multiaffinity. Many growth processes in random media give rise to multi-affine surfaces. Quenched disorder often leads to power-law distributed noise, that makes the interface roughness to exhibit different scaling exponents at different scales. A nice example is found in the SOD model belonging to the previously discussed DPD universality class [Sneppen and Jensen 1993] [*cf.* Sec. 3.1.2]. In order to analyze multiaffinity we compute the height-height q-correlation function $C_q(\ell) = \langle |h(x + \ell) - h(x)|^q \rangle^{1/q}$ for different values of q (Fig. 3.8). We observe that the same scaling $C_q(\ell) \sim \ell^{\alpha}$ holds for different values of q and the values of the exponents are in agreement with the roughness exponents observed in the structure factor scaling. This result rules out the existence of multiscaling in our model.

3.2.3 Activity statistics: Numerical results

Once we have identified the mentioned temperature ranges as different dynamical regimes we now focus on the typical activity patterns observed. The main advantage of the discrete model is that the activity can be directly examined. Any given site

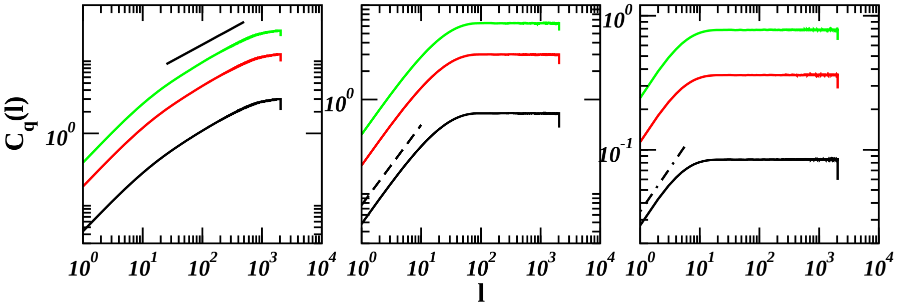

Figure 3.8: Correlation function $C_q(\ell)$ measured after 10^6 time steps for temperatures $\widetilde{T} = 1.2, 0.24$ and 0.02 (from left to right) and moments $q = 2, 3, 4$ (from bottom to top). Lines are plotted as a guide with exponent 0.45 *(solid)*, 0.85 *(dashed)*, and 0.65 *(dot-dashed)*.

$i \in [1, L]$ is active at time t if it is to be updated $h_i \to h_i + 1$ (*i.e.* if $v_i(t) > 0$) and inactive otherwise. The activity is therefore a binary variable taking values either 1 (moving) or 0 (resting) at each site. Typical patterns of activity are shown in Fig. 3.9 for $\widetilde{T} = 0.04, 0.24, 1.2$. A first thing to note is the high diversity in the density of active sites between the three plots. This corresponds to the different velocity regimes of the fronts at each temperature. Another important aspect is that the activity tends to be concentrated in clusters, as also does the inactivity (white areas). In order to characterize in a quantitative way the activity patterns we measure the statistics of the sizes of such clusters, *i.e.*, the spatio-temporal activity distribution. In the following we calculate the first-return time probability density, $P_f(\tau)$, and its counterpart for the distance between active sites $\mathcal{L}_f(\ell)$. As a complement, we also measure the probability of returning activity (not necessarily the first return), $P_r(\tau)$, and also the equivalent magnitude for the distribution of distances between any two active sites $\mathcal{L}_r(\ell)$.

Temporal statistics

First let us focus on the behavior of the time statistics. The activity temporal statistics can be determined by calculating the first-return time probability density function, $\mathcal{P}_f(\tau)$, which stands for the probability for a site to become active again after a period of inactivity τ. This probability describes the time intervals separating subsequent returns of activity at any given site.

As shown by Maslov et al. [1994] the average total number of return points $n(\tau)$ in a time interval τ is

$$n(\tau) = \tau - n(\tau) \int_1^\tau s\mathcal{P}_f(s)ds \, . \tag{3.23}$$

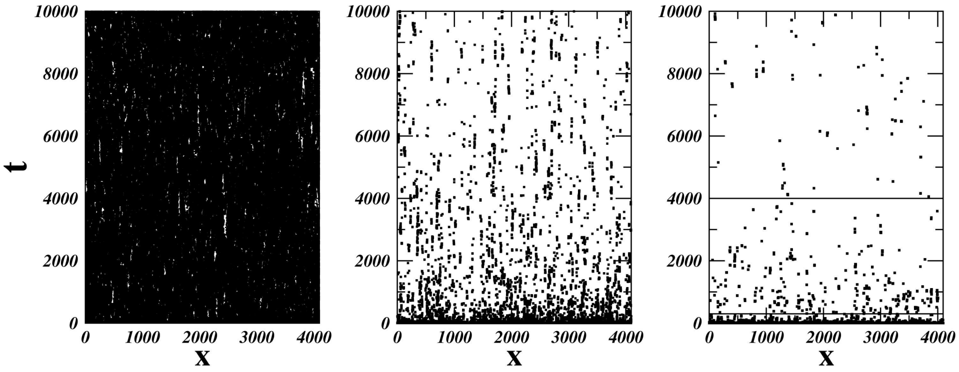

Figure 3.9: Activity patterns for a single realization of a system of size $L = 4096$ at different temperatures: $\widetilde{T} = 1.2$ (left), $\widetilde{T} = 0.24$ (center) and $\widetilde{T} = 0.04$ (right). The plots are $x - t$ maps where the active sites are marked in black. For the lowest temperature, $T = 0.04$ on the right, the moments at which the system describes the characteristic drop-offs are signalled by the horizontal black lines.

On the other hand, this quantity is also related to the fractal dimension D of return points, and in the long time limit $\tau \to \infty$ it can be written as $n(\tau) \sim \tau^D$ with $0 < D < 1$. Then for $D \to 1$ activity returns become dense in time, while for $D \to 0$ returns rarely occur.

In the case of a scale-invariant (fractal) activity the asymptotic distribution of first-return times decays as a power law, $P_f(\tau) \sim \tau^{-\beta_\mathrm{f}}$ for $\tau \gg 1$, with $1 < \beta_\mathrm{f} < 2$. Then, the scaling relation

$$D = \beta_f - 1 \tag{3.24}$$

connecting the fractal dimension of return points with the distribution of inter-event times can be obtained.

One can also consider the probability of returning activity (not necessarily the first return), $\mathcal{P}_r(\tau)$, defined as the probability that activity at certain site at time τ_0 will return to the same site after τ time steps [3].

This distribution can also be related to the average total number of return points

$$\mathcal{P}_r(\tau) = n(\tau + 1) - n(\tau) \; . \tag{3.25}$$

---

[3] Note that $\mathcal{P}_f(\tau)$ is a density probability function while $\mathcal{P}_r(\tau)$ is a probability with values constrained between zero and one. Both functions are conditional to the presence of activity at the initial measuring time.

So both local return time probabilities are related via $n(\tau)$ and from Eqs. (3.23) and (3.25) we have

$$\mathcal{P}_r(\tau) \sim [1 + \int_1^\tau s\mathcal{P}_f(s)ds]^{-1} \, . \tag{3.26}$$

This relation is always fulfilled no matter the functional forms of our time distributions. In the case of an activity pattern with fractal statistics in time, then both distributions exhibit power-law scaling, $\mathcal{P}_f(\tau) \sim \tau^{-\beta_f}$ and $\mathcal{P}_r(\tau) \sim \tau^{-\beta_r}$, and we have [Maslov et al. 1994]

$$\begin{aligned} \mathcal{P}_r(\tau) = n(\tau+1) - n(\tau) \sim (\tau+1)^D - \tau^D \sim \\ \sim \tau^{D-1} \sim \tau^{\beta_f - 2} \end{aligned} \tag{3.27}$$

that implies

$$\beta_f + \beta_r = 2. \tag{3.28}$$

This scaling relation suggests that fractal activity implies an infinite average return time $\langle\tau\rangle = \int_1^\infty s\mathcal{P}_f(s)ds$. However, as we shall see in detail in next section, the first-return time distribution can be directly related with the waiting time distribution between metastable states of the string (see Sec. 3.1.3). This implies that $\mathcal{P}_f(\tau)$ is bounded by an upper cutoff τ_{max} associated to the optimal excitation of the thermal activation process. Therefore, Eq. (3.28) is compatible with a finite average return time in the context of creep dynamics.

As $n(\tau)$ is simply the sum of all returns of activity to a particular site up to time τ, it can be easily related with the average instantaneous velocity of the system

$$v(t) \propto n(t+1) - n(t) = \mathcal{P}_r(t) \, . \tag{3.29}$$

This allows us to identify $\gamma = \beta_r$ whenever the distribution $\mathcal{P}_r(\tau)$ is a genuine power-law, *i.e.*, when $v_\infty \to 0$. In the case of creep motion v_∞ is expected to be small but finite and the equality becomes only approximate

$$\gamma(T) \approx \beta_r(T) \, . \tag{3.30}$$

Finally, from Eq. (3.29) we can also obtain the power spectrum of the velocity, $S(\omega) = \langle \widehat{v}(\omega)\widehat{v}(-\omega)\rangle$, in terms of the local return time distributions with $\widehat{v}(\omega) \propto \int_{-\infty}^{\infty} \mathcal{P}_r(\tau)\exp(2\pi i\omega\tau)d\tau$. If fractal activity is present then $S(\omega) \sim \omega^{-2(\beta_f - 1)}$. In the more general case of an exponential decay of the first-return time probability as $\mathcal{P}_f(\tau) \sim \tau^{-\beta_f}\exp(-\tau/\tau_\times)$ we have

$$S(\omega) \propto \langle \widehat{v}(\omega)\widehat{v}(-\omega)\rangle \sim \begin{cases} \omega^{-2(\beta_f-1)} & \text{if} \quad \omega \gg \omega_{\rm c} \\ \omega_{\rm c}^{-2(\beta_f-1)} & \text{if} \quad \omega \ll \omega_{\rm c}, \end{cases} \tag{3.31}$$

where the cut-off frequency is $\omega_c \sim \tau_\times^{-1}$.

These relations establish an interesting connection between the statistics of the local waiting times and the global dynamics of the interface. In the following we describe our numerical results concerning the local activity and the global velocity of the interface in the different dynamical phases.

In Fig. 3.10 we plot $\mathcal{P}_f$ and $\mathcal{P}_r$ for typical temperatures within these regimes. The measurements are done after a long enough transient from the initial condition and the distributions are stationary in the time span considered.

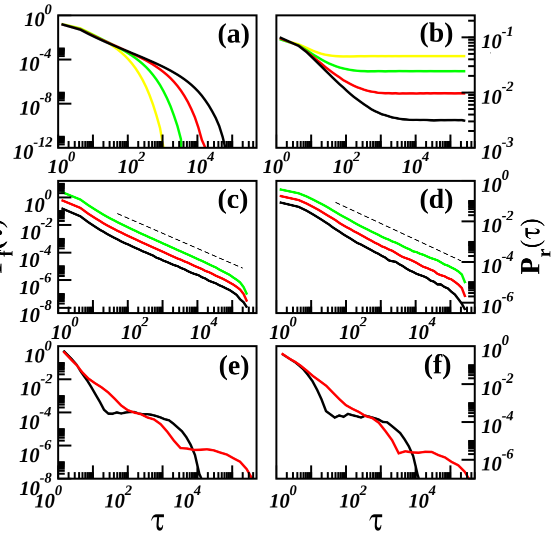

Figure 3.10: Activity statistics collected from 100 realizations in a system of size $L = 4096$. $\mathcal{P}_{\rm f}(\tau)$ is shown on the left panels and $\mathcal{P}_{\rm r}(\tau)$ on the right ones. High temperature regime *(a-b)* for $\widetilde{T} = 2$ (yellow), 1.2 (green), 0.8 (red), and 0.6 (black). Low temperature regime *(c-d)* for $\widetilde{T} = 0.28$ (green), 0.24 (red), and 0.20 (black). Curves are vertically shifted for clarity. Dashed lines with slope -1.1 in (c) and -0.8 in (d) are drawn for reference. Ultra-low temperature regime *(e-f)* for $\widetilde{T} = 2 \times 10^{-2}$ (red) and 4×10^{-3} (black).

At high temperatures, for which the front asymptotically reaches a constant velocity and thermal fluctuations dominate the dynamics, we observe an exponential decay of the inter-event times distribution preceded by a power-law decay at short τ, $\mathcal{P}_f(\tau) \sim \tau^{-\beta_f} \exp(-\tau/\tau_\times)$, where β_f and $\tau_\times$ vary with temperature [see

Fig. 3.10(a)]. We find that β_{f} varies from 1.3 to 1.5 for $\widetilde{T} = 0.6$ to $\widetilde{T} = 2$. The extent of the approximate power-law regime is bounded by $\tau_\times$, which enlarges with decreasing T. This distribution implies the existence of a finite average time $\langle \tau \rangle \propto \tau_\times$ for the activity to return at any given site. This behavior can be related analytically with the asymptotic functional form of the return probability

$$\mathcal{P}_r(\tau) \sim [1 + \int_1^\tau s^{1-\beta_f} \exp(\tau/\tau_\times) ds] \sim [1 + \tau_\times(T)]^{-1} , \tag{3.32}$$

which becomes a temperature dependent constant in the long time limit $\tau \gg \tau_\times$. This also implies $\gamma = 0$ and, therefore, a constant velocity. These analytical results are in excellent agreement with the results shown in Fig. 3.10(b) and Fig. 3.6(a).

As previously introduced, we can also attend to the temporal correlations of the interface global velocity. According to Eq. (3.31), it is expected to exhibit long-range temporal correlations in this regime of high temperatures. In Fig. 3.11 we plot $S(\omega)$ for several values of temperature within this high-temperature regime. All the spectra are obtained for a temporal range in which the signal is already stationary. We observe $S(\omega) \sim \omega^{-2D}$ with $2D \sim 1$ for $\omega \gg \omega_c$ and a crossover to pure thermal behavior $S(\omega) \sim \omega^0$ for $\omega \ll \omega_c$. In agreement with the behavior of the exponential cutoff of $\mathcal{P}_f(\tau)$ the typical frequency $\omega_c(T)$ increases with temperature.

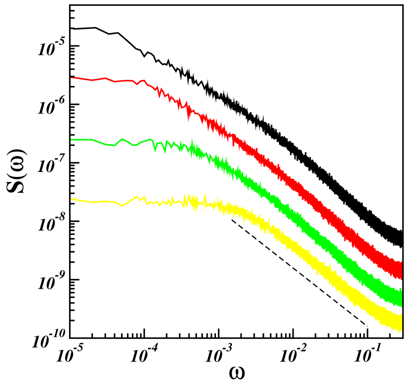

Figure 3.11: Spectral density of the velocity signal for a system of size $L = 4096$ at temperatures $\widetilde{T} = 2, 1.2, 0.8$ and 0.6 (from bottom to top). Curves are vertically shifted for clarity. Dashed line has slope -1.

The existence of a $1/\omega^{2D}$ velocity spectrum with $2D \approx 1.0$ within a range of high temperatures had already been observed in simulations of the QEW continuous model [Ramasco et al. 2006]. In that work velocity correlations were linked with the emergence of local temperature induced avalanches of depinning events. Now we show the connection between the local activity statistics and the global dynamics of the interface. At high temperatures thermal fluctuations are able to depin the interface and the velocity shows long-range correlations in time. When temperature is even higher this effect is washed out and the interface is in practice depinned from the disorder, so a flat spectrum $S(\omega) \sim \omega^0$ is observed in agreement with a pure thermal dynamics.

The pattern of activity changes substantially when temperature is decreased. For our simulation parameters, temperatures within the range $0.15 \lesssim \widetilde{T} \lesssim 0.40$ (intermediate regime) lead to a first-return time distribution that exhibits a power-law tail over several decades in time $\mathcal{P}_f(\tau) \sim \tau^{-\beta_f(T)}$, with an exponent $1 < \beta_f(T) < 2$. We shall see in detail in next section that this functional decay of $\mathcal{P}_f(\tau)$ can be directly related with the thermally activated jumps over energy barriers $U(\ell)$ that characterize the creep dynamics. On the other hand, this implies that $\mathcal{P}_r(\tau)$ also decays as a power-law (see Fig. 3.10(d)) and the relation given in Eq. (3.28) must hold. For instance, for typical values of the temperature within this dynamical regime we obtain $\beta_f = 1.12(5), 1.13(2), 1.15(1)$ and $\beta_r = 0.88(5), 0.86(6), 0, 80(7)$, for $\widetilde{T} = 0.20, 0.24, 0.28$, respectively. These results are in good agreement with the scaling relation $\beta_f + \beta_r = 2.0(1)$. They are also in fair good agreement with (but slightly different from) the velocity exponents γ observed for the same values of temperature [*cf.* Sec. 3.2.2], as expected due to the existence of a small but finite asymptotic creep velocity.

Finally, the activity statistics changes even further at ultra-low temperatures $\widetilde{T} \ll 0.15$. Both local return-time probabilities show sudden declivities at certain characteristic times [see Figs. 3.10(e) and (f)]. This behavior, similar to the one observed in other discrete glassy systems [Sibani and Littlewood 1993, Sibani and Dall 2003, Sibani and Jensen 2004], is to be compared with that observed for the average velocity in Fig. 3.6(e), which is indeed expected to be the same, $v(t) \propto \mathcal{P}_{\mathrm{r}}(t)$. For this ultra-low temperatures the space-time activity patterns reveal that the spatial distribution of events becomes very narrowly localized around a few sites that are co-active at the same time instant. In this case the discreteness of the model becomes relevant at any scale due to the sluggish dynamics of the front. The typical creep picture presented in Sec. 3.1.3 that describes the dynamics as coherent advances of regions L_{c} up to certain equilibration length $L(t)$ is not applicable here. The system stays out of equilibrium at all scales and the activity statistics is dominated by these very local events, giving rise to the characteristic downward jumps observed in Figs. 3.6 and 3.10.

Spatial statistics

A next question to take into account is the statistics of distances between active sites. We define the functions $\mathcal{L}_f(\ell)$ and $\mathcal{L}_r(\ell)$ as the counterpart of the distributions $P_f(\tau)$ and $P_r(\tau)$ we have employed to analyze the temporal statistics. These distributions are defined in terms of distances on the interface at a given time. The former represents the distribution of distances between active sites of the interface. The latter represents the probability of having activity at distance ℓ from a certain active site. In an analogous way to that in previous section to obtain Eq. (3.26) we get the following expression

$$\mathcal{L}_r(\ell) \sim [1 + \int_1^{\ell} s\mathcal{L}_f(s)ds]^{-1} , \tag{3.33}$$

that relates both distance distributions.

In the following we analyze the behavior of $\mathcal{L}_f(\ell)$ and $\mathcal{L}_r(\ell)$ at different temperatures. In order to make a similar analysis to that of time statistics, done for a time-window of 10^5 time steps, we analyze the distance distributions in a large system of $L = 131200$ sites. The measurements are done after a long enough transient from the initial condition.

In Fig. 3.12 the functions $\mathcal{L}_f(\ell)$ and $\mathcal{L}_r(\ell)$ are presented for typical temperatures within the different dynamical regimes. As we observed in the time-statistics analysis, at low temperatures both distributions exhibit a power-law decay, that reflects coherent advances of regions of the string due to thermal activation of the quasi-equilibrium barriers. However, as we mentioned before, these advances occur at scales below the equilibrium length $L(t)$. Because of this, $\mathcal{L}_f(\ell)$ and $\mathcal{L}_r(\ell)$ decay in a power-law fashion only up to this characteristic length. Above this scale, both functions become uniform distributions as corresponds to equiprobable distances between active sites. In the case of $\mathcal{L}_r(\ell)$ a slight increase is observed at long distances, that reflects the presence of several independent advances in the interface at the same time. The presence of this dynamical characteristic scale $L(t)$ makes us rule out the counterpart in distances of the scaling relation Eq. (3.28), which would correspond to fractal activity in distances.

On the other hand, in the high temperature regime thermal behavior of the interface growth dominates and we observe an exponential decay of $\mathcal{L}_f(\ell)$. This is connected by Eq. (3.33) with a uniform distribution $\mathcal{L}_r(\ell)$, in an analogous way to what we observed in the time statistics analysis.

Finally, no substantial changes are found when temperature is decreased from low to ultra-low values (compare Figs. 3.12(c-d) with Figs. 3.12(e-f)). So, whatever the dynamical features of this regime are, as long as the distance statistics of activity are concerned there are not important differences with the former one. There seems to be also certain typical scale that grows slower than $L(t)$ in the low temperature regime, as was also observed in the evolution of the structure factor shown in Fig. 3.7.

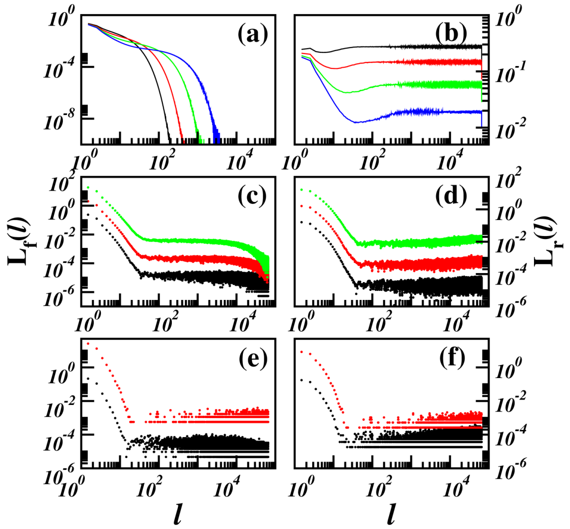

Figure 3.12: Activity statistics for distances collected from 100 realizations in a system of size $L = 131200$. $\mathcal{L}_f(\ell)$ is shown on the left panels and $\mathcal{L}_r(\ell)$ on the right ones. High temperature regime *(a-b)* for $\widetilde{T} = 2$ (blue), 1.2 (green), 0.8 (red), and 0.6 (black). Low temperature regime *(c-d)* for $\widetilde{T} = 0.28$ (green), 0.24 (red), and 0.20 (black). Ultra-low temperature regime *(e-f)* for $\widetilde{T} = 2 \times 10^{-2}$ (red) and 4×10^{-3} (black).

3.2.4 Theoretical arguments

A scaling theory can be developed to explain the activity statistics in our model at least for the region of moderate temperatures. For low temperatures, $T \ll U_{\mathrm{c}}$, one would expect the dynamics to be governed by thermally activated jumps over the energy barriers $U(\ell)$ that have to be overcome to equilibrate the system up to the length scale ℓ, which is the mechanism leading to the characteristic creep motion. In Sec. 3.1.3 we have described how creep dynamics can be connected with a power-law distribution of waiting times in Eq. (3.20). These waiting times between two consecutive metastable states can be related directly with the first-return times we have analyzed in our activity patterns. Then, we have the following distribution

$$\mathcal{P}_{\mathrm{f}}(\tau) \sim T \left(\frac{\tau_0}{\tau} \right)^{1 + aT/U_{\mathrm{c}}}, \tag{3.34}$$

where we can identify $\beta_{\rm f} = 1 + aT/U_{\rm c}$. This linear variation with T is consistent with our numerical results at low temperatures [Fig. 3.10(c)].

A distribution of first-return times as (3.34) would imply that the average return time $\langle\tau\rangle$ is infinite for $\beta_{\rm f} < 2$, *i.e.* for the low-temperature regime. However, as was previously mentioned, one can assume that there exists a cutoff of the first-return time distribution arising from the elastic nature of the problem. The creep behavior is controlled by the characteristic length scale $L_{\rm opt} = L_{\rm c}(f_{\rm c}/f)^{1/(2-\alpha_{eq})}$ corresponding to the optimal excitation that minimizes the free energy cost to nucleate such a perturbation [Chauve et al. 2000, Vinokur et al. 1996]. Therefore, during creep motion the average first-return time of the activity distribution is bounded from above by $\tau_{max} \sim \tau_0 \exp[U(L_{opt})/T]$. We then have $\langle\tau\rangle \sim \int_1^{\tau_{\max}} s\mathcal{P}_f(s)ds$, where $\mathcal{P}_f(s)$ at temperature T is given by Eq. (3.34). The stationary velocity can then be obtained as $v_\infty \sim \langle\tau\rangle^{-1}$ and satisfies the creep law of Eq. (3.16).

The fact that $\mathcal{P}_f(\tau)$ and $\mathcal{P}_r(\tau)$ are not 'pure' power-laws can also be considered to explain the evolution of the interface velocity in the long time limit. The existence of this cutoff at τ_{max} implies that $v(t)$ cannot decay as a a power-law unless the asymptotic creep velocity $v_\infty(f,T)$ is subtracted [*cf.* Fig. 3.6(c)], and then $v(t) - v_\infty \sim t^{\gamma(T)}$ in agreement with our results.

This interpretation of creep dynamics is also consistent with our results for the spatial statistics of the activity of the interface sites. Distance distributions decay as power-laws up to the equilibration length $L(t)$, which grows extremely slowly in time [Figs. 3.12(c) and (d)]. In fact, the value of this typical distance is consistent with the typical wavenumber $q^*(t)$ observed at the same instant in the structure factor of the interface [Fig. 3.7(b)], above which height correlations are given by the roughness exponent at equilibrium $\alpha_{eq} = 1$.

The situation is completely different for high values of temperature. In this regime thermal fluctuations are strong enough to renormalize the elementary pinning scales U_c and L_c [Nattermann et al. 1990, Müller et al. 2001]. Now the system evolves significantly faster toward the steady state due to stronger thermal fluctuations, and the constant values of the stationary velocity do not satisfy the creep law. In terms of activity statistics this regime implies the existence of finite average first-return time $\langle\tau\rangle$ independently of the value of L_{opt}. Then, from Eq. (3.34) one can define a depinning temperature $T_{\rm dep} \approx U_c(T_{\rm dep})/a$ separating the high-temperature and the low-temperature regions, and the distribution $\mathcal{P}_r(\tau)$ becomes bounded for $T \gg T_{\rm dep}$. In other words, the high temperature regime appears when $\beta_{\rm f}(T) = 1 + aT/U_{\rm c} < 2$ becomes $\beta_{\rm f} = 2$, implying the existence of a finite $\langle\tau\rangle$, and therefore $v \sim \langle\tau\rangle^{-1}$.

This scenario is consistent with our numerical results of time and distance statistics of the activity. Our inter-event distributions $\mathcal{P}_f(\tau)$ and $\mathcal{L}_f(\ell)$ exhibit exponential decays [*cf.* Figs. 3.10(a) and 3.12(a)], while their complementary distributions of all events, $\mathcal{P}_r(\tau)$ and $\mathcal{L}_r(\ell)$, become flat in the long-time limit. The functional form of the time distributions also leads us to establish an interesting connection between the statistics of the local waiting times with the global dynamics of the interface in Eq. (3.31). We observe long-range correlations of $v(t)$ that can be directly connected with the emergence of thermally induced local avalanches in coherence with the observed activity statistics in time.

The presented arguments allow us to understand the local activity statistics in the low and high temperature regimes and leads to conclusions consistent with our numerical results. However, such a line of reasoning based on energy barriers breaks down at ultra-low temperatures due to the up/down asymmetry that causes our model to be generically out-of-equilibrium in the absence of thermal fluctuations ($T \to 0$). Unfortunately, at this point we do not have a theoretical understanding of the dynamics in the ultra-low temperature regime. We claim that the dynamics of our model in this regime strongly resemblances to that observed in other discrete disordered systems with glassy behavior by Sibani and co-workers [Sibani and Littlewood 1993, Sibani and Dall 2003, Sibani and Jensen 2004], which is still poorly understood on general grounds.

3.2.5 Nonlinear contributions

The study of nonlinear contributions to the elasticity should allow a better understanding of the glassy properties of more realistic elastic models. As previously pointed in Sec. 3.1.2, nonlinearities may emerge, for instance, from the anisotropy of the medium randomness. Thus the interest of such analysis is clear, especially for many experimental setups. However, the scenario for the QKPZ dynamics in presence of non-negligible thermal fluctuations is still an open question and only a few attempts to clarify it have been carried out up till now [Ramasco et al. 2006]. Although we are not able to formulate any theoretical framework for the nonlinear case, in this section we provide a first insight into this scenario from the analysis of the local activity statistics. It could be considered as a counterpart survey of the analysis provided by Ramasco et al. [2006].

The inclusion of nonlinear corrections up to the lowest order in ∇h in the growth equation leads to Eq. (3.15), which in terms of our discrete automaton model implies

$$\begin{aligned} v_i(t) &= \kappa\,(h_{i+1} + h_{i-1} - 2h_i) + \lambda\,(h_{i+1} - h_{i-1})^2 + \\ &\quad + \Delta^{1/2}\,\eta_i(h_i) + T^{1/2}\,\varepsilon_i(t) + f\,, \end{aligned} \tag{3.35}$$

where $v_i(t)$ is again evaluated at time $t > 0$ for all sites, and $h_i(t+1) \to h_i(t) + 1$ if $v_i(t) > 0$. The parameters are fixed to $\kappa = 10$, $\Delta^{1/2} = 20$, $\lambda = 1$, and $f \approx 10^{-2} \times f_c(T = 0)$. The dimensionless temperature remains as $\widetilde{T} = T(\kappa/\Delta^2)^{1/3}$.

Due to the nonlinear effect the activity rapidly spreads laterally, giving rise to considerably different activity patterns to that the linear case. In contrast with the $\lambda = 0$ case, the thermally induced bursts of activity tend to overlap with the previous ones, giving rise to spatially extended events that correlate the interface at large scales. We observe that for a range of intermediate temperatures around certain $\widetilde{T}_{opt} = 0.032$ such correlation length extends over the whole system $\xi \sim L$ and the avalanches cover a macroscopic region of the system.

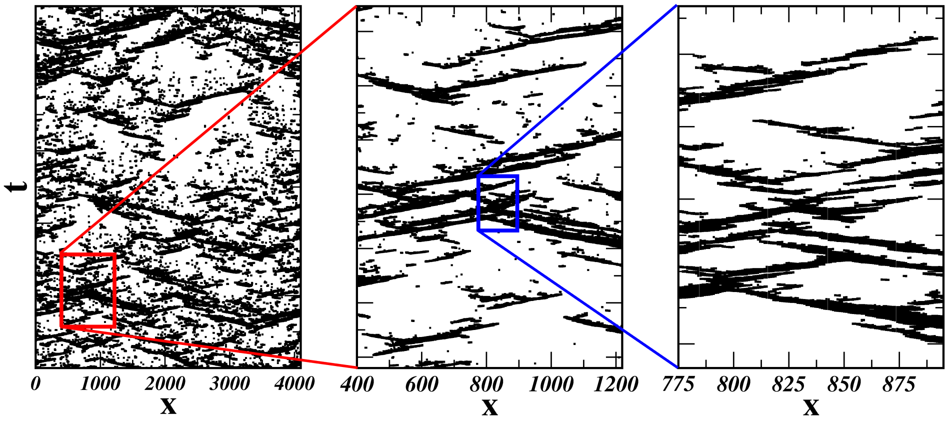

Figure 3.13: Activity pattern for a single realization of a system of size $L = 4096$ at temperature $\widetilde{T}_{opt} = 0.032$ and $\lambda = 1$. The left panel shows the whole system activity during a time span of 10^5 steps after a long enough transient from the initial condition. The remaining panels are cross-sections at scales 0.2 (middle) and 0.03 (right). The fractal structure of the avalanches is evidenced as the rescaled sections seem to exhibit the same statistical properties as the original one.

In Fig. 3.14 we plot the structure factor of the interface for several values of the temperature after a transient long enough from the initial conditions. While for high temperatures a crossover to pure thermal behavior is observed, with $\alpha_{th} = 0.5$, at $\widetilde{T}_{opt}$ we observe that spatial correlations extend the whole system, with a roughness exponent $\alpha = 0.67$ that, in agreement to that observed by Ramasco et al. [2006], remains the same for a considerable range of temperatures around $\widetilde{T}_{opt}$.

Finally we analyze how these thermally induced avalanches affect the global velocity of the interface. As previously observed in the linear case, there are large correlations due to the presence of the bursts of activity. In Fig. 3.15 we show the

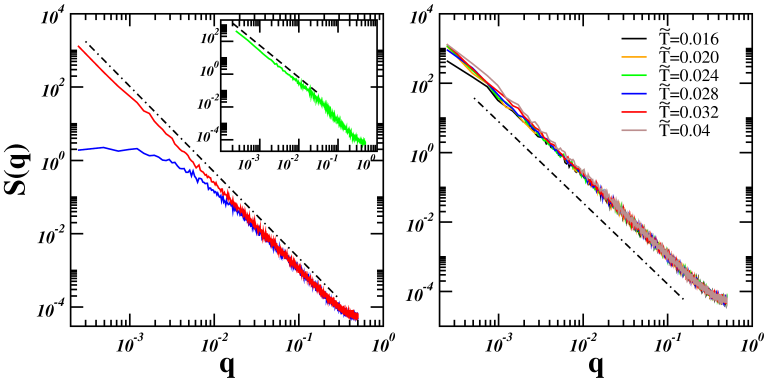

Figure 3.14: Structure factor of an interface of size $L = 4096$. On the left the spatial power spectra is shown for high, low and ultra-low temperatures. At $\widetilde{T} = 0.4$ (green) pure thermal behavior is observed with $\alpha_{th} = 0.5$. At ultra-low temperature $\widetilde{T} = 0.004$ (blue) the unlikely avalanches are not enough to correlate the interface, but at temperature $\widetilde{T}_{opt} = 0.032$ (red) such thermally induced events correlate the whole interface. On the right we plot the structure factor for a range of intermediate temperatures around $\widetilde{T}_{opt}$. Dashed line in the inset has slope $(2\alpha + 1) = 1.95$ and dot-dashed line $(2\alpha + 1) = 2.34$.

spectral density of the velocity signal for several values of temperature. In the low frequency limit we observe a power-law decay $S(\omega) \sim \omega^{-\chi(T)}$. For ultra-low temperatures $T \ll T_{opt}$ the signal velocity is uncorrelated with $\chi \approx 0$, while for high temperatures $\chi \approx 1/3$ as corresponds to a freely moving KPZ interface [Krug 1991]. At intermediate temperatures we indeed observe long-range temporal correlations with $\chi(T) \approx 1.5$ within a quite extent region around $\widetilde{T}_{opt}$.

3.3 Conclusions

In this chapter we have introduced a discrete model to study the local activity statistics of a forced elastic interface in heterogeneous media at a finite temperature. The model presents an up/down movement asymmetry that renders the model out-of-equilibrium in the limit of zero temperature. The system exhibits three dynamical regimes, two of which are equivalent to the ones observed in the QEW continuous elastic model. Thanks to the discrete character of our model, the activity becomes a binary variable and can be precisely tracked in space and time. The model shows significant differences of the activity patterns in the three regimes, being specially interesting those corresponding to the intermediate and low temperature regimes. In order to analyze in a quantitative way these activity patterns, we have defined the

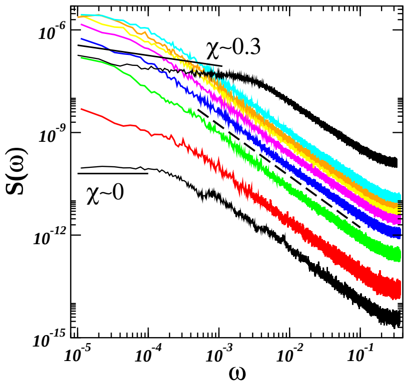

Figure 3.15: Spectral density of the global velocity of the interface. Colored spectra correspond to intermediate temperatures $\widetilde{T} = 0.016, 0.020, 0.024, 0.028, 0.032, 0.36,$and 0.04 (from bottom to top). Black spectra correspond to ultra-low and high temperatures, with $\widetilde{T} = 0.004$ (bottom) and $\widetilde{T} = 0.4$ (top) respectively. The dashed line has slope -1.5.

spatio-temporal distributions of the first-return and all-returns of activity. We find that these probabilities show a power-law decay in the intermediate regime with exponents that depend on temperature. Simple scaling arguments based on an exponential distribution of energy barriers lead us to propose an expression for the temporal probability distributions of activity in good agreement with simulations. The non-equilibrium character of the model becomes relevant as the temperature is decreased toward zero and the quasi-equilibrium arguments fail to describe the dynamics. In this ultra-low temperature regime the activity statistics is similar to that observed in certain discrete glassy systems [Sibani and Littlewood 1993, Sibani and Dall 2003, Sibani and Jensen 2004].

One of the main results presented in this chapter concerns the novel approach to study the problem of the relaxation of the driven elastic string in terms of the local activity and avalanche statistics. We show that activity statistics is directly connected with the interface velocity, the power spectrum $S(\omega) \sim 1/\omega^{\chi}$ of velocity fluctuations, and the structure of avalanches of activity. Our analysis provides global dynamical information from a local observable. We expect this can be useful in experiments, in particular in those cases where only local proves can be used to obtain information about the position of the interface.

Part II

Sociophysics

CHAPTER

4 Introduction to social models

4.1 Introduction

The application of Statistical Physics methods to social phenomena has recently attracted the attention of theoretical physicists. Statistical Mechanics teaches us that, even when it is impossible to foresee what a single particle will do, one can often predict how a sufficiently large number of particles will behave. One may conjeture that this can also be applicable to societies made of many individuals which interact mostly locally with each other, like in classical statistical mechanical systems. This approximation is probably too ambitious as social interactions are not mechanical, but complex and hardly reproducible. Therefore these models cannot - and do not pretend- reproduce the real Society. However, we expect that some aspects of collective behavior and self-organization in a society may be reasonably well described by means of simple statistical models. In recent years a number of such models have been introduced and analyzed, giving rise to the new field of *Sociophysics*. In contrast to classical systems studied by Statistical Physics, the *particles* (agents) and *interactions* of a human society are not of an elementary but of a highly complex nature. In many cases the thoughts, emotions and intentions of a single individual are as complex as the complexity of the brain itself. Another fundamental difference is that in physico-chemical systems the interactions lead to a blind, unintended self-organization of the system , whereas the nature of interactions in sociology leads, at least partially, to intelligent 'planed' structures. In order to have a useful and, therefore, still sufficiently simple quantitative theory, those sociologic phenomena have to be excluded and the full complexity of human behavior and interactions have to be taken into account in the sense of a comprehensive *microscopic theory*. Sociophysics studies phenomena where- at the level of the single individual- a complex mixture of fluctuating rational considerations, emotional preferences and motivations finally merge into one of relatively few well demarcated resultant *attitudes*. Social systems can then be quite well described at this level by Langevin and Fokker-Planck equations where the interactions between individuals or agents can be understood as the deterministic contribution, while the fluctuations due to political evolution, economics, etc. are embraced in stochastic terms.

These systems can also be treated as agent-based models by means of simulations based on the global consequences of local interactions of individuals. The origin of agent-based modeling can be traced back to the 1940s with the introduction by Von Neumann and Ulam of the notion of cellular automaton models [Neumann 1966, Ulam 1960]. These individual-based models were primarily used for social systems by Reynolds [1987], who tried to model the behavior of a flock of geese. In such models the individuals might represent plants and animals in ecosystems, vehicles in traffic, people in crowds, or autonomous characters in animation and games. The agents interact in a given environment according to *procedural rules* tuned by characteristic parameters, and the characteristics of each individual are tracked through time. This stands in contrast to modeling techniques where the characteristics of the population are averaged together and the model attempts to simulate changes in these averaged characteristics for the whole population. Some of these individual-based models are also spatially explicit since the individuals are associated with a location in geometrical space or their position on a specified network. In this case the models can also exhibit more complex features as, for instance, mobility of the individuals around their environment (this would be a natural model, for example, of an animal in an ecological simulation).

The number of different issues that Sociophysics embraces is quite large. The most studied are probably *language dynamics* [Milroy 1960, Abrams and Strogatz 2003, Stauffer and Schulze 2005, Stauffer et al. 2007, Wang and Minett 2005, Baxter et al. 2006], *cultural dissemination* [Axelrod 1997, Axelrod and Hamilton 1981; 2005, Castellano et al. 2000, Deffuant et al. 2000, Laguna et al. 2003, Vazquez and Redner 2007] and *opinion dynamics* [Sznajd-Weron and Sznajd 2000, Slanina and Lavicka 2003, Schulze 2003, Fortunato 2004, Bernardes et al. 2002, Galam 2004, Stauffer and Martins 2004, Krapivsky and Redner 2003]. Other interesting topics deal with crow dynamics, the emergence of hierarchies or traffic. Sociophysics is also deeply related with other fields as Evolutionary Game Theory or Econophysics.

In the following some examples are presented to provide a general overview of the different topics in this field (opinion formation is excluded here, to be presented in detail in the following section).

Language dynamics

The similarity of the evolution of human languages to biological evolution of species is utilized to study the rise or fall of language use inside large groups of individuals. Like species, a language can split into several languages, it can mutate, by modifying words or expressions over time, or it can face extinction. Such similarities have fostered the application of models used to describe biological evolution in a language competition context. These models can be based on macroscopic differential equations (similar to *Lotka-Volterra* equations) or by microscopic Monte-Carlo simulations, where the state of each individual is monitored in time, incorporating the birth, maturity and death of individuals. This very old idea of describing language evolution as being similar to the evolution of biological species has been recently quantified by Sutherland [2003].

A well-known example of language competition modeling was proposed by Abrams and Strogatz [2003]. Their study considers a two-sate society, *i.e.*, a community in which there are speakers of either a language X or a language Y. They describe the competitive evolution of both languages in the community by means of a Lotka-Volterra equation. Considering a constant population of N individuals where everybody speaks one of the two languages, the dynamics is given by the simple rate equation

$$\frac{dx}{dt} = (1-x)x^a s - x(1-x)^a(1-s) \; , \tag{4.1}$$

where x is the fraction of the population that speaks X and the fraction of Y speakers is given by $y = 1-x$. The parameter s, with $0 < s < 1$, gives the relative status (prestige, usefulness) of language X (for Y it will be $1-s$) and a is some positive exponent. The above equation thus describes how people switch from one language to the other one. Y speakers switch over to language X with a rate proportional to $x^a s$ (the complementary way to switch from X to Y). The factor x^a takes into account that people prefer to switch to a widely spoken language from a rare language.

This model predicts that one language will die out and the other will be spoken by everybody. The dynamics has only two stable fixed points, corresponding to $x = 0$ and $x = 1$. There is a third fixed point, corresponding to $x = 1/2$ and $s = 1/2$, when both languages are equivalent. However, it is unstable as confirmed by numerical simulations of a microscopic version of the model on different graph topologies [Stauffer et al. 2007]. These results are illustrated in Fig. 4.1. In sum-

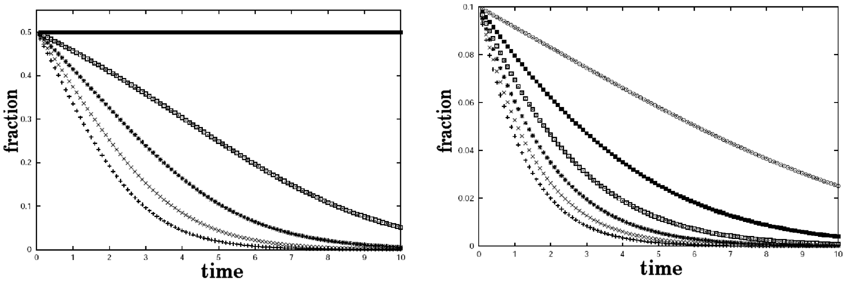

Figure 4.1: Fraction of population speaking first language (X) in the two-language model of Abrams and Strogatz. *Left:* Symmetrical initial distribution with $x(t=0)=1/2$, $a=1.31$, and $s=0.1, 0.2, 0.3, 0.4, 0.5$ (from bottom to top). The fraction x decays rapidly for small values of the $s<1/2$ parameter while for $s=1/2$ both languages are equally strong and nothing changes. For larger $s>1/2$ the other language dominates in a symmetrical behavior. *Right:* Initial distribution favors one of the languages, with $x(t=0)<1/2$, $a=1.31$ and $s=0.1, 0.2, 0.3, 0.4, 0.5, 0.6$ (from bottom to top). In this case x decays toward zero even for $s=0.5$ and 0.6. Only for $s=0.7$ and above x approach unity in the final state. From Ref. [Stauffer and Schulze 2005].

mary, simulations of this model predict that one of the two languages wins, and this is the language which is favored by a larger initial population or a more favorable status s. In their seminal paper, Abrams and Strogatz tested the model with real data on the proportion of speakers over time collected from 42 different regions of Peru, Scotland, Wales, Bolivia, Ireland and Alsace-Lorraine. They showed that the model is able to reproduce the decrease in time of the number of speakers of various endangered languages.

Several modifications of the model have been proposed to consider richer language dynamics. For instance, in Ref. [Mira and Paredes 2005] bilingual speakers were introduced in the original Abrams-Strogatz model. In this case the system reaches a steady state characterized by the coexistence of one group of monolingual speakers with a group of bilinguals. Monolingual speakers of the endangered language are bound to disappear, but the survival of the language is ensured by bilingualism. In [Patriarca and Leppänen 2004] the effect of population density is introduced, by turning the rate equation Eq. (4.1) into a reaction-diffusion equation. In this version people can move on a plane divided in two regions, and in each of them one language has a higher status that the other one, respectively. The system converges to a stable configuration where both languages survive, although they are mostly concentrated in the zones where they are favored.

Cultural dynamics

A large number of models have been recently proposed to describe cultural and population dynamics [Axelrod 1997, Castellano et al. 2000, Deffuant et al. 2000, Laguna et al. 2003, Vazquez and Redner 2007]. As an example, we briefly introduce here a cooperation model introduced by Axelrod and Hamilton [2005; 1981] in which interaction between peers of different cultural groups lead to a tendency toward cooperation between similar featured agents.

An open system is considered on a square lattice and the agents are labeled with three different tags; the first one specifies its group membership (the original version of the model considers four different cultural groups), the second one specifies its tendency to cooperate or defect with the agents from its own cultural group, and the third one quantifies the tendency to cooperate with individuals from different cultural groups. Four different strategies are then observed, namely *ethnocentric* (only in-group cooperation), *generous* (collaboration with any individual), *egoist* (non collaboration), and *mole* (only out-group collaboration).

The simulation begins with an empty space. At each time period the system is updated considering several phenomena:

- *Immigration*: A new agent with random traits enters at a randomly empty site.

- *Reproduction*: Each agent creates analogous individuals at the adjacent sites with probability R and considering certain probability for an aleatory mutation M.

- *Interaction*: Each pair of neighbors interact according to the one-move Prisoner's Dilemma in which each one chooses (independently) whether or not to cooperate with the other. Cooperation has a cost, namely a fixed decrease of the reproductive capability R in a fraction n. In contrast, receiving help increases R in $m > n$.

- *Death*: Each individual dies with certain probability.

This simple rules lead to a dominance of ethnocentric strategy even when favoritism toward similar others is not built in to the model. Fig(4.2) shows how a run of the model looks like. After a large time span the model exhibits a great predominance of the ethnocentric strategy.

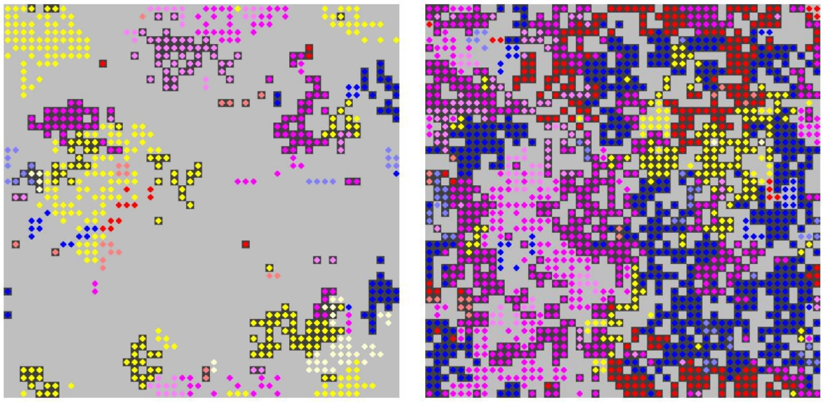

Figure 4.2: A typical run of the model after 100 periods (left) and 2000 periods (right). The shading of the foreground of a cell indicates the agents strategy toward others of its own color, with a dark dot indicating cooperation. The shading of the background of a cell indicates the agents strategy toward agents of other colors, with black indicating defection. Thus agents using the ethnocentric strategy have a dark dot on a black background, and egoist agents have a light dot on a black background [Axelrod and Hamilton 1981].

4.2 Opinion formation models

The spread and evolution of opinions in a society has always been a central topic in Sociology, Politics and Economics. Among other aspects, the building (or the lack) of consensus in social systems has been focus of much interest. The first opinion dynamics designed by a physicist was a model proposed in 1971 by Weidlich [1971]. Later on Ising-like models made their first appearance in opinion dynamics [Galam et al. 1982, Galam and Moscovici 1991], in which the spin-spin coupling represents the pairwise interaction between agents. Since then a number of models have been considered in order to mimic the dynamics of consensus in opinion formation [Sznajd-Weron and Sznajd 2000, Slanina and Lavicka 2003, Schulze 2003, Fortunato 2004, Bernardes et al. 2002, Galam 2004, Stauffer and Martins 2004, Krapivsky and Redner 2003]. They are basically cellular automata, where one starts by assigning, usually at random, a set of numbers to any of the N agents of a community. One of these numbers is the opinion, and the others may describe specific features of the agents, like persuasiveness, tolerance, etc. Society is modeled as a graph, and each agent interacts with its graph neighbors. The procedure is iterative: at each iteration one takes a set of interacting agents and updates their opinion according to a simple dynamical rule. After many iterations, the system usually reaches a state of static or dynamic equilibrium. The dynamics usually favors the agreement of groups of agents about the same opinion, so that one ends up with just a few opinions in the final state. In particular, it is possible that all agents share the same opinion *(consensus)*, or that they split in two or more factions. Here we briefly present some basic types of opinion formation models.

4.2.1 Voter model

A well established model class is known as the Voter Model (VM). It is based on the idea that the adoption of a given *opinion* (behavior, attitude) depends on its frequency in the neighborhood. VM is possibly the minimal model for opinion spreading and one of the simplest models of nonequilibrium statistical mechanics with nonconserved dynamics. It is defined as a set of N *voters* with two opinion states (or spin) $s_i = \pm 1$ located at the nodes of a graph. The elementary dynamical step consists in randomly choosing one node and assigning to it the opinion, or spin value, of one of its nearest neighbors, also chosen at random. This dynamics describes a coarsening process driven by interfacial noise. In sociophysical terms it mimics the homogenization of opinions through the confrontation of peers and reflects a complete lack of self-confidence of the agents.

The asymptotic behavior of the ordering process highly depends on the dimension of the graph where the dynamics is defined. On regular graphs of dimension $d \leq 2$ the system eventually converges to an ordered state with all agents sharing the same opinion. This is an absorbing state since the system cannot escape from it once it is reached. In this case the time needed to reach consensus scales as $\tau \sim N^2$ for $d = 1$ and $\tau \sim N \ln N$ for $d = 2$. On regular lattices with $d > 2$ (as well as in small-world networks and scale-free graphs) the VM dynamics is unable to order the system in the thermodynamic limit of large systems. Starting from a random initial condition and after an initial transient the system falls in a metastable partially ordered state. Therefore the critical dimension of the VM is $d_c = 2$ [Krapivsky and Redner 2003, Krapivsky 1992]. However, in a finite system this metastable state has a finite lifetime, as a finite fluctuation takes the system from the metastable state to one of the two absorbing states. Therefore, the average consensus time for a finite system above the critical dimension is given by $\tau \sim N$. A standard order parameter to describe the ordering dynamics is the average interface density, $\rho_m(t)$, defined as the fraction of links connecting sites with different spin value. These connections form the surface where the interfacial coarsening process takes place. In the coarsening-phase (where $\rho_m(t) \to 0$ when $t \to \infty$) the asymptotic regime toward the ordered state is characterized in $d = 1$ by a power law $\rho_m(t) \sim t^{-1/2}$, while at the critical

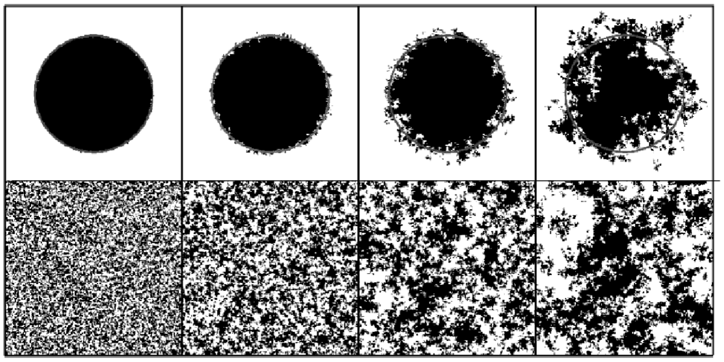

Figure 4.3: Illustration of the domain growth in the two-dimensional VM for a system of size 256×256 sites. *Top:* Evolution at different times from an initial compact bubble of opinion $(+)$ (agents with opinion $(-)$ are depicted in white). *Bottom:* Same from symmetric random initial conditions. Ref. [Dornic et al. 2001].

dimension $d_c = 2$ a slow logarithmic decay is found $\rho_m(t) \sim 1/\ln t$ [Dornic et al. 2001].

In the VM temperature is absent but since the dynamics is noiseless (only interfacial noise is present) it works at zero temperature in nature. However, the critical temperature is also zero. If one introduces noise, by allowing spontaneous changes of opinion, the system does not coarsen in any dimension [Ben-Naim et al. 1996], even for $d < d_c$.

This model has been widely studied in many different versions and dimensions [Castellano et al. 2003], mostly due to its intrinsic interest in non-equilibrium statistical mechanics. The reasons for its success are simplicity (the intuitive 'convincing' rule) and the profound relationship with other non-conserved coarsening processes, as for instance the Ising model with Metropolis dynamics at $T = 0$ (Glauber kinetic Ising model). In both models the dynamics gives rise to coarsening patterns characterized by a correlation length $\xi(t) \sim \sqrt{t}$. However in Glauber dynamics phase competition is driven by surface tension and the interface density decays as $\rho_m(t) \sim 1/\xi(t) \sim t^{-1/2}$ while in the VM with $d > 1$ this surface tension is absent. Only in $d = 1$ both models are actually equivalent [Ben-Naim et al. 1996].

4.2.2 Social impact models

The psychological theory of *social impact* describes how individuals feel the presence of their peers and how they influence other individuals. The impact of a social group on a subject can depend on the number of individuals in the group, on their convincing power, or on the distance from the subject (where the distance may refer both to spatial proximity or to the closeness in an abstract space of personal relationships). The first mathematical model to describe social impact effect was introduced by Latané [1981]. In this model each individual is characterized by two random parameters that estimate the strength of its action on the others: persuasiveness p_i and supportiveness s_i. They describe the capability to convince someone to change or keep its opinion, respectively. These parameters conform the total impact I_i that an individual i experiences from its social environment. Then an individual state flips if the pressure in favor of the opinion change overcomes the pressure to keep the current opinion.

Other models have been proposed to account for more complex processes related with social impact [Kohring 1996, Bordogna and Albano 2007, Holyst et al. 2001]. Probably the most popular one that studies social impact effects is the Szanjd model [Sznajd-Weron and Sznajd 2000], based on the idea that the impact exerted by a social group on an individual depends on the size of such group.

Sznajd model

One starts with a simple observation: an individual is more easily convinced to change its mind if more than just a single person tries to persuade him. This tendency of any individual to imitate the behavior observed in large enough groups is called *social validation*. In their original paper, Sznajd-Weron and Sznajd proposed a two states $s_i = \pm 1$ Ising-like spin model considering this particular effect of social impact [Sznajd-Weron and Sznajd 2000]. They defined a one dimensional chain with periodic boundary conditions where each spin (or lattice site) $i = 1, ..., N$ interacts with its neighbors following two basic rules:

Rule 1: If two consecutive lattice sites have the same opinion, $s_i \times s_{i+1} = 1$, then $s_{i-1} = s_i = s_{i+1} = s_{i+2}$.

Rule 2: If two consecutive lattice sites have a different opinion, $s_i \times s_{i+1} = -1$, then $s_{i-1} = s_{i+1}$ and $s_{i+2} = s_i$.

So, if the pair of agents share the same opinion, they successfully impose their opinion to their neighbors (this rule resembles ferromagnetism). However, if the two agents disagree, each agent imposes its opinion to the other agent's neighbor (as in anti-ferromagnetism). Opinions are updated in a random sequential order. Starting from a totally random initial configuration, two types of stationary states are found, corresponding to either *consensus*, with all spins up ($m = \sum_i s_i/N = 1$) or down ($m = -1$), or to a *stalemate*, with the same number of up and down spins

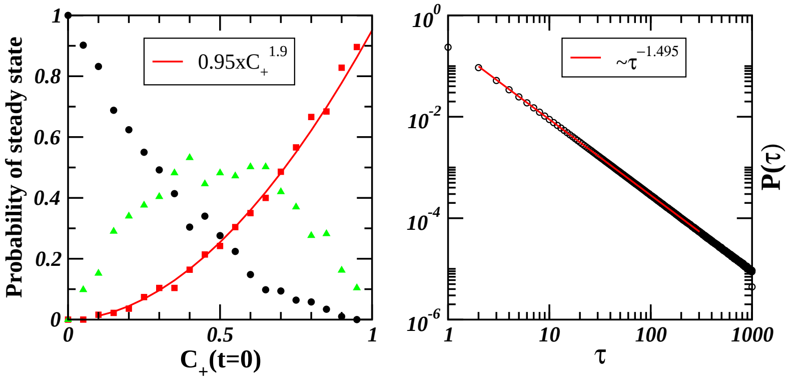

Figure 4.4: *Left:* Dependence between initial concentration of supporters of opinion $(+)$, $C_+(t = 0)$, and the probability of reaching the steady state $m = +1$ (*squares*), $m = 0$ (*triangles*), or $m = -1$ (*circles*). Even a relatively small group can make the system go to the stalemate state. However, to win the group has to be greater (to have the 50% of probability to win the initial concentration has to be of 70%). *Right:* Decision time distribution exhibit power law behavior with exponent ≈ -1.5. Picture by the present author, based on the original paper by Sznajd-Weron and Sznajd [2000].

in antiferromagnetic order ($m = 0$). The latter is a consequence of the second rule, which favors antiferromagnetic configurations, and has a probability $p = 1/2$ to be reached when both opinions are equally distributed in the initial configuration. In these conditions each of the two consensus states occurs with probability $p = 1/4$. In a more general case, the dependence between the final state and the initial concentration of supporters is shown in Fig. (4.4). The relaxation time of the system into one of the three possible attractors has a log-normal distribution [Behera and Schweitzer 2003]. It was also observed that a change of opinion is usually followed by further changes, and these periods of frequent changes are followed by periods of stagnancy. Indeed, the decision time, which is the time that an agent needs to change its opinion, decays as a power-law in time $P(\tau) \sim \tau^{-3/2}$. The fraction x of individuals who never changed opinion decays also as a power-law in time, $P_x(t) \sim t^{-3/8}$, with the same exponent as the 1-d Ising model.

However, the original Sznajd model does not satisfy the principle of social validation that intends to represent (that was enunciated as “United we stand and divided we fail”). It has been proved in Ref. [Behera and Schweitzer 2003] that the Sznajd model in one dimension is equivalent to a voter dynamics in which each spin is influenced by its next-nearest-neighbor. Therefore, the original Sznajd model does not exhibit the features that motivated its introduction, as each spin is influenced only by a single spin, not by a pair. On the other hand these rules lead to a quite unrealistic antiferromagnetic state in terms of a real community (although it is possible in other spin systems). Because of this, the second rule was soon replaced in subsequent versions of the model. In the most popular alternative only the ferromagnetic rule holds, so the neighbors of a disagreeing agents pair maintain their opinions [Sznajd-Weron and Sznajd 2000]. Other possibility was proposed by Sánchez [2004], in which each spin of the disagreeing peer convinces its own neighbor (that is, if $s_i s_{i+1} = -1$, then $s_i = s_{i-1}$ and $s_{i+1} = s_{i+2}$). These versions of the model exhibit similar behavior as the original one with the exception of the antiferromagnetic steady-state. In this case the final state is clearly determined by the initial configuration: if the initial magnetization is $m > 0$ ($m < 0$) the system always attains consensus with $m = +1$ ($m = -1$).

An exact solution for the Sznajd-like dynamics on a complete graph was later derived by Slanina and Lavicka [2003]. These results were obtained for the simplified "two against one" version. If two agents, randomly taken, are in agreement they are able to convince to another randomly chosen agent, otherwise nothing hapens. The evolution equation for the probability density $P(m,t)$ that the system has magnetization m at time t reads:

$$\frac{\partial P(m,\tau)}{\partial \tau} = -\frac{\partial}{\partial m}\Big[(1-m^2)mP(m,\tau)\Big] \, . \tag{4.2}$$

The general solution of this equation is

$$P(m,\tau) = [(1-m^2)m]^{-1} f\left(e^{-t}\frac{m}{\sqrt{1-m^2}}\right) , \tag{4.3}$$

where the function f depends on the initial conditions. In the particular case $P(m,\tau = 0) = \delta(m - m_0)$ the distribution $P(m,t)$ is a δ-function at any moment of the evolution. It drifts toward the extremes $+1$ if $m_0 > 0$ or -1 if $m_0 < 0$. This analysis properly recovers the above exposed results obtained by means of numerical simulations. The average time to reach the steady state of the system, starting from an initial fraction p of 'up' spins, can also be deduced from Eq. (4.2):

$$\langle \tau_{st} \rangle \simeq -\ln\left(\frac{|2p-1|}{\sqrt{p(1-p)}}\frac{1}{\sqrt{N}}\right) , \tag{4.4}$$

which diverges for $p \to 1/2$ according to the presence of a phase transition at $m_0 = 0$.

Later modifications of the model have certainly brought the Sznajd model closer to reality, for instance by changing the topology of the chain to more complicated structures like two dimensional lattices [Stauffer et al. 2000], scale free networks

[Bernardes et al. 2002, Sousa 2005] or a fractal structure coming from percolation [Moreira et al. 2001]. Another step toward a realistic model for opinion dynamics has been done by increasing the range of interactions [Schulze 2003] and the number of agent states [Sznajd-Weron and Sznajd 2005, Fortunato 2004].

4.2.3 Majority rule models

This class of opinion models includes all the models in which the process of opinion formation is favored by a majority or minority opinion. Some of them are defined in terms of a single spin that adopts the majority/minority opinion in its neighborhood. For instance the model proposed by Ligget [1985], in which a single spin takes with probability q (or $1-q$) the sign of the minority (or the majority) of its neighbors. Also the Klimek model [Klimek et al. 2007], where an agent is convinced if there is at least a fraction p of its neighbors sharing the same opinion. In some other majority rule models the whole system is splitted in discussion groups in which majority/minority tendencies dominate the dynamics [Krapivsky and Redner 2003, Mobilia and Redner 2003]. Among all these models, probably the most studied one is the introduced by Galam [1990].

Galam model

The simplest version of the model considers two possible option states $s_i \pm 1$ and a population of N individuals that randomly gather in discussion groups of fixed size G. The basic premise of the model is that all the people within a group adopt the opinion of the majority of the discussion cell. In the case of a tie (which may occur only if the size cell is an even number) a bias is introduced in favor of one of the opinions, say $(+)$, and this opinion prevails in the group. This prescription is inspired in the principle of *social inertia*: people are reluctant to accept a reform if there is no clear majority in its favor.

The main finding of this model is that any initial distribution of voters leads to a collective stable state with a total polarization of the opinion along either one of the two competing states. If $P_+(t) = N_+(t)/N$ is the probability of having the $(+)$ opinion at time t, the final state will be $P_+ = 1$ for initial density $P_+(t = 0) > p_c$ and zero otherwise. In the case of odd size groups this critical density is exactly $p_c = 1/2$. By contrast, groups of even sizes have $p_c \neq 1/2$ as an effect of the tie rule. This implies that even an initially minority opinion can win in the long term.

Krapivsky and Redner [2003] made further analysis of the behavior of the system for odd size groups, for which both possible opinions are symmetrical. They analytically solved the mean-field limit for arbitrary discussion groups of size $G = 3$. They found two stable fixed points at $P_+ = 0, 1$ and an unstable one at $P_+ = 1/2$. Starting from any initial concentration $P_+(t = 0) \neq 1/2$ all agents will converge to the state of the initial majority, recovering Galam's results. It was also obtained that the time needed to reach this consensus grows as $\tau \sim \ln N$. In Ref. [Krapivsky and Redner 2003] the authors also analyzed the model on finite-dimensional lattices. In this case the initial majority also determines the steady state of the system but the consensus time grows as a dimension-dependent power of N. The 1-dimensional model is the only case where the minority can ultimately win, with $\tau \sim N^2$.

Several versions of this model have been recently proposed. A generalization for discussion groups distributed according to a given distribution of gathering sizes has been achieved [Galam 2002; 2003, Tessone et al. 2004], and the same asymptotic behavior with $\tau \sim \ln N$ was observed (here the value of p_c depends of the employed distribution of group sizes).

An interesting modification was also introduced in the model in order to analyze the presence of some agents called *contrarians*- namely, people who are in a "nonconformist opposition". That is, people who always adopt the opposite opinion to the majority [Galam 2004, Stauffer and Martins 2004]. In stock markets for instance, contrarians are those investors who buy shares of the stock when most others are selling, and sell when others are buying. The existence of a high proportion of contrarians in a society may play an important role in social dynamics. With a small fraction a of contrarians and odd sized groups, the unstable separator is still $P_+ = 1/2$, but the system no longer leads to total polarization: starting from any initial concentration $P_+(t = 0) \neq 1/2$, the fully ordered state with a unique opinion becomes mixed with a stable majority-minority splitting. Then, the presence of a small concentration of contrarians preserves the minority opinion in the population. On the other hand, for concentrations of contrarians above some critical fraction a_c the population equally divides between the two possible opinion states. The system exhibits a disordered phase with no opinion dominating ($m = \sum_i s_i/N = 0$).

Further studies of the Galam model in presence of contrarians have extended it to multi-state opinions [Chen and Redner 2005], spatial distribution of meeting cells [Tessone et al. 2004] or even movement of the agents in space [Stauffer 2002].

4.2.4 Bounded-confidence models

In the models considered so far opinion is a binary variable, which represents a reasonable description in several instances. However, there are cases for which the position of an individual can vary smoothly from one extreme to the other of a range of possible choices. Continuous opinion states invalidate some of the concepts adopted in models with binary choices, like the concepts of majority of an opinion or equality of opinions, so they require a different framework. The initial state is usually a population of N agents with randomly assigned opinions, represented by real numbers within some interval. In contrast with binary opinion dynamics, here all the agents usually start with different opinions, and the possible scenarios are more complex, with opinion clusters emerging in the final stationary state. Such opinion clusters can be one (*consensus*), two (*polarization*) or more (*fragmentation*). Discussion only takes place between two agents if their opinions are sufficiently close to each other. This realistic aspect of interaction is called *bounded confidence*. It is usually introduced by employing the tolerance parameter ε such that an agent with opinion x only interact with other agents whose opinion lies in the interval $|x-\varepsilon, x+\varepsilon|$. One of the most popular bounded-confidence models is probably the Deffuant model [Deffuant et al. 2000].

Deffuant model

This model is based on a compromise strategy. After a constructive debate, the positions of the interacting agents get closer to each other by a relative amount μ. The dynamics is defined on a complete graph and based on random binary encounters. Let i and j be the pair of interacting agents at time t, with opinions $x_i(t)$ and $x_j(t)$, respectively (initially chosen at random in the interval [0,1]). If the difference of opinions exceeds the tolerance parameter ε then nothing happens. Otherwise,

$$\begin{aligned} x_i(t+1) &= x_i(t)+\mu[x_j(t)-x_i(t)] \qquad (4.5)\\ x_j(t+1) &= x_j(t)+\mu[x_i(t)-x_j(t)]\,. \qquad (4.6) \end{aligned}$$

The parameter μ is the so-called convergence parameter, and its value lies in the interval $[0, 1/2]$. For any values of the parameters, the average opinion of the interacting pair is the same before and after the interaction, so the global average opinion of the population is an invariant for this dynamics.

The dynamics gives rise to different patches with an increasing density of agents, that will become the final opinion clusters. Once each cluster is sufficiently far from the others, so that the difference of opinion for agents of different clusters exceeds the threshold, only agents inside the same cluster may interact, and the dynamics leads to the convergence of the opinions of all agents in the cluster to the same value. Therefore, the final opinion configuration is a succession of Dirac's delta functions centered around well defined opinions.

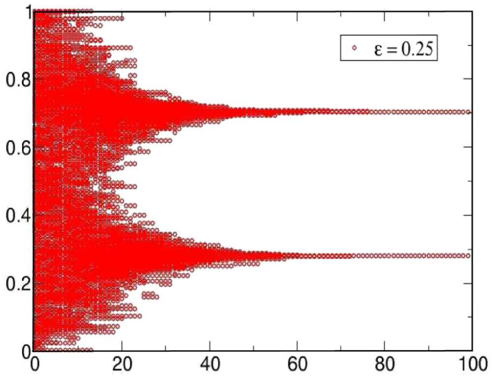

Figure 4.5: Opinion evolution of a population of $N = 500$ agents under Deffuant dynamics for $\varepsilon = 0.25$. The system is considered on a complete graph, *i.e.*, everyone may interact with everybody else. The dynamics leads to a polarization of the population in two factions [Castellano et al. 2007].

CHAPTER

5 The effect of social temperature

In this chapter we deal with Ising-like opinion formation models as some presented in the previous chapter. We include here the effect of a stochastic driving that can be understood as a simplified description of the interplay between an agent, its surroundings, and a collective climate parameter, which is usually referred to as *social temperature* of the system. The chapter is fully devoted to our own original research. In the first part we understand the effect of this social temperature as a tendency of certain individuals to act in the opposite way to the procedural rules of the model. In the second part of the chapter we implement such effect by means of spontaneous changes of opinion that the agents may experience due to the effect of this stochastic driving.

5.1 Emergence of contrarian-like behavior

An important aspect, recently discussed within opinion formation models, has been the presence of some agents called *contrarians*, people that are in a "nonconformist opposition". As we have discussed previously (*cf.* Sec. 4.2.3), such individuals represent people that always adopt the opposite opinion to the majority [Galam 2004, Stauffer and Martins 2004, Schneider 2004]. The existence of a significant proportion of contrarians in a society may play an important role in social dynamics (think for instance of referendums or stock markets dynamics). In an attempt to include the contrarian effect in existing social models, a number of previous studies have considered contrarian agents as an initial condition, either a given fixed density of contrarians is introduced in the model by hand (annealed disorder) [Galam 2004] or a fraction of the population is randomly selected from the start to always behave as a contrarian (quenched disorder) [Stauffer and Martins 2004]. This is somewhat artificial and one would expect that simple models of opinion spreading should spontaneously lead to the existence of a fraction of contrarians among the population as some sort of emergent property. In the following we analyze the emergence of contrarian-like behavior that results from adding a stochastic term to the procedural rules that define the model. As a typical model we employ the Sznajd model introduced in Sec. 4.2.2.

5.1.1 Mean-field approach

Following the previously discussed approach made by Slanina and Lavicka [2003] for the Snajdz-like dynamics, we consider the simplified version in which two agents are chosen randomly and, if they are in consensus, then another randomly chosen agent is convinced by them (called "two over one" case). Up to second order in $1/N$ (with N the total number of agents) the Fokker-Planck equation (FPE) for the probability of having a magnetization m at time t (given a certain initial condition at time $t_0 < t$) results to be

$$\begin{aligned}\frac{\partial}{\partial t}P(m,t) = & -\frac{\partial}{\partial m}\Big[m(1-m^2)P(m,t)\Big] \\ & + \left(\frac{1}{2N}\right)\frac{\partial^2}{\partial m^2}\Big[(1-m^2)P(m,t)\Big] \ , \end{aligned} \tag{5.1}$$

where the magnetization $m = (N^+ - N^-)/N$, and N^+, N^- are the number of agents supporting the $(+)$ or the $(-)$ position, respectively (with $N^+ + N^- = N$).

Now we include the effect of social temperature by considering certain probability p that the rules of the Sznajd model are fulfilled ($p \leq 1$), while there is a probability $1-p$ that those rules are not fulfilled (and then an agent adopts the opposite option than the one indicated by the rules). Following the same procedure that yields Eq. (5.1), we arrive at a FPE for $P_p(m,t)$ (idem for $P(m,t)$, when a probability p is included) that reads

$$\begin{aligned}\frac{\partial}{\partial t}P_p(m,t) = & -\frac{\partial}{\partial m}\Big\{\Big[(6p-5)m-(2p-1)m^3)\Big]P_p(m,t)\Big\} \\ & + \left(\frac{1}{2N}\right)\frac{\partial^2}{\partial m^2}\Big\{\Big[3-2p-(2p-1)m^2\Big]P_p(m,t)\Big\}. \end{aligned} \tag{5.2}$$

The latter FPE has the general form $\frac{\partial P}{\partial t} = -\frac{\partial}{\partial m}[A(m)P(m,t)] + \frac{1}{2}\frac{\partial^2}{\partial m^2}[B(m)P(m,t)]$, and can also be written as a continuity equation $\frac{\partial P(m,t)}{\partial t} + \frac{\partial}{\partial m}J(m,t) = 0$ for the current $J(m,t) = A(m)P(m,t) - \frac{1}{2}\frac{\partial}{\partial m}[B(m)P(m,t)]$. In the case of $\partial P/\partial t = 0$ and $J = 0$ the stationary probability distribution function (PDF) results to be

$$P_p^{stat}(m) \approx \exp\left\{ 2N \int_{-1}^{m} \frac{(6p-5)u(2p-1)u^3}{3-2p-(2p-1)u^2}\, du + \ln\left[\frac{N}{3-2p-(2p-1)m^2}\right] \right\} \quad (5.3)$$

and it can also be expressed in terms of an effective potential as $P_p^{stat}(m) \approx e^{-V_{eff}}$.

The analysis of this stationary solution for varying p shows that there is a threshold value, $p = p_c$, such that for $p > p_c$ the system is *bistable* with a probability density $P_p^{stat}(m)$ having two maxima at $m_\pm = \sqrt{(6p-5)/(2p-1)}$. In this case the system gets ordered by spontaneously selecting one of the stable solutions $m_\pm$. On the contrary, for $p < p_c$ the system becomes *monostable* and disordered with a magnetization density peaked at $m = 0$ in which no dominant opinion survives. The threshold p_c can be calculated in this mean-field approximation equation by equating $m_+ = m_-$, as the value of p at which all three extrema coalesce into single minimum at $m = 0$, so that we find $p_c = 5/6$ (see Fig. 5.1).

For details of calculations carried out in this section we refer the reader to appendix A.

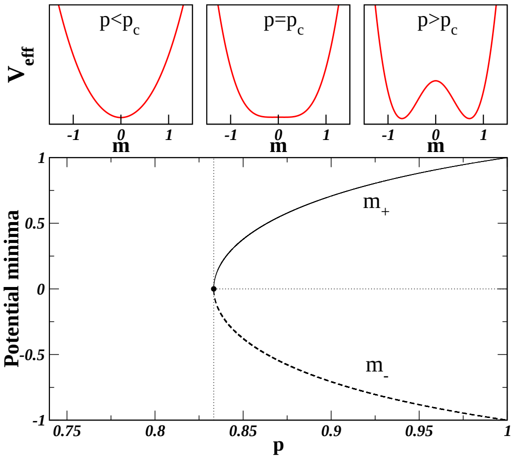

Figure 5.1: The effective potential obtained from Eq. (5.3) shows, for large values of p, two minima $m_\pm$ that become closer to each other for decreasing values of p (second order transition). *Bottom*: Position of the potential minima vs. p. When both extrema coalesce into $m = 0$, the transition point is reached. *Top*: Effective potential for (from left to right) $p = 0.7$, $p = p_c = 5/6$, and $= 0.9$.

The picture emerging from the mean-field approach is clear. The effect of including thermal fluctuations in Sznajd type models immediately leads to a spontaneous contrarian-like effect. Some agents randomly take decisions that oppose the rules of the model, indicating some undecideness in a fraction of the population. If such a fraction overcomes the critical threshold ($\rho_c = 1 - p_c = 1/6$) the system will reach a stalemate situation, analogous to the *contrarians* effect discussed in [Galam 2004, Stauffer and Martins 2004, Schneider 2004]. Furthermore, this critical density of contrarians is in good agreement with the numerical result presented by Galam in [Galam 2004] for groups of size $G = 3$.

5.1.2 Monte-Carlo simulations

In what follows we report on Monte Carlo simulations in order to test the above-discussed mean-filed results. We have studied the model on regular lattices and small-world networks (which in the limit of high rewiring probability should reproduce the mean-field results). To make such an analysis we consider now the more general case in which four spins are updated at each time (version "two against two"). In order to avoid the spurious antiferromagnetic solution of the original Sznajd model, we have studied a convenient variation proposed by Sánchez [2004] and previously introduced in Sec. 4.2.2:

Rule 1: if $s_i \times s_{i+1} = 1$, then s_{i-1} and s_{i+2} adopt the direction of the selected pair $[i, i+1]$.

Rule 2:: if $s_i \times s_{i+1} = -1$, then s_i adopts the direction of s_{i-1} and s_{i+1} the direction of s_{i+2}.

In the case of disagreement of the pair (s_i, s_{i+1}), the second rule makes the agent i to feel "more comfortable" since it ends up with at least one neighbor having its same opinion. This variation of the Sznajd model does not affect the basic behavior and indeed has been shown to exhibit the same type of scaling features as the original model [Sánchez 2004], while lacking the spurious antiferromagnetic phase.

As indicated above, we introduce a stochastic mechanism in the dynamics in order to consider the effect of certain *social temperature*. At each Monte Carlo step we assume that, with a probability p, the rules are applied as indicated above, while the opposite happens with a probability $1 - p$. We define the probability p in analogy with previous works of Weidlich [Weidlich 2002; 1991] and Babinec [Babinec 1997, Kuperman and Zanette 2002],

$$p = \Lambda \exp\left[\frac{\alpha}{\theta}\right], \tag{5.4}$$

where α is some fixed parameter related with the strength of nearest-neighbor interactions, which just defines the units in which temperature is measured (we use natural units in what follows, $\alpha = 1$), and θ is the collective climate parameter (*social temperature*). Λ is just a normalization parameter ($\Lambda^{-1} = \exp[(\alpha)/\theta] + \exp[-(\alpha)/\theta]$).

The asymptotic behavior of p is

- if $\theta \rightarrow 0$, we have $p \rightarrow 1$, indicating that without thermal fluctuations we recover the original dynamics;
- if $\theta \rightarrow \infty$, we have $p \rightarrow 0.5$, the probability of fulfilling the rules or the opposite is the same. The model has a totally random behavior.

a) One-dimensional lattice results

Firstly we report on our results on the one-dimensional lattice, where each lattice site is occupied by one agent with opinion (spin) $s_i \in \{+1, -1\}$. We started with a randomly distributed opinion of the N agents and let the system evolve toward its stationary state. For $\theta = 0$ a consensus state arises ($m_{\pm} = \pm 1$). However, as θ is increased we observe a phase transition towards the *stalemate* state. Nonetheless, in a different way that in the mean-field case, this transition is discontinuous (first order) as shown in Fig. 5.2.

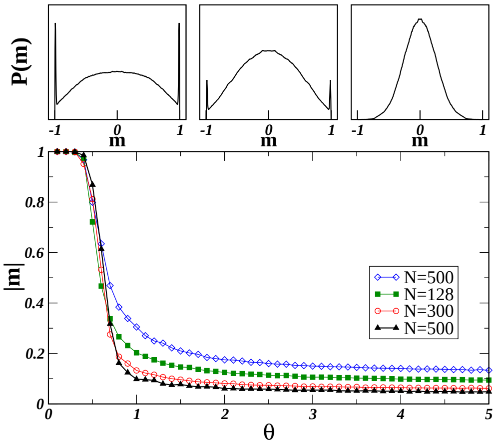

Figure 5.2: Discontinuous phase transition for one-dimensional regular lattice: the jump of the order parameter *m* from ±1 to zero occurs abruptly. That discontinuity is clearer the larger N is. *Top*: Stationary PDF for $\theta = 0.44, 0.46, 0.6$ (from left to right), and $N = 512$. For small values of θ a relative maximum appears at m=0 and dominates for $\theta > \theta^{*}$, as corresponds to a first order transition

b) Fully-connected network results

In order to compare with the mean-field results, we have studied our model in a fully connected network, which is expected to behave as the mean-field theory. Indeed, in these conditions we observe that the transition between order and stalemate states becomes continuous. The qualitative agreement with the previously discussed theoretical result is apparent (see Fig. 5.3). The critical density of contrarians needed to reach the phase transition can be approached as $\rho_c(\theta^*) \sim 1 - p(\theta^*)$. In the large system size limit this value tends to $\rho_c(\theta^*) \to 1/3$, as is shown in Fig. 5.4.

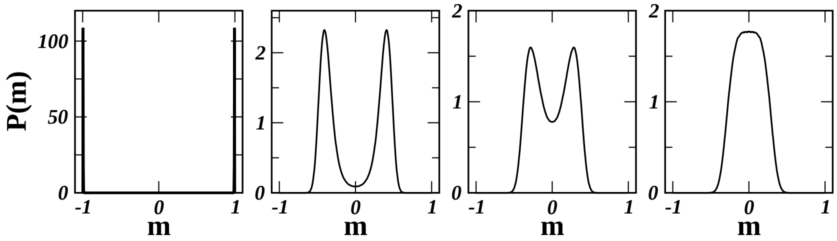

Figure 5.3: Stationary PDF for a fully-connected lattice of $N = 512$. From left to right $\theta = 0.30$, 2.30, 2.60, and 2.90. A second order transition toward a "stalemate" state is apparent: the most probable values of the order parameter *m* change continuously from $m = \pm 1$ (*bistable*) to $m = 0$ (*monostable*).

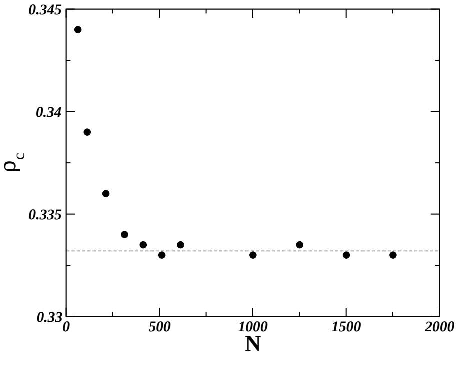

Figure 5.4: Critical density of contrarians ρ_c versus system size N for a fully connected network. In the large system size limit this value tends to $\rho_c(\theta^*) \to 1/3$.

c) Small-world network results

In order to find the intermediate behavior between one-dimensional and the *mean-field-like* approach, we have applied the rules of the model on a *small-world* network. Such networks are characterized by Poissonian distributions of the number of links and short distances between nodes. To generate them we employ the Watts-Strogatz algorithm [Watts and Strogatz 1998], departing from a regular lattice with connections up to n neighbors and then redirecting the links with probability r. For further reading on small-world networks see Sec. 6.4. We observed that even for small values of r the system undergoes a continuous phase transition from order to disorder as predicted by mean-field theory [*c.f.* Fig. 5.5]. We also observed that for increasing values of the rewiring probability r, the critical temperature θ^* separating the ordered and disordered phases also increases, as shown in Fig. 5.6.

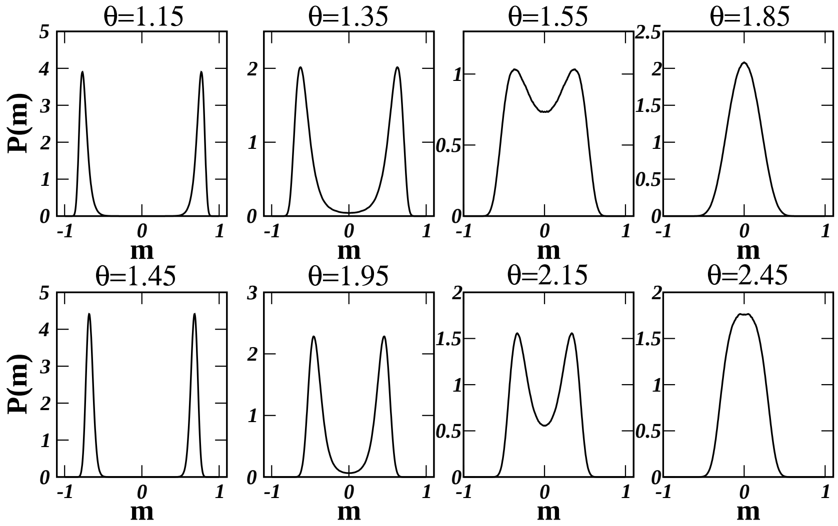

Figure 5.5: Stationary PDF for a small-world lattice of $N = 512$ obtained from a regular lattice with connections up to $n = 5$ neighbors that are redirected with probability $r = 0.1$ (top) and $r = 0.8$ (bottom). A second order transition towards a "stalemate" state is observed even in case of low rewiring probability.

Summarizing, we observe a contrarian-like effect analogous to the one described in [Galam 2004]. If social temperature is above a critical threshold, the density of contrarians is high enough to avoid the consensus, and the opinion is equally distributed between the two options leading to a zero global magnetization state with no opinion dominance. In some cases the critical density of contrarians needed to force the stalemate state, $\rho_c = 1 - p(\theta^*)$, may be quite large (we observed $\rho_c \approx 1/3$

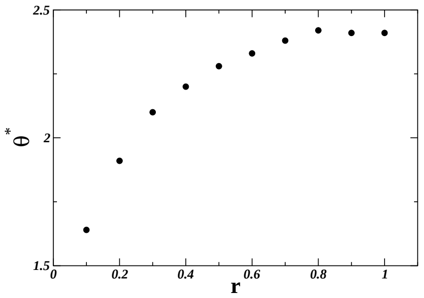

Figure 5.6: θ^*, the critical temperature for the phase transition, vs. r, the probability of link redirection. It is apparent that for increasing values of r (larger small-world effect the lattice has), θ^* increases monotonously. In all cases $N = 512$.

for the "two against two" model on fully-connected networks). However, even such large concentrations of contrarians could be considered in realistic systems, as the agents adopt this role dynamically. We do not have to assume the presence of a large fixed group of "nonconformist agents", as is done when they are introduced by hand [Galam 2004, Stauffer and Martins 2004].

5.2 Spontaneous change of opinion. Van Kampen's approach

In this section we try to implement the thermal effect by means of agents that can suffer spontaneous changes of opinion. We work on a simple opinion formation model, analogous to the one studied in [Vazquez et al. 2003, Vazquez and Redner 2004]. The system consists of two parties, A and B, and an "intermediate" group I, that we call *undecided agents*. We consider that members of groups A and B have well established positions about a given subject (*e.g.* European constitution) and I constitutes a group of undecided agents that could possibly be converted to one of the dominant positions. We assume that the supporters of parties A and B do not interact directly, but only through their interaction with group I. However, we do not consider that members of I can convince those of A or B, mainly because they do not have a definite opinion, but instead we assume that there is a nonzero probability of a spontaneous change of opinion from I to the other two parties and viceversa $I \leftrightarrows A$ and $I \leftrightarrows B$. We will see that this probability of spontaneous change of opinion (implying the existence of a *social temperature*) prevents the system from reaching a consensus. Instead of consensus, we find that each party has some statistical density of supporters, and there is also a statistical stationary number of undecided (I) agents.

Our aim is to write a master equation for this toy model, and study its behavior via a van Kampen's Ω-expansion approach [van Kampen 1981]. After determining if, in this case, the conditions for the validity of using such an approach are fulfilled, we will obtain the *macroscopic* evolution equations for the density of supporters of A and B parties, as well as the Fokker-Planck equation governing the fluctuations around such deterministic or macroscopic behavior. The same approach also gives information about the typical relaxation behavior of small perturbations around the stationary macroscopic solutions.

5.2.1 The model and the approach

Description of the model

We consider a system composed by three different groups of agents, namely N_A and N_B for the number of supporters of the A and B parties, respectively, and a group of undecided, indicated by N_I. We have the constraint $N_A + N_B + N_I = N$, where N is the total number of agents. Such a constraint implies that, for fixed N, there are only two independent variables N_A and N_B. As mentioned above, the interactions we are going to consider are only between A and I, and B and I. That means that we do not consider direct interactions among A and B. The different contributions that we include are

- spontaneous transitions $A \to I$, occurring with a rate $\alpha_1 \, N_A$;
- spontaneous transitions $I \to A$, occurring with a rate $\alpha_2 \, N_I$;
- spontaneous transitions $B \to I$, occurring with a rate $\alpha_3 \, N_B$;
- spontaneous transitions $I \to B$, occurring with a rate $\alpha_4 \, N_I$;
- convincing rule $A + I \to 2\,A$, occurring with rate $\frac{\beta_1}{N} N_A N_I$;
- convincing rule $B + I \to 2\,B$, occurring with rate $\frac{\beta_2}{N} N_B N_I$.

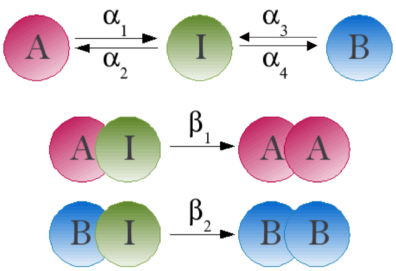

Figure 5.7: All possible interactions among the three different groups of agents, namely A, B, and undecided ones, I. Spontaneous transitions occur at rate α_i, for which $i = 1, 2, 3, 4$ (top). Convincing process occur at rate β_i, $i = 1, 2$ (bottom).

With the above indicated interactions and rates, the master equation for the probability $P(N_A, N_B, t)$ of having populations N_A and N_B at time t (given that we had populations N_A^o and N_B^o at an initial time $t_o < t$), may be written as

$$\begin{aligned}\frac{\partial}{\partial t}P(N_A,N_B,t) = \alpha_1(N_A+1)P(N_A+1,N_B,t)+ \\ &+\alpha_3(N_B+1)P(N_A,N_B+1,t)+ \\ &+\alpha_2(N-N_A-N_B+1)P(N_A-1,N_B,t)+ \\ &+\alpha_4(N-N_A-N_B+1)P(N_A,N_B-1,t)+ \\ &+\frac{\beta_1}{N}(N_A-1)(N-N_A-N_B+1)P(N_A-1,N_B,t)+ \\ &+\frac{\beta_2}{N}(N_B-1)(N-N_A-N_B+1)P(N_A,N_B-1,t)- \\ &-\Big[\alpha_1 N_A+\alpha_3 N_B+(\alpha_2+\alpha_4)(N-N_A-N_B)+ \\ &+\Big(\frac{\beta_1 N_A+\beta_2 N_B}{N}\Big)(N-N_A-N_B)\Big]P(N_A,N_B,t). \qquad (5.5)\end{aligned}$$

This is the model master equation to which we will apply van Kampen's approach [van Kampen 1981].

Van Kampen's expansion

In order to apply van Kampen's approach, as discussed in [van Kampen 1981], we identify the large parameter Ω with N (assuming $N \gg 1$); and define the following separation of the N_i's into a macroscopic part of size N, and a fluctuational part of size $N^{\frac{1}{2}}$:

$$\begin{aligned} N_A &= N\Psi_A(t) + N^{\frac{1}{2}}\xi_A(t), \\ N_B &= N\Psi_B(t) + N^{\frac{1}{2}}\xi_B(t), \end{aligned} \tag{5.6}$$

where $\Psi_{A(B)}$ is the density of supporters of party $A(B)$ and $\xi_{A(B)}$ represents fluctuations around the macroscopic solution. A "reference" density $\rho = \frac{N}{\Omega}$ is defined, that in our case is simply $\rho = 1$. We also define the "step operators"

$$\begin{aligned} \mathbb{E}_i^+ f(N_i) &= f(N_i + 1), \\ \mathbb{E}_i^- f(N_i) &= f(N_i - 1), \end{aligned}$$

with $f(N_i)$ an arbitrary function. Using the forms indicated in Eqs. (5.6), in the limit of $N \gg 1$, the step operators adopt the differential form [van Kampen 1981]

$$\mathbb{E}_i^{\pm} = 1 \pm \left(\frac{1}{N}\right)^{\frac{1}{2}} \frac{\partial}{\partial \xi_i} + \frac{1}{2}\left(\frac{1}{N}\right) \frac{\partial^2}{\partial \xi_i^2} \pm \ldots, \tag{5.7}$$

with $i = A, B$. Transforming from the original variables (N_A, N_B) to the new ones (ξ_A, ξ_B), we have the relations

$$P(N_A, N_B, t) \rightarrow \Pi(\xi_A, \xi_B, t)\ , \tag{5.8}$$

$$N^{\frac{1}{2}} \frac{\partial}{\partial N_i} P(N_A, N_B, t) = \frac{\partial}{\partial \xi_i} \Pi(\xi_A, \xi_B, t)\ , \tag{5.9}$$

$$\frac{\partial}{\partial t} P(N_A, N_B, t) = \frac{\partial}{\partial t} \Pi(\xi_A, \xi_B, t) - N^{\frac{1}{2}} \frac{d\Psi_A}{dt} \frac{\partial \Pi}{\partial \xi_A} - N^{\frac{1}{2}} \frac{d\Psi_B}{dt} \frac{\partial \Pi}{\partial \xi_B}\ . \tag{5.10}$$

Putting everything together, we can rewrite the master equation Eq. (5.5) in terms of the new variables. We are now in a position to collect the different powers of N.

Considering contributions up to order $N^{1/2}$, yields the following two coupled differential equations for the macroscopic behavior

$$\frac{d}{dt}\Psi_A(t) = -\alpha_1 \Psi_A + \Big[\alpha_2 + \beta_1 \Psi_A\Big]\Big(\rho - \Psi_A - \Psi_B\Big), \tag{5.11}$$

$$\frac{d}{dt}\Psi_B(t) = -\alpha_3 \Psi_B + \Big[\alpha_4 + \beta_2 \Psi_B\Big]\Big(\rho - \Psi_A - \Psi_B\Big). \tag{5.12}$$

It can be proved that the last set of equations has a unique (physically sound) stationary solution $\left(\frac{d\Psi_A(t)}{dt} = \frac{d\Psi_B(t)}{dt} = 0\right)$, *i.e.* a unique attractor

$$\begin{aligned} \Psi_A(t \rightarrow \infty) &= \Psi_A^{st} \\ \Psi_B(t \rightarrow \infty) &= \Psi_B^{st}. \end{aligned}$$

This is the main condition to validate the application of van Kampen's Ω-expansion approach [van Kampen 1981]. To prove this we analyze the linear stability of the solution when a small perturbation $\Psi_{st} + \delta\Psi$ is considered. Fluctuations around the stationary solution are supposed to evolve exponentially with time $\delta_i \approx e^{\lambda_i t}$, $i = A, B$ and we can prove that for any value of the parameters the exponents λ_A,λ_B result to be negative. Up to this point, we have discussed the $N^{1/2}$ order.

The following order, that is N^0, yields the Fokker-Planck equation governing the fluctuations around the macroscopic behavior. It is given by

$$\begin{aligned}
\frac{\partial}{\partial t}\Pi(\xi_A,\xi_B,t) = {} & \frac{\partial}{\partial \xi_A}\Big[(\alpha_1\xi_A + (\alpha_2+\beta_1\Psi_A)(\xi_A+\xi_B) - \beta_1\xi_A(\rho-\Psi_A-\Psi_B))\,\Pi(\xi_A,\xi_B,t)\Big] \\
& + \frac{\partial}{\partial \xi_B}\Big[(\alpha_3\xi_B + (\alpha_4+\beta_2\Psi_B)(\xi_A+\xi_B) - \beta_2\xi_B(\rho-\Psi_A-\Psi_B))\,\Pi(\xi_A,\xi_B,t)\Big] \\
& + \frac{1}{2}\Big[\alpha_1\Psi_A + (\alpha_2+\beta_1\Psi_A)(\rho-\Psi_A-\Psi_B)\Big]\frac{\partial^2}{\partial \xi_A^2}\Pi(\xi_A,\xi_B,t) \\
& + \frac{1}{2}\Big[\alpha_3\Psi_B + (\alpha_4+\beta_2\Psi_B)(\rho-\Psi_A-\Psi_B)\Big]\frac{\partial^2}{\partial \xi_B^2}\Pi(\xi_A,\xi_B,t). \qquad (5.13)
\end{aligned}$$

This is a two-dimensional linear FPE, with a general form

$$\frac{\partial P(x,y,t)}{\partial t} = \frac{\partial}{\partial x}[(A_0 + A_1x + A_2y)P] + \frac{\partial}{\partial y}[(B_0 + B_1y + B_2x)P] + \frac{1}{2}C_0\frac{\partial^2 P}{\partial x^2} + \frac{1}{2}D_0\frac{\partial^2 P}{\partial y^2}\ ,$$

which describes a Ornstein-Uhlenbeck process. It is well known that the solution of this FPE is a Gaussian determined by the first and second moments of the fluctuations [van Kampen 1981]. Hence, in the next section we analyze the equations governing those quantities.

5.2.2 Behavior of fluctuations

From the FPE in Eq. (5.13), it is possible to obtain equations for the mean value of the fluctuations as well as for the correlations of those fluctuations. For the fluctuations, $\langle\xi_A(t)\rangle = \eta_A$ and $\langle\xi_B(t)\rangle = \eta_B$, we have

$$\begin{aligned}
\frac{d}{dt}\eta_A(t) &= \int\!\!\int \xi_A\frac{\partial\Pi}{\partial t}\,d\xi_A\,d\xi_B = \\
&= -\Big[\alpha_1 + \alpha_2 + \beta_1(2\Psi_A + \Psi_B) - \beta_1\rho\Big]\eta_A - (\alpha_2 + \beta_1\Psi_A)\eta_B\ , \qquad (5.14) \\
\frac{d}{dt}\eta_B(t) &= \int\!\!\int \xi_B\frac{\partial\Pi}{\partial t}\,d\xi_A\,d\xi_B = \\
& - \Big[\alpha_3 + \alpha_4 + \beta_2(\Psi_A + 2\Psi_B) - \beta_2\rho\Big]\eta_B - (\alpha_4 + \beta_2\Psi_B)\eta_A. \qquad (5.15)
\end{aligned}$$

Calling $\sigma_A = \langle \xi_A(t)^2 \rangle$, $\sigma_B = \langle \xi_B(t)^2 \rangle$, and $\sigma_{AB} = \langle \xi_A(t)\xi_B(t) \rangle$, we also obtain for the correlation of fluctuations

$$\begin{aligned}
\frac{d}{dt}\sigma_A(t) &= -2\alpha_1\sigma_A - 2[\alpha_2 + \beta_1\Psi_A][\sigma_A + \sigma_{AB}] + 2\beta_1\sigma_A[\rho - \Psi_A - \Psi_B] \\
&\qquad + [\alpha_1\Psi_A + (\alpha_2 + \beta_1\Psi_A)(\rho - \Psi_A - \Psi_B)] \,, \qquad (5.16) \\
\frac{d}{dt}\sigma_B(t) &= -2\alpha_3\sigma_B - 2[\alpha_4 + \beta_2\Psi_B][\sigma_{AB} + \sigma_B] + 2\beta_2\sigma_B[\rho - \Psi_A - \Psi_B] \\
&\qquad + [\alpha_3\Psi_B + (\alpha_4 + \beta_2\Psi_B)(\rho - \Psi_A - \Psi_B)] \,, \qquad (5.17) \\
\frac{d}{dt}\sigma_{AB}(t) &= -[\alpha_1 + \alpha_3]\sigma_{AB} - [\alpha_2 + \beta_1\Psi_A][\sigma_{AB} + \sigma_B] \\
&\qquad - [\alpha_4 + \beta_2\Psi_B][\sigma_A + \sigma_{AB}] + [\rho - \Psi_A - \Psi_B][\beta_1 + \beta_2]\sigma_{AB} \,. \qquad (5.18)
\end{aligned}$$

a) Reference state: symmetric case

Here we particularize the obtained equations for the symmetric case, *i.e.*, the case when $\Psi_A^{st} = \Psi_B^{st}$. Hence, we adopt

$$\alpha_1 = \alpha_3 = \alpha, \quad \alpha_2 = \alpha_4 = \alpha',$$

and

$$\beta_1 = \beta_2 = \beta.$$

In such a case, the macroscopic equations (5.11) and (5.12) take the form

$$\frac{d}{dt}\Psi_A(t) = -[\alpha + \alpha' - \beta]\Psi_A - \beta\Psi_A^2 - \beta\Psi_A\Psi_B - \alpha'\Psi_B + \alpha' \qquad (5.19)$$

$$\frac{d}{dt}\Psi_B(t) = -[\alpha + \alpha' - \beta]\Psi_B - \beta\Psi_B^2 - \beta\Psi_A\Psi_B - \alpha'\Psi_A + \alpha'. \qquad (5.20)$$

In order to make the solution of these equations more explicit, we work with the auxiliary variables $\Sigma = \Psi_A + \Psi_B$ and $\Delta = \Psi_A - \Psi_B$, and use $\rho = 1$. The last equations now transform into

$$\frac{d}{dt}\Sigma(t) = -\Big[\alpha + 2\alpha' - \beta\Big]\,\Sigma - \beta\Sigma^2 + 2\alpha' \qquad (5.21)$$

$$\frac{d}{dt}\Delta(t) = -\Big[\alpha - \beta\Big]\,\Delta - \beta\Delta\Sigma. \qquad (5.22)$$

In the long time limit, $t \to \infty$, we found on one hand

$$\Delta^{st} = 0,$$

implying $\Psi_A^{st} = \Psi_B^{st}$, while on the other hand

$$0 = \beta\,\Sigma^2 + \Big[\alpha + 2\alpha' - \beta\Big]\,\Sigma - 2\alpha'.$$

This polynomial has two roots, but only one is physically sound, namely

$$\Sigma^{st} = \frac{\alpha + 2\alpha' - \beta}{2\beta}\left(-1 + \sqrt{1 + \frac{8\alpha'\beta}{[\alpha + 2\alpha' - \beta]^2}}\right), \tag{5.23}$$

yielding $\Psi_A^{st} = \Psi_B^{st} = \Psi_o^{st} = \frac{1}{2}\Sigma^{st}$.

In a similar way, we can also simplify the equations (5.14) and (5.15) for η_A and η_B, calling $S(t) = \eta_A + \eta_B$ and $D(t) = \eta_A - \eta_B$. The corresponding equations are then rewritten as

$$\begin{aligned} \frac{d}{dt}S(t) &= -\Big[\alpha + 2\alpha' + 2\beta(\Psi_A + \Psi_B) - \beta\Big]\,S, && (5.24)\\ \frac{d}{dt}D(t) &= -\Big[\alpha + \beta(\Psi_A + \Psi_B) - \beta\Big]D - \beta\Big[\Psi_a - \Psi_B\Big]S, && (5.25) \end{aligned}$$

while for the correlation of the fluctuations we have

$$\begin{aligned} \frac{d}{dt}\sigma_A(t) &= -2\alpha\sigma_A - 2[\alpha' + \beta\Psi_A][\sigma_A + \sigma_{AB}] + 2\beta[1 - \Psi_A - \Psi_B]\sigma_A \\ &\quad + \big[\alpha\Psi_A + (\alpha' + \beta\Psi_A)(1 - \Psi_A - \Psi_B)\big], && (5.26)\\ \frac{d}{dt}\sigma_B(t) &= -2\alpha\sigma_B - 2[\alpha' + \beta\Psi_B][\sigma_{AB} + \sigma_B] + 2\beta[1 - \Psi_A - \Psi_B]\sigma_B \\ &\quad + \big[\alpha\Psi_B + (\alpha' + \beta\Psi_B)(1 - \Psi_A - \Psi_B)\big], && (5.27)\\ \frac{d}{dt}\sigma_{AB}(t) &= -2\alpha\sigma_{AB} - [\alpha' + \beta\Psi_A][\sigma_{AB} + \sigma_B] \\ &\quad -[\alpha' + \beta\Psi_B][\sigma_{AB} + \sigma_A] + 2\beta[1 - \Psi_A - \Psi_B]\sigma_{AB}. && (5.28) \end{aligned}$$

Equations (5.24) and (5.25) show that, in the asymptotic limit $t \to \infty$, both $S = 0$ and $D = 0$, implying that $\eta_A^{st} = \eta_B^{st} = 0$. However, also in the general (non symmetric) case we expect to find $\eta_A^{st} = \eta_B^{st} = 0$. In addition, from Eqs. (5.26), (5.27) and (5.28), it is clear that we obtain $\sigma_i^{st} \neq 0$ ($i = A, B, AB$) for $t \to \infty$.

b) Beyond the symmetric case

Let us call α_o, α'_o and β_o the parameter's values corresponding to the symmetric case. We consider now the following cases, where we vary the parameters

$$\beta_1 = \beta_o, \quad \beta_2 = \beta_o + \Delta\beta,$$

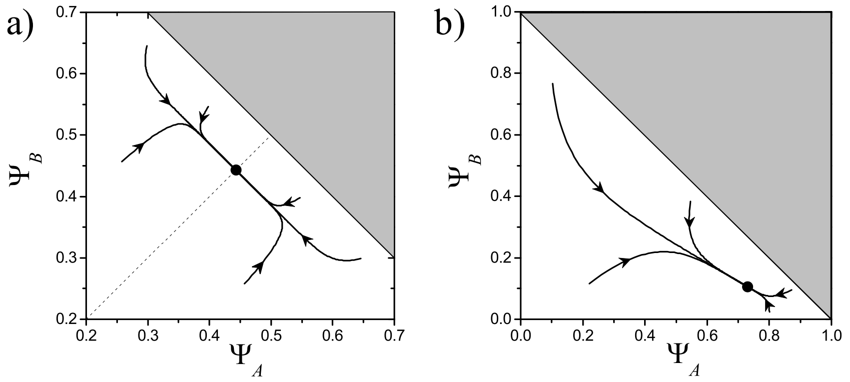

Figure 5.8: Evolution of the macroscopic solutions [Eqs.(5.11) and (5.12)]. Case (a) corresponds to trajectories toward a symmetric solution (*i.e.* with $\Psi_A^{st} = \Psi_B^{st}$), with parameters $\alpha_1 = \alpha_3 = 1$, $\alpha_2 = \alpha_4 = 3$, and $\beta_1 = \beta_2 = 2$. Case (b) corresponds to trajectories toward an asymmetric solution (*i.e.* with $\Psi_A^{st} \neq \Psi_B^{st}$), with parameters $\alpha_1 = 1$, $\alpha_3 = 5$, $\alpha_2 = \alpha_4 = 3$, and $\beta_1 = \beta_2 = 2$.

$$\alpha_1 = \alpha_o, \quad \alpha_3 = \alpha_o + \Delta\alpha,$$
$$\alpha_2 = \alpha_o', \quad \alpha_4 = \alpha_o' + \Delta\alpha'.$$

We will vary only one of these parameters, while keeping the rest fixed. In the following section we present the results (mainly numerical) corresponding to these different cases.

5.2.3 Numerical Results

As indicated above, the macroscopic equations (Eqs. (5.11) and (5.12)) have a unique attractor, indicating that it is adequate to apply van Kampen's expansion approach. In this section we will present some results corresponding to symmetric and asymmetric situations, which show some typical behavior to be expected from the model and the approximation method. In what follows, all parameters are measured in arbitrary units.

In Fig. 5.8 we show the evolution of $\Psi_A(t)$ and $\Psi_B(t)$, the macroscopic solutions, indicating some trajectories toward the attractor: (a) for a symmetric, and (b) an asymmetric case. It is worth recalling that Ψ_A and Ψ_B are the density of supporters of party A and party B, respectively. During the evolution toward the attractor, starting from arbitrary initial conditions, we observe the possibility of a marked initial increase of the macroscopic density for one of the parties, followed by a marked

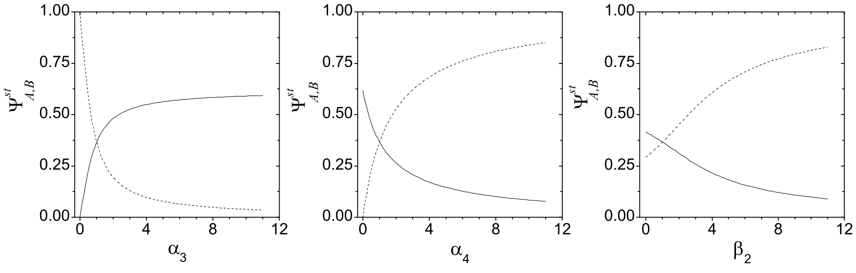

Figure 5.9: Dependence of the stationary macroscopic solutions on different system parameters: (a) On α_3, the rest of parameters are $\alpha_1 = \alpha_2 = \alpha_4 = 1$, and $\beta_1 = \beta_2 = 1$. (b) On α_4, the rest of parameters are $\alpha_1 = \alpha_2 = \alpha_3 = 1$, and $\beta_1 = \beta_2 = 1$. (c) On β_2, the rest of parameters are $\alpha_1 = \alpha_2 = \alpha_3 = \alpha_4 = 1$, and $\beta_1 = 1$. In all three cases, the continuous line corresponds to Ψ^{st}_A while Ψ^{st}_B is indicated by the dotted line.

reduction, or other situations showing only a decrease of an initial high density. Such cases may indicate that one should be careful when evaluating the results of surveys and polls during, say, an electoral process. It is possible that an impressive initial increase in the support of a party can be followed by an equally impressive decay of support. We remark that in both panels of Fig 5.8 the sum of Ψ_A and Ψ_B is always $\Psi_A + \Psi_B < 1$, so implying that there is always a finite fraction of undecided agents.

On the other hand, we analyze the dependence of the stationary macroscopic solutions on the system parameters. In Fig. 5.9 we depict how Ψ^{st}_B and Ψ^{st}_A vary with α_3, α_4, and β_2. Due to the symmetry of the problem, varying the set of parameters $(\alpha_3, \alpha_4, \beta_2)$ is equivalent to varying the set $(\alpha_1, \alpha_2, \beta_1)$. In Fig. 5.9(a) the dependence on α_3 is represented. It is apparent that for $\alpha_3 < \alpha_1$, we have $\Psi^{st}_B < \Psi^{st}_A$, while for $\alpha_3 > \alpha_1$, we find the inverse situation. Clearly, $\Psi^{st}_B = \Psi^{st}_A$ when $\alpha_3 = 1 (= \alpha_1)$, as it corresponds to the symmetric case. Similarly, in Figs. 5.9(b) and 5.9(c) we see the dependence of the stationary macroscopic solutions on the parameters α_4 and β_2, respectively. Also in these cases we observe similar behavior as in the previous one, when varying the indicated parameters. The parameters α_3 or α_4 (and similarly for α_1 or α_2) correspond to spontaneous changes of opinion, and may be related to the presence of a *social temperature*. However, also β_1 and β_2, which correspond to convincing capacities, are affected by such a temperature. So, the variation of these parameters in Fig. 5.9 corresponds to changes in the social temperature, changes that

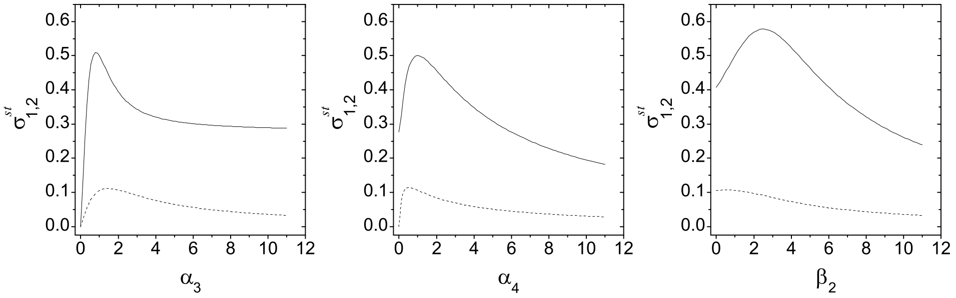

Figure 5.10: Dependence of the stationary correlation functions σ_i (with $i = 1, 2$) corresponding to the projection of $\sigma_{A,B,AB}$ on the principal axes, on different parameters of the system: (a) on α_3, the other parameters are $\alpha_1 = \alpha_2 = \alpha_3 = 1$, and $\beta_1 = \beta_2 = 1$. (b) on α_4, the other parameters are $\alpha_1 = \alpha_2 = \alpha_3 = 1$, and $\beta_1 = \beta_2 = 1$. (b) on β_2, the other parameters are $\alpha_1 = \alpha_2 = \alpha_3 = \alpha_4 = 1$, and $\beta_1 = 1$.

could be attributed, in a period of time preceding an election, to an increase in the level of discussions as well as to the amount of propaganda.

We can also analyze numerically the behavior of fluctuations. As was previously pointed out for a general non symmetrical case we have $\eta_A^{st} = \eta_B^{st} = 0$. However, we can analyze the behavior of the stationary correlation of such fluctuations. In Fig. 5.10 we depict the dependence of the stationary correlation functions for the fluctuations σ_i (with $i = 1, 2$, corresponding to the projection of $\sigma_{A,B,AB}$ on the principal axes) on different systems' parameters. In Fig. 5.10(a) the dependence on α_3 is represented, and similarly in Figs. 5.10(b) and 5.10(c), the dependence on the parameters α_4 and β_2, respectively. We observe that, as the parameters are varied (that, in the case of α_3 and α_4, and as indicated above, could be associated with a variation of the social temperature) a *tendency inversion* could arise. This indicates that the dispersion of the probability distribution could change with a variation of the social temperature.

We can also depict the stationary (Gaussian) probability distribution:

$$\Pi(\xi_A, \xi_B)^{st} \sim \exp\left\{ \begin{pmatrix} \xi_A & \xi_B \end{pmatrix} \begin{pmatrix} \sigma_A & \sigma_{AB} \\ \sigma_{AB} & \sigma_B \end{pmatrix}^{-1} \begin{pmatrix} \xi_A \\ \xi_B \end{pmatrix} \right\}. \tag{5.29}$$

Figure 5.11 shows Π projected on the original (N_A, N_B) plane where, following Eq. (5.6), $\xi_i = \frac{N_i}{N}\sqrt{N} - \sqrt{N}\Psi_i, i = A, B$.

We show three cases: on the left a symmetrical case, the central panel corresponds to an asymmetrical situation with a population of $N = 100$, and on the right

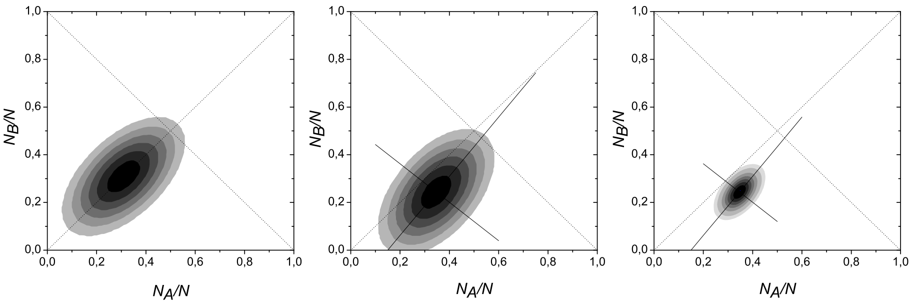

Figure 5.11: Stationary, Gaussian, probability distribution $\Pi(\xi_A, \xi_B)^{st}$ projected on the original (N_A, N_B) plane. On the let we have a symmetrical case with $\alpha_1 = \alpha_3 = 2$, $\alpha_2 = \alpha_4 = 1$, $\beta_1 = \beta_2 = 2$, and the population is $N = 100$. The central plot shows an asymmetrical case, with $\alpha_1 = 2$ and $\alpha_3 = 2.5$, while $\alpha_2 = \alpha_4 = 1$, $\beta_1 = \beta_2 = 2$, and the population is $N = 100$. On the right we have the same asymmetrical case as before, but now $N = 1000$, showing the dispersion's reduction of the Gaussian distribution.

the same asymmetrical situation but with $N = 1000$. The latter clearly shows the influence of the population number in reducing the dispersion (as the population increases). We can use this PDF to estimate the probability p_i $(i = A, B)$ of winning for one or the other party. This corresponds to the volume of the distribution remaining above, or below, the bisectrix $N_A/N = N_B/N$. In the symmetrical case, obviously, we obtain $p_A = p_B = 0.5$ (or 50%), while in the asymmetrical case we find $p_B = 0.257$ (or 25.7%) and $p_B = 0.015$ (or 1.5%) for $N = 100$ and $N = 1000$, respectively. These results indicate that, for an asymmetrical situation, we have a non zero probability that the minority party could, due to a fluctuation during the voting day, win a close election. However, in agreement with intuition, as far as $N \gg 1$ and the stationary macroscopic solution departs from the symmetric case, such a probability p_i reduces proportionally to N^{-1}[1].

By analyzing the evolution in time of the macroscopic solution and the correlations of the fluctuations we can get an idea of how this Gaussian probability behaves in time. In Fig. 5.12, on the left, we show a typical result for the time evolution of the macroscopic solution toward an asymmetric stationary case. In the same figure, in the central part, we find the associated time evolution of the correlation functions

---

[1] It is worth commenting that it is convenient to avoid pathological ranges of parameters that make $\Upsilon = \Psi_A^{st} + \Psi_B^{st}$ to fall within a very thin strip near the frontiers of the physical region (*i.e.* the region limited by $\Upsilon = 1$, $\Psi_A^{st} = 0$, and $\Psi_B^{st} = 0$). In such cases, the tail of fluctuations falling outside the physical region will be too large invalidating the whole approach. Clearly, the parameters chosen for Fig. 5.11 avoid such pathological situation, as the fluctuation tails falling outside the physical region are negligible.

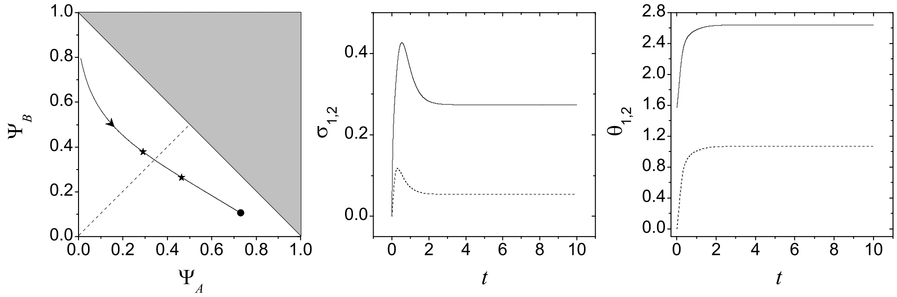

Figure 5.12: On the left, we have the time evolution of the macroscopic solutions $\Psi_A(t)$ and $\Psi_B(t)$. The parameter values are $\alpha_1 = 1$, $\alpha_3 = 5$, $\alpha_2 = \alpha_4 = 3$, $\beta_1 = \beta_2 = 2$. The stars indicate the position where σ_1 and σ_2 attain their maximum, as seen in the central panel. Central part, time evolution of the correlation functions σ_i (with $i = 1, 2$) corresponding to the projection of $\sigma_{A,B,AB}$ on the principal axes. On the right, the angle between the principal axes and the figure axes. The parameters are $\alpha_1 = 1$, $\alpha_3 = 5$, $\alpha_2 = \alpha_4 = 3$, and $\beta_1 = \beta_2 = 2$.

for the fluctuations σ_i (with $i = 1, 2$) corresponding to the projection of $\sigma_{A,B,AB}$ on the principal axes, while on the right we show the evolution of the angle between the principal axes and the figure axes. The temporal reentrance effect that has been observed in other studies based on the van Kampen's approach [van Kampen 1981, Schat et al. 1991] is apparent. This is again a warning sing indicating the need to take with some caution the results of surveys and polls during an electoral process.

Finally, we focus on the analysis of the typical time for the system to relax when small perturbations take it out from the stationary state. In the symmetric case we know that $\Psi_A^{st} = \Psi_B^{st} = \Psi_o^{st}$, hence it is clear that $\sigma_A(t)$ and $\sigma_B(t)$ behave in a similar way. And in particular $\sigma_A^{st} = \sigma_B^{st} = \sigma_o^{st}$. If we assume small perturbations of the form $\sigma_i^{st} \approx \sigma_o^{st} + \delta\sigma_i(t)$ (with $i = A, B$) and $\sigma_{AB}^{st} \approx \sigma_{AB,o}^{st} + \delta\sigma_{AB}(t)$, we find again that both $\delta\sigma_A(t)$ and $\delta\sigma_B(t)$ behave in the same way, and this helps us reduce the number of equations describing the decay of correlations. Hence, we can put $\delta\sigma_A(t) = \delta\sigma_B(t) = \delta\sigma_o(t)$. The system driving the correlations becomes

$$\frac{d}{dt}\delta\sigma_o(t) = -2\Big[\alpha + \alpha' - \beta + 3\,\beta\Psi_o^{st}\Big]\delta\sigma_o - 2\Big[\alpha' + \beta\Psi_o^{st}\Big]\delta\sigma_{AB} \quad (5.30)$$

$$\frac{d}{dt}\delta\sigma_{AB}(t) = -2\Big[\alpha + \alpha' - \beta + 3\,\beta\Psi_o^{st}\Big]\delta\sigma_{AB} - 2\Big[\alpha' + \beta\Psi_o^{st}\Big]\delta\sigma_o . \quad (5.31)$$

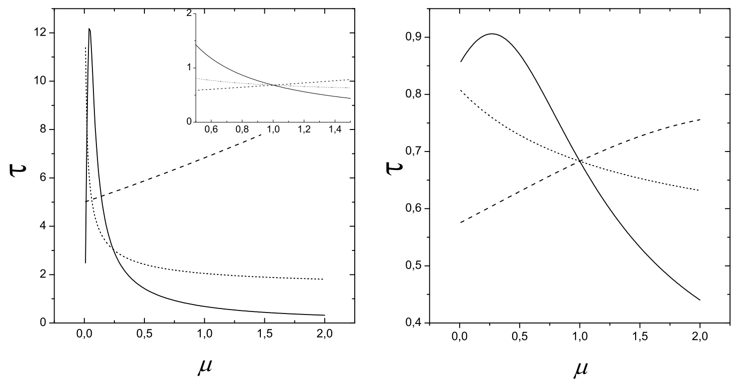

Figure 5.13: Dependence of the *dominant* relaxation time on different system parameters. On the left, symmetrical case: continuous line varying $\mu = \alpha_1 = \alpha_3$, dotted line varying $\mu = \alpha_2 = \alpha_4$, and dashed line varying $\mu = \beta_1 = \beta_2$. In order to compare all three, the dotted line was multiplied by 3, while the dashed one by 10. The inset shows, now on the same scale, the crossing of the lines at the point where all the parameters are equal to 1. On the right, asymmetrical case: continuous line varying α_1, dotted line varying α_2, and dashed line varying β_1. In all cases, the parameters that remain constant are all equal to 1.

Clearly, $\delta\sigma_o^{st} = \delta\sigma_{ab}^{st} \equiv 0$. After some algebraic steps we obtain

$$\delta\sigma_o(t) \simeq \delta\sigma_o(0)\ \exp\Big[-2[\alpha + 2\beta\Psi_o^{st} - \beta]\,t\Big] \tag{5.32}$$

$$\delta\sigma_{AB}(t) \simeq \delta\sigma_{AB}(0)\ \exp\Big[-2[\alpha + 2\beta\Psi_o^{st} - \beta]\,t\Big]. \tag{5.33}$$

These results indicate that, for the symmetrical case, the typical relaxation time is given by

$$\tau_{\text{relax}} = \frac{1}{2}[\alpha + 2\beta\Psi_o^{st} - \beta]^{-1}. \tag{5.34}$$

In Fig. 5.13 we depict the dependence of the dominant (or relevant) relaxation time, that is the slowest of the three relaxation times, for different parameters of the system. On the left, we show a symmetrical case where the different lines represent the dependence on variations of: $\mu = \alpha_1 = \alpha_3$ indicated by a continuous line; $\mu = \alpha_2 = \alpha_4$ indicated by dotted line; $\mu = \beta_1 = \beta_2$ indicated by dashed line. The strong dependence of the relaxation time on $\alpha = \alpha_1 = \alpha_3$ is apparent (in order to be represented in the same scale, the other two cases are multiplied by 3 or 10, respectively). This means that changes in the *social temperature* that, as discussed before, induce changes in $\alpha (= \alpha_1 = \alpha_3)$, could significatively change the dominant relaxation time.

For the non symmetric case the expression of the relaxation time is much more complicated than for the symmetrical case. However, in Fig. 5.13 we show its dependence on variations of the parameters of the system. As before, the different lines represent the variation of: α_1, indicated by a continuous line; α_2, indicated by a dotted line; and β_1, indicated by dashed line. It is worth remarking that, when all the the parameters (α_1, α_2 and β_1) are equal to 1, we see that the relaxation time is the same. This is shown in the inset of the left panel figure. In the asymmetrical case, the behavior is of the same order for the variation of the three parameters. However, the comment about the effect of changes on the *social temperature* remains valid.

5.3 Conclusions

In this chapter we have analyzed the effect that the *social temperature*, θ, understood as a collective climate parameter, exerts on processes of opinion formation. In the first section of the chapter we have considered the temperature effect as a tendency of the agents to act in a way that is opposite to the procedural rules of the opinion formation model. We have considered a variation of the Sznajd model in which the convincing rules are fulfilled with probability $p \propto \exp[\theta]^{-1}$. Then, with probability $(1-p)$ these rules are not fulfilled, and the spins to be updated adopt the opposite option that the one indicated by the rules. We observe that this dynamical mechanism leads to a contrarians-like effect analogous to the one described in [Galam 2004]. We found that for low temperatures the system gets to a consensus where a majority opinion emerges like in Sznajd type models. On the other hand, if temperature is above a critical threshold the density of contrarians is (on average) high enough to make it impossible for the system to reach a consensus and the opinion is equally divided between both options. However, in contrast to Galam [2004], we found that contrarians may spontaneously emerge from the dynamics when social temperature effects are taken into account. Here, we have considered different forms and the most convenient prescriptions of the Sznajd model for the analytical and the numerical analysis. However, we have checked that the phenomenon is robust and does not depend on the particular form of the model. Moreover, since the Sznajd model (as well as many other two state opinion formation models) is similar to a Ising type model [Galam 2005] up to a certain extent, we can regard our results as a sophisticated manifestation in social systems of the ferromagnetic transition in spin systems.

In the second part of the present chapter, we implemented the thermal effect as spontaneous changes of opinion that the agents can suffer during the opinion formation dynamics. We introduced a model consisting in two parties, A and B, that do not interact among them, but only through their interaction with the group I. Members of I are not able to convince those of A or B, because they do not posses a proper opinion, but instead we considered a nonzero probability of a spontaneous change of opinion from I to the other two parties and viceversa. It is this possibility of spontaneous change of opinion what inhibits the possibility of reaching a consensus: each party has some statistical density of supporters, while a statistical stationary number of undecided agents remains. As long as the direct interaction between both parties A and B remains small, the monostability will persist, and the Van Kampen's approach will remain valid. We obtained the macroscopic evolution equation for the density of supporters of A and B parties, as well as the Fokker-Planck equation governing the fluctuations around such deterministic macroscopic behavior. We have also analyzed the relaxation of small perturbations near the stationary state, and the dependence of the typical relaxation times on the system parameters was obtained. This could shed some light into the social response to small perturbations like an increase of propaganda, or dissemination of information about some "negative" aspects of a candidate, etc. However, it is important to underline that such an analysis is only valid near the macroscopic stationary state, but loses its validity for a very large perturbation. Finally, we can conclude that the inclusion of the group of undecided agents is essential to explain the fluctuations in the possible outcomes of a poll, as it is to be expected. The polarization of those undecided agents to one of the positions A or B is strongly dependent of the social temperature during the immediate time preceding the voting.

Part III

Networks

CHAPTER

6

Introduction to complex networks

6.1 Introduction

The study of networks has been traditionally in the real of Mathematics and Social Science in the context of *Graph Theory*. Such theory is one of the pillars of discrete mathematics and is rooted in the 18th century, beginning with the work of Euler, whose celebrated solution of the Königsberg bridge problem is often cited as the first true proof in the graph theory. At first, the problems analyzed by this discipline dealt with small systems, containing at most a few hundred nodes, and focused on the individual properties of its elements. Recent years, however, have witnessed a substantial new movement in network research. The current availability of computers allows the collection and analysis of more data, and the interest has shifted to the examination of large-scale statistical properties of graphs. Statistical Mechanics provides the necessary tools to carry on such analysis, and the subject of Complex Networks nowadays represents a focus of intense activity in the Physics community.

Complex networks analysis may be applied to many real systems that can be mapped as graphs. Examples include the Internet, social networks among individuals, networks of business, relations between companies, neural networks, metabolic networks, and many others. A network is a collection of *vertices* or *nodes*, connected by a set of *edges* or *links*. However, these mathematical items may be more complex than this simple definition. For instance, there may be more than one different type of

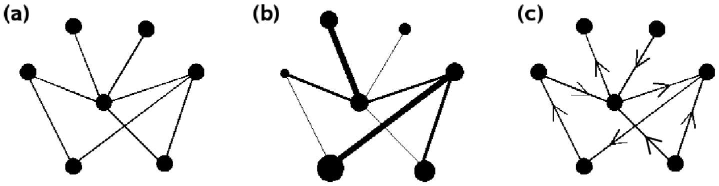

Figure 6.1: Examples of various types of networks: (a) an undirected network with only a single type of vertex and a single type of edge; (b) a network with varying vertex and edge weights; (c) a directed network in which each edge has assigned a preferred direction.

vertex in a network, or more than one different type of edge. Very often the links of the network are labeled with *weights* that represent, for instance, the different capacity of each connection in a transportation network or the connection strength between two nodes. They can also be directed, pointing in only one direction, and thus we talk about directed graphs or, sometimes, *digraphs*. A graph representing email messages between individuals would be directed, since each message goes in only one direction. Many other levels of sophistication can be added, according with the variety of networks that can be found in Nature. For instance, one can also consider *hyper-edges* connecting more than two vertices together. Graphs may also evolve over time, with vertices or edges appearing or disappearing, as well as values defined on those vertices and edges changing. In this chapter we introduce some common features of graphs, and we provide a short approximation to the state-of-art in network modeling and to the dynamics of processes that may take place on them.

6.2 Random and Scale-free graphs

The degree distribution is one of the most basic quantitative properties of a network, and its functional form determines many of its features. The *degree* of a node is the number of edges connected to that node. Thus, the degree distribution of a network represents the probability that a vertex chosen at random has degree k.

Random graphs

In a *random graph* the links between nodes are placed simply at random, and the resulting degree distribution is Poissonian, or binomial in the small size limit, with $P(k) \sim e^{-\langle k \rangle} \langle k \rangle^k / k!$. Both functional distributions are strongly peaked around the mean $\langle k \rangle$ and exhibit a tail for large values of k that rapidly decays as $1/k!$. This means that in these graphs most nodes have degree close to the mean value.

Probably the biggest impact on the development of a mathematical theory of random graphs was due to Erdős and Rényi [1959; 1960]. According to the ER model, every pair of the N nodes of a network is connected independently with probability p, creating a graph with approximately $pN(N-1)/2$ edges randomly distributed. This extremely simple model gives rise to random graphs whose structure varies with the value of the connecting probability, since they exhibit a phase transition from a disconnected to a fully-connected structure for increasing values of p. Below the critical probability p_c the network is composed of isolated clusters, but above p_c a giant cluster spans the entire graph and most of the nodes are connected by paths through the network. This phenomenon can be studied as a manifestation of a percolation transition on networks [Albert and Barabási 2002].

Random graphs have fundamented the analysis of complex networks for decades after its introduction in the late 1950s. In Physics, they have been employed to study a variety of systems too, as spin models [Barrat and Zecchina 1999], random walks [Cassi 1996], and quantum chaos [Kottos and Smilansky 1997]. However, real-world networks are mostly found to be very distinct from random graphs. In order to obtain more realistic networks, non-Poisson degree distributions were incorporated. This lead to the so-called configurational model [Molloy and Reed 1995], that enables to build *generalized random graphs* with an arbitrary degree distribution. Basically this model consists in assigning to each vertex a certain number of possible connections or *stubs* according to a previously determined degree distribution, and then the network is built randomly choosing pairs of stubs and connecting them to form the edges.

Scale-free graphs

As it has just been pointed out, real networks are often far from Poissonian. Indeed, in many real networks the node degree distribution is highly rightskewed, meaning there is a long right tail to values that are far above the mean. In other words, there exist some few nodes, called *hubs*, that exhibit a large number of connections. These networks apparently exhibit no characteristic scale and display a power-law degree distribution $P(k) \sim k^{-\lambda}$. Such graphs are called *scale-free* (SF) networks [*cf.* Fig. 6.2]. Examples are the World-Wide Web [Albert et al. 1999], protein networks [Jeong et al. 2001], and language [Ferrer i Cancho and Solé 2001] or sexual contacts networks [Liljeros et al. 2001]. The exponent in the power law distribution has been obtained for many different real-world networks, and it usually has values in the range $2 < \lambda < 4$ [Newman 2003, Albert and Barabási 2002].

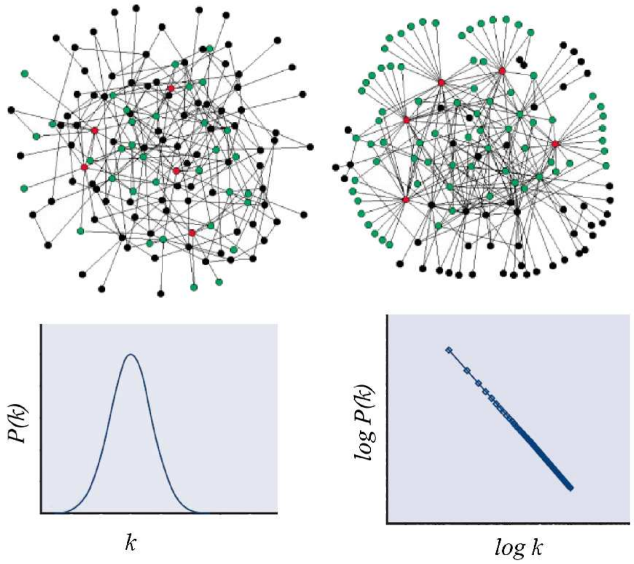

Figure 6.2: The random network generated by the ER model is rather homogeneous (*left*), while the scale-free network is extremely inhomogeneous and few nodes have a large number of links (*right*). In both graphs the five nodes with the largest number of connections are colored in red, and its first neighbors are colored in green. While in the exponential network only 27% of the nodes are reached from these five highlight nodes, in the power-law distributed graph more than the 60% of the nodes are reached from them. This evidences the key role that hubs play in scale-free networks. Both graphs contain the same number of nodes and links. Ref. [Barabási 2003].

Scale-free networks can be constructed in different ways. If one strictly focus on the network topology, they can be built as generalized random graphs with power-law degree distribution [Newman et al. 2001, Catanzaro et al. 2005]. However the degree distribution alone does not characterize the graph in full, and these *random scale-free networks* do not capture all the features that most real power-law distributed networks exhibit. It has been claimed that the nature of such networks is rooted at their dynamical assembly [Newman 2003]. Thus, several models have been proposed to describe SF network formation, in which vertices and edges are gradually added to the graph in some manner intended to reflect real network growth mechanisms. An early model was proposed by Price [1976], based on what he called *cumulative advantage*. This idea was much later adopted in the *preferential attachment* (PA) mechanism in the well-known Albert-Barabási model, in which the likelihood of connecting a new node to the existing ones depends on the node degree [Barabási and Albert 1999]. Although PA is widely accepted as the probable explanation of most of the observed real scale-free networks, other mechanisms based on *vertex copying* have been proposed [Kleinberg et al. 1999, Vazquez et al. 2003, Krapivsky and Redner 2005], in which new nodes choose an existent node at random and copy a fraction of its links. These models may describe, for instance, some biochemical power-law distributed networks for which PA seems to be a non appropriate model [Kim et al. 2002b, Solé and Pastor-Satorras 2003, Newman 2003].

6.3 Mixing patterns and clustering

In order to observe deeper patterns in network structures one can look at the tendency for vertices to be connected to other vertices that are like (or unlike) them in some specific way. This kind of selective linking is called *assortative* (or *dissortative*) mixing. A special case of assortative mixing by a scalar vertex property is mixing according to vertex degree, also commonly referred to simply as *degree correlation*. This particular case is interesting since degree is itself a property of the graph topology, and degree correlations can give rise to some interesting network structure effects.

Several different ways of quantifying degree correlations have been proposed. One can simply plot the two-dimensional histogram of the degrees of vertices at either ends of an edge, as was done by Maslov et al. in Ref. [Maslov and Sneppen 2002, Maslov et al. 2004], where they showed results for both protein interaction networks and the Internet. A more exhaustive way to detect correlations is to calculate the average degree of the neighbors of a node with degree k [Pastor-Satorras et al. 2001, Zhanga and Zhou 2007]. This number is formally defined as:

$$\langle k_{nn} \rangle (k) = \sum_{k'} k' P(k'|k) \tag{6.1}$$

where $P(k'|k)$ is the conditional probability that an edge of a node with degree k points to a node with degree k'. If there are no degree-degree correlations $P(k'|k)$ only depends on k' and the neighbor connectivity $\langle k_{nn} \rangle$ is a constant. However, if this function increases with k, the network is assortative, since nodes of high degree connect, on average, to nodes of high degree. Alternatively, if the function decreases, the network is dissortative, since nodes of high degree tend to connect to nodes of lower degree.

The level of degree correlations can also be quantified in terms of an *assortativity coefficient*, introduced by Newmann in the general context of mixing patterns according to scalar properties of the vertex [Newman 2002]. For the particular case of mixing by vertex degree in a graph with M links, this coefficient takes the form

$$r = \frac{M^{-1}\sum_i j_i k_i - [M^{-1}\sum_i \frac{1}{2}(j_i + k_i)]^2}{M^{-1}\sum_i \frac{1}{2}(j_i^2 + k_i^2) - [M^{-1}\sum_i \frac{1}{2}(j_i + k_i)]^2} \tag{6.2}$$

where j_i, k_i are the degrees of the vertices at the ends of the ith edge, with $i = 1, ..., M$. This definition is nothing but the Pearson correlation coefficient of the degrees at either ends of an edge. Indeed, it can be written in a more familiar way in terms of the pairs of connected nodes as

$$r = \frac{\langle k_i k_j \rangle_{i>j} - \langle k \rangle^2}{\sigma_k^2} , \tag{6.3}$$

where $\langle k \rangle$ and σ_k are, respectively, the mean and standard deviation of the degree distribution and the $\langle ... \rangle_{i>j}$ term is averaged over all the nearest-neighbor pairs in nodes of the network. Thus, networks with positive values of r are assortative and tend to have a core-periphery structure. The nodes with high degree are attracted to one another forming a highly interconnected core surrounded by a periphery of lower-degree nodes, as shown in Fig. 6.3(a). On the other hand, in dissortative correlated networks, the high-degree nodes tend to be scattered more broadly over the network, as shown in Fig. 6.3(b).

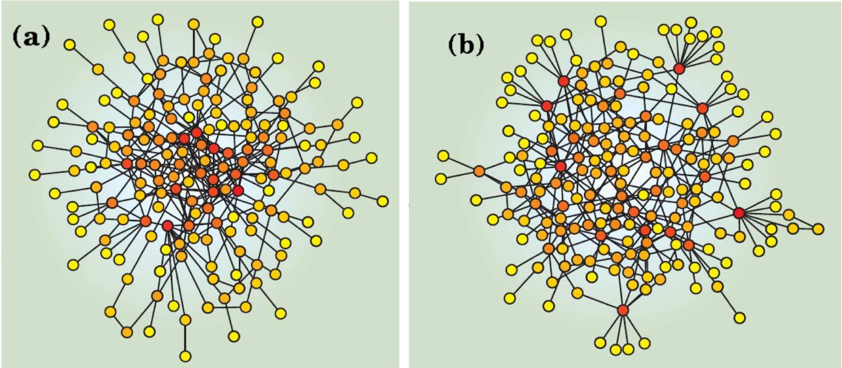

Figure 6.3: Two networks built with the same degree distribution but with different mixing according to vertex degree: assortative (*a*) and dissortative (*b*). Nodes are colored according to their degree (from yellow to red as their degree increases). The former is positively correlated and exhibit a clump of high-degree nodes. The latter is negatively correlated and the high-degree nodes spread over the graph as they tend to connect to nodes of lower degree. From Ref. [Newman 2008]

It is clear that degree correlations have a strong effect on the structure of networks as well as on the behavior of the processes that take place on them. A disease, for instance, can more easily persist in a positively correlated network by circulating in the dense core where there are many opportunities to spread. In a negatively correlated graph, the same disease finds it harder to persist and, if it does, then it typically spreads over the whole network. Random graphs with arbitrary degree distribution do not exhibit degree correlations [Newman et al. 2001, Catanzaro et al. 2005]. On the other hand, Krapivsky and Redner [2001] have shown that, in the scale-free graphs generated with the Barabási-Albert model, correlations develop spontaneously between the degrees of connected nodes during the network growth. The assortativity coefficient has also been measured for many real-world networks [Newman 2002], and some of these results are shown in table 6.1.

Table 6.1: Assortativity coefficient measured for various real-world networks of size N [Newman 2002]. From top to botton: collaboration networks of scientists in physics, collaborations between film actors, connections between autonomous systems on the Internet, protein-protein interactions in yeast, and the synaptic connections in the neural network of a nematode.

Network	N	r
Physics coautorship	52909	0.363
Film actors collaborations	449913	0.208
Internet	10697	-0.189
Protein interactions	2115	-0.156
Neural network	307	-0.163

Up till now we have focused on nearest-neighbor degree correlations. However, three node correlations are also interesting to analyze network structure. Analogously to the previous case, three node correlations can be measured by means of the probability $P(k', k''|k)$ that a node of degree k is simultaneously connected to nodes with degree k' and k''. The direct evaluation of this conditional probability is generally difficult. To overcome this problem, another interesting alternative quantity, the *clustering coefficient*, is frequently used. By definition, the clustering coefficient of a node i with degree k_i is defined as the probability that two neighbors of this node are also neighbors themselves [Watts and Strogatz 1998]. This local coefficient is computed as $C_i = t_i/\binom{k_i}{2}$, where t_i is the number of links among the node neighbors (triangular connections) and $\binom{k_i}{2}$ is the number of possible pairs that could exist among its k_i neighbors. To characterize the clustering coefficient of the whole graph, the most extended criterion is [1]

$$C = \frac{\sum_{i=1}^{N} t_i}{\sum_{i=1}^{N} \binom{k_i}{2}} = \frac{3 \times \text{number of triangles}}{\text{number of pairs of adjacent edges}} \,. \tag{6.4}$$

In contrast with ordered lattices, whose clustering only depends on their coordination number, complex networks exhibit size dependent clustering coefficients. In a random graph the probability of connection for two neighbors is equal to the probability that two randomly selected nodes are connected. Consequently, the clustering coefficient for a random graph is $C_{rand} = \frac{\langle k \rangle}{N}$. On the other hand, scale-free networks exhibit larger values of clustering. Numerical simulations indicate that for Albert-Barabási SF networks the clustering coefficient decays with the system size as $C \sim N^{-0.75}$ [Albert and Barabási 2002], and also a high degree of clustering has been observed in many SF real networks [Ravasz and Barabási 2003, Vázquez et al. 2002].

This high probability of interconnection between the neighbors of a given node leads in turn to another interesting analysis in the study of SF networks, that is the appearance of hierarchical and community structures [Everitt 1974, Ravasz and Barabási 2003, Soffer and Vázquez 2005]. The development of methods for finding communities within networks is nowadays a sub-area of intense activity, with an enormous number of different techniques under development [Lancichinetti et al. 2008, Arenas et al. 2008, Pollner et al. 2006].

6.4 Small-world effect

In a network, the distance between two nodes is defined as the number of edges along the shortest path connecting them. The diameter d of a network, therefore, is defined to be the average path length of the graph, *i.e.*, the mean distance between two nodes averaged over all pairs of nodes. This quantity determines the effective size of a network, the most typical separation of one pair of nodes therein.

An interesting feature of most complex networks is that their diameter is relatively smaller than that of regularly constructed graphs with the same number of vertices and edges. For instance, in a random graph the mean number of neighbors at distance ℓ away from a vertex is $n \sim \langle k \rangle^{\ell}$, and hence the typical value of d needed to

---

[1] Other definitions of the clustering coefficient are also found in literature. C is often defined as the average value of the local clustering coefficients of each node. However, as shown in Ref. [Bollobás and Riordan 2003], both definitions of the global coefficient are nor equivalent.

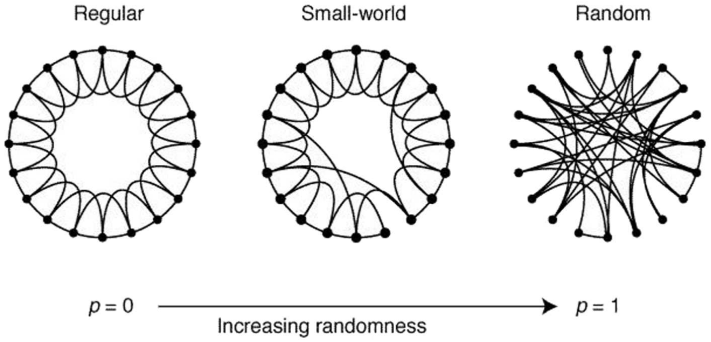

Figure 6.4: Starting from a regular lattice, the Watts-Strogatz model randomly rewires its edges with probability p. Results for different values of the rewiring probability are shown. For $p = 0$, the original lattice is unchanged; as p increases, the graph becomes increasingly disordered until for $p = 1$, for which all edges are rewired randomly. For intermediate values of p, the graph is a small-world network: highly clustered like a regular graph, yet with small characteristic path length, like a random graph. Ref. [Watts and Strogatz 1998].

encompass the entire network from a typical central node scales as $d \sim \ln N$. This smallness leads to the idea of the small-world effect, hence the name of *small-world networks*.

One of the first proofs of the small-world effect in real networks was performed in the $1960s$ by Milgram [1967]. In his experiment some letters were given to randomly chosen people and passed person to person till reaching a designated target individual. Only a small number of steps, around six, were necessary for the mail to reach its final destination. Later, Watts and Strogatz [1998] observed that many real-world graphs have a small average shortest path length. They proposed a model to build small-world graphs starting from a low-dimensional regular lattice and then randomly adding or moving edges to create a low density of “shortcuts” that connect remote parts of the lattice to one another. This rewiring mechanism allows to interpolate between a regular lattice and a random graph, giving rise to highly clustered structures with low path lengths. As the rewiring probability increases, such networks exhibit a crossover from a “large world” (as a regular lattice) to a small-world random network [Barthélémy and Amaral 1999, Barrat and Weigt 2000].

In recent years the term small-world has been sharpened and given a more precise meaning: networks are said to show the small-world effect if the network diameter

d scales logarithmically or slower with network size for a fixed mean degree. Logarithmic scaling can be proved for a variety of network models [Newman et al. 2001, Albert and Barabási 2002] and has also been observed in various real-world networks [Newman 2001, Amaral et al. 2000]. Even more, some networks have been observed to have mean vertex-vertex distances that increase slower than $\ln N$. Cohen and Havlin [2003] found analytically that for scale-free networks with $2 < \lambda < 3$ the diameter of the graph behaves as $d \sim \ln(\ln(N))$, for which they coined the name of *ultra-small world* networks.

6.5 Processes on networks

A natural step after analyzing the structure of networks is to look at the behavior of dynamical processes that may take place on them. Real networks are the basis for a wide range of mechanisms in which the topology of the underlaying network plays a crucial role. In many cases the time scales describing the network growth and the dynamical process that take place on the graph are widely different, then the dynamics can be modelled considering a fixed network structure. A good example is the Internet traffic, which involves a time resolution from millisecons up to a day, while periods of order of months are required for significant topological changes in the network structure. On the other hand, when the time scales governing the dynamics on the network are comparable with the characteristic times defining its assembly, the supported process can itself influence network structure and growth. This is the case, for instance, of some biological models inspired by the emergence of cellular structures.

Many dynamical processes have been studied on networks. The topics under investigation include weakly coupled oscillators [Barahona and Pecora 2002, Hong et al. 2002], neural networks [Lago-Fernández et al. 2000], social influence phenomena [Sánchez et al. 2002], and iterated games and coopertation models [Abramson and Kuperman 2001, Ebel and Bornholdt 2002, Kim et al. 2002a].

Understanding the effects that the network structure has on the dynamics is a hard task since the topological features of complex networks are not fully understood yet. However, there have been some important advances in last few years. In this context, *spreading and diffusion* have been studied on several types of networks, from regular structures [Keeling 1999] to random [Weigt and Hartmann 2001], small-world [Moukarzel 1999, Kuperman and Abramson 2001] and scale-free networks [Bilke and Peterson 2001, Dezső and Barabási 2002]. Epidemic models can be easily formulated on networks, in which nodes represent the agents that may be infected and links represent the possible contacts along which the epidemic diffuses. Particularly interesting is the analysis provided by Pastor-Satorras and Vespignani [2001; 2003] about the influence of the network topology on the spread of viral diseases. They showed that, while on a random network a local infection spreads over the whole graph only if the spreading rate κ is larger than a critical value κ_c, for a scale-free network any spreading rate leads to the infection of the entire graph. This lack of any epidemic threshold arises from the extreme degree heterogeneity and high clustering that these graphs exhibit. Hence, the scale-free nature of networks calls for different immunization strategies in order to eradicate infections. In contrast to standard models, SF networks do not acquire global immunity in the presence of a high density of randomly immunized individuals, but successful immunization strategies must take into account the inhomogeneous connectivity patterns.

Percolation theory has also been studied on networks, not only related to epidemic spread but also to analyze the network resilience. Real-world networks are often found to be highly resilient to the random deletion of vertices. A percolation process is one in which vertices or edges on the graph may be either “occupied” or “unoccupied” and one analyzes the properties of the resulting pattern and contiguous clusters of occupied/unoccupied items. These clusters determine whether the graph is fully connected or a set of disconnected subgraphs, which usually implies a network failure. Resilience can be measured in different ways. Perhaps the simplest indicator of resilience in a network is the variation in the fraction of vertices belonging to the giant component of the graph, *i.e.*, the largest fully-connected subgraph. Callaway et al. [2000] proposed a percolation method in which the probability of occupation of a vertex can be any function of the degree of that vertex. In order to analyze the network resilience, this method allows to remove vertices from the graph in an order that depends on their degree. In agreement with Pastor-Satorras and Vespignani results, they found that networks with power-law degree distributions are highly susceptible to this type of targeted attack; one needs to remove only a small precentage of vertices to destroy the giant component entirely. Similar results were also found independently by Cohen et al. [2001] using a similar method.

Dynamical searching processes have also attracted much interest. Suppose some resource of interest is stored at the vertices of a network, such as information on Web pages or computer files on a distributed database. One would like to be able to rapidly determine where on the network a particular item of interest can be found (or determine that it is not on the network at all). It has been shown that the shortest paths between nodes of the graph can be found employing local strategies, *i.e.*, with strategies that do not require precise global information of the network. Theoretical explanations of this mechanism have been given by Kleinberg [2000] and Watts et al. [2002], based on the idea that the structure of the network provides information that can be exploited heuristically in a search process. In scale-free communication networks and in some decentralized peer-to-peer communication networks it has been shown that the existence of highly connected hubs allows the design of quite efficient local search algorithms [Adamic et al. 2003].

Further investigations carried out in the context of communication networks focus on the traffic derived from the communication process itself. Some stylized models of traffic flow [Arenas et al. 2001, Ohira and Sawatari 1998, Solé and Valverde 2001] can be used to gain intuition about dynamics on complex networks, and to determine the leading parameters of the dynamic processes related to the network topology. The main results obtained up to now about traffic flow in complex networks are related to the determination of bounds for this flow to become congested. In the following chapter, we present original research work on this topic.

CHAPTER

7

Optimization of transport protocols

7.1 Transport processes on networks

In this chapter, we focus on the transport capacity of communication networks and present our own research work concerning congestion phenomena. Transportation processes are ubiquitously present in our lives and nowadays play a decisive role in the progress and development of human societies. Everyday communication networks are used all around the world for different purposes, as for transferring of information (*e.g.* the Internet) or transportation of goods and people (such as networks of roads and airlines). This relevance, exponentially increasing over the past years, explains the intense activity in the study of such transportation networks, in fields as diverse as Biology [Tlalka et al. 2003], Informatics [Ohira and Sawatari 1998, Solé and Valverde 2001], or urban planning (vehicular traffic) [Nagel and Schreckenberg 1992, Nagel and Paczuski 1995].

Tools taken from Statistical Mechanics are often employed to study the topological properties of these communication networks and also their dynamics. Particularly interesting is the analysis of congestion. A transition from a sparse to a jammed phase may occur due to increased traffic, yielding an increase in the transit time of information. A clear example of that is the first Internet collapse reported in the literature, occurred in October of 1986. It was reported that, due to this collapse, the connection speed between two places separated 200 meters dropped by a factor of 100 [Jacobson

1988]. This transition has also been observed in many numerical simulations. For instance, in models of traffic flow, such as the Nagel-Schreckenberg model [Nagel and Schreckenberg 1992]. The referred work shows how, as the density of cars ρ increases, a well-defined transition that separates a fluid phase from a jammed phase occurs. At the critical threshold ρ_c, the jams are observed as back-propagating waves with fractal properties.

Therefore, many efforts have recently focused on understanding the physics of congestion for general communication processes to optimize the transport capacity of the information networks. A general collection of models that captures the essential features of communication processes has been proposed [Arenas et al. 2001, Ohira and Sawatari 1998, Solé and Valverde 2001]. These models include the basic ingredients for communication between two elements:

– Physical support for the communication process (agents and channels).

– Discrete information packets that are exchanged

– Limited capacity of the agents to handle such packets.

In what follows we will refer to a general model defined as a communication network mapped onto a lattice, where the N nodes represent the communicating elements and the links between them represent communication channels. The packet transmission is modeled by a discrete time parallel algorithm. The information packets flow via neighbor connections toward its final destination, and every node stores in queue the packets received from its neighbors. The algorithm basically consists of three operations at each time-step:

- **Packet generation:** every node introduces a new packet in the system at rate γ, independently from the rest of the nodes. The final destination of this new packet is chosen at random from the remaining $N-1$ nodes. The packet is then appended at the end of the host tail that the node stored in previous steps.
- **Routing:** according to a set of previously defined routing paths, every node sends the packets at the head of its queue to one of its neighbors. The nodes can deliver, on average, only a finite number of packets at each time step and, without lost of generality, this number can be fixed to 1.
- **Reception:** the nodes can receive an unlimited number of packets. If the recipient node is the target destination, the packet is eliminated from the system. Otherwise the node stores it at the end of its queue. All the packets received in the same time step are randomly ordered in a subqueue appended to the existing tail. This randomization is needed because times are not resolved below the single-packet processing time scale.

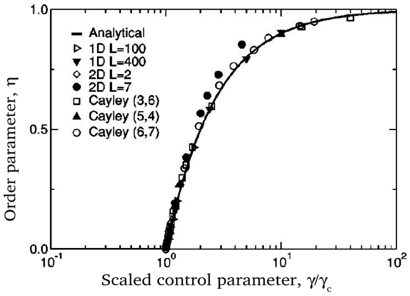

Figure 7.1: Behavior of the rate of steady-state packet growth $\eta(\gamma)$ for a communication model according with the previous general description . The solid line corresponds to the analytical calculation for two nodes exchanging information packets. Symbols corresponds to simulations performed in regular lattices of dimmension $d = 1$, $d = 2$ and hierarchical Cayley lattices. Ref. [Guimerà et al. 2002a].

It has been observed in Refs. [Arenas et al. 2001, Ohira and Sawatari 1998, Solé and Valverde 2001] that, for low values of the packet generation rate γ, the system reaches a steady state in which the total number of floating packets in the network, $P(t)$, fluctuates around a finite value. As γ increases the system undergoes a continuous transition to a congested phase in which $P(t) \propto t$. At the critical point, γ_c, the number of packets present in the network diverges, as well as other quantities as the delay times and the queue lengths [Guimerà et al. 2002a, Solé and Valverde 2001].

Thus, to characterize this transition, the *rate of steady-state packet growth* is introduced as a convenient order parameter [Arenas et al. 2001, Sreenivasan et al. 2007]

$$\eta(\gamma) = \lim_{t \to \infty} \frac{1}{\gamma N} \frac{\langle \Delta P \rangle}{\Delta t} , \tag{7.1}$$

where $\Delta P = P(t + \Delta t) - P(t)$ and $\langle ... \rangle$ indicates average over time windows of width Δt. Essentially, this order parameter represents the ratio between undelivered and generated packets at the stationary state. For $\gamma > \gamma_c$ the system collapses, $\langle \Delta P \rangle$ grows linearly with Δt, and therefore $\eta = \eta(\gamma)$. On the other hand, for $\gamma < \gamma_c$, $\langle \Delta P \rangle = 0$ and $\eta = 0$.

Further analysis of this sparse/congested transition has been carried out [Arenas et al. 2001] to analyze the behavior of the system when the number of delivered packets depends on the queue length of the nodes. If the agents are able to deliver more packets as they are more congested then the network never collapses. On the other hand, if agents deliver fewer packets as their loads increase, then the system exhibits a discontinuous transition toward a congested phase and the network collapses in an inhomogeneous way, giving rise to several congestion nuclei. Only in the case in which the delivering capacity of the nodes is independent of their load, the dynamics leads to the previously described critical phase transition.

In order to avoid congestion and optimize the transport capacity of the networks, many efforts have been focused on enhancing the critical threshold γ_c. This would allow to cope with a higher number of packets while the system is still in the sparse phase. Several studies [Yan et al. 2006, Sreenivasan et al. 2007, Danila et al. 2006] have shown that the transport capacity of these communication networks (quantified by the packet insertion rate at which jamming occurs) can be optimized by means of optimization of the routing criterion employed to send the packets from one node to one of its neighbors at every time step.

The sequence of nodes and edges that a given packet visits during its flow toward its destination constitutes the route for that source-destination pair of nodes. For a network of size N, the routing problem consists in finding an assignment of routes for all $N(N-1)/2$ pairs of nodes of the graph. This set of paths conform the assigned *static routing protocol* (SRP) to the communication network. A quantity of interest for a given SRP is the *centrality* or *betweeness* b_i of each node, defined as the total number of paths that pass through node i [Newman 2001]. The jamming effect is directly related with the betweeness distribution of the SRP. Indeed the congestion threshold γ_c can be expressed in terms of the maximal node betweeness B as follows. The average packet current incurred from a given source node s to certain destination node d is $\gamma/(N-1)$, as the destination of every generated packet at s is randomly chosen from the remaining $N-1$ nodes. This current flow through the network following the routing path given by the SRP. Thus, for a node with betweenness b the average packet inflow current will be $b\gamma/(N-1)$. Since the outflow of packets occurs at unit latency, we will have queuing and congestion at the node for which this quantity reaches unity for the first time, namely at the node with maximal betweenness B. Then it can be expressed as

$$\gamma_c = \frac{N-1}{B} \, . \tag{7.2}$$

From this equation follows that for a given SPR the dependence of the congestion threshold γ_c on the network size is determined by the scaling with N of the maximal node betweenness. Therefore the optimal routing protocol, from the point of view of congestion avoidance, should be the one for which B exhibits the slowest growth with N. In other words, the optimal SRP implies a betweenness distribution as homogeneous as possible, giving rise to a maximal node betweenness $B \sim N^{1+\varepsilon}$ with the minimal value of ε. [Guimerà et al. 2002a].

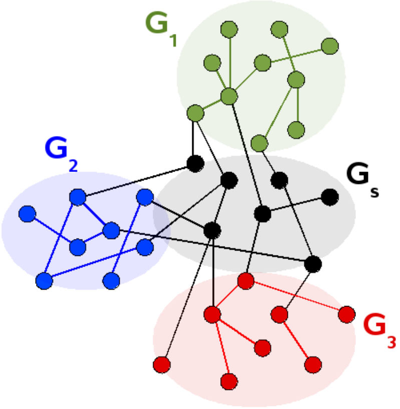

Figure 7.2: Illustrative sketch of a vertex separator G_s that divides the network in three disconnected subgraphs, in such manner that every path from G_i to G_j pass through G_s if $i \neq j$.

But minimizing B is not a simple task. It was shown in Ref. [Sreenivasan et al. 2007] that there exists a lower bound B_T for the maximal node betweenness given by the network topology. This limit is independent of the routing protocol employed, and implies that congestion can never be avoided for large enough values of the packet insertion rate, $\gamma > \gamma_T$. Here we briefly expose the graph partitioning arguments employed by Sreenivasan et al. [2007] to introduce B_T. A subgraph G_s is extracted from the whole graph G, in such manner that the rest of the graph becomes a set of n disconnected subgraphs G_i with $n \geq 2$. Then G_s is called a *vertex separator* of G (see Fig. 7.2). The number of nodes contained in a subgraph G_i is denoted by $|G_i|$. Since G_s is a separator set, there is at least $\sum_{i,j} |G_i||G_j|$ routes passing through G_s for any SRP. In this case the average betweenness of the nodes of G_s is $B_s = \{\sum_{i,j} |G_i||G_i|\}/|G_s|$. Since the maximum is always larger or equal than the average, the maximum betweenness of the nodes in G_s must be no less than B_s. Considering all the possible choices of vertex separators, there will be an optimal one for which B_s is as small as possible. Thus, this is the lower bound B_T for the maximal node betweenness given by the network topology.

Sreenivasan et al. [2007] focused on the particular case of random, uncorrelated, scale-free networks. They estimated the scaling of B_T with the network size N as

$$B_T \lesssim B_{est} \sim N^{\frac{\lambda}{\lambda-1}} , \tag{7.3}$$

where $P(k) \sim k^{-\lambda}$ is the degree distribution of the graph. When $\lambda \to \infty$ the network approaches a random regular graph and Eq. (7.3) estimates $B_{est} \sim N^0$. On the other hand, for $\lambda = 2$ the network becomes a star-like graph, for which the only possible separator is the central node and $B_{est} \sim N^2$. Between these two limits, scale-free networks typically employed in communication problems present a degree distribution with $2 > \lambda > 3$. Thus one could expect a topological bound for the maximal node betweenness of $B_T \lesssim B_{est} \sim N^{3/2}$ (same as for $\lambda = 3$ in Eq. (7.3)).

Traditionally, Shortest-Path (SP) based protocols have been applied as the best option to optimize the transport capacity of networks. Focusing on SF networks with $\lambda = 2.5$, we observe that the maximal node betweenness scales as $B_{SP}(\lambda = 2.5) \sim N^{1.6}$ [Danila et al. 2006], which is in quite good agreement with the estimation of B_T provided in Eq. (7.3). However, the optimality of SP routing protocols is clearly questioned in the light of the above exposed arguments. SP algorithms minimize the length of the routing paths, but do not take into account minimization of the maximal betweenness.

At this point the following question arises: *Is it possible to design an optimal SRP whose maximal node betweenness approaches B_T better than the Shortest-Path SRP?*.

Recently, other algorithms have been proposed to replace the traditional Shortest-Path SRP. In Ref. [Sreenivasan et al. 2007] a hub avoidance (HA) method is introduced. This algorithm surpasses the scaling of the topological estimation B_{est} with $B_{HA}(\lambda = 2.5) \sim N^{1.42}$. This is a significant improvement over the SP protocol. The work presented in Ref. [Yan et al. 2006] also provides an alternative SRP based on the redistribution of the paths toward the lower degree nodes. In this case they obtained $B_{ER}(\lambda = 2.5) \sim N^{1.31}$.

An alternative and useful method to minimize the maximal node betweenness consists of an iterative method that detects the node with highest centrality B and somehow reduces it. Based on this criterion, Danila et al. [2006] proposed a optimization algorithm that reduces the maximal betweenness in a deterministic way, by increasing the weights of all the links of the maximal betweenness node. With this method they achieve $B_{DAN}(\lambda = 2.5) \sim N^{1.185}$. Following this line of thought, we propose here an alternative stochastic algorithm that differs from Danila's deterministic optimization method. With the aim at preserving a stronger compromise between *optimization* and *short-distances*, we have designed a new stochastic algorithm that, based on extremal optimization [Boettcher and Percus 2001], minimizes the maximum node betweenness keeping the path lengths as short as possible. The addition of this constrain gives rise to an algorithm that, although it is not able to reach better optimization for the betweenness than other already proposed methods [Danila et al. 2006], it is able to keep the paths with only small fluctuations over the initial SP protocol.

7.2 Our proposal for an optimal SRP

We now focus on power-law degree distributed networks, $P(k) \sim k^{-\lambda}$, with $\lambda = 2.5$ to facilitate the comparison with previous studies [Yan et al. 2006, Sreenivasan et al. 2007, Danila et al. 2006] [1]. In order to generate our ensemble of networks, we employ the configurational model [Molloy and Reed 1995] introduced in Sec. 6.2. Each node is first assigned a random integer $k > k_0$ according to the degree distribution $P(k)$, where $k_0 = 2$ is the minimal number of links for each node that guarantees the full connection of the graph. Next we randomly select stubs and connect them to form the edges, respecting the preassigned degrees and avoiding multiple and self-connections. We consider an additional restriction on the maximum possible degree of the vertices, $k_{max} \sim N^{1/(\lambda-1)}$, to build graphs with no degree-degree correlations [Catanzaro et al. 2005]. This restriction ensures that, on average, only one node has k_{max} connections, *i.e.*, $1/N = \int_{k_{max}}^{\infty} P(k)dk$.

The optimization algorithm starts from the non-degenerated Shortest-Path SRP. So once the network is built, the first step is to calculate the SP using Dijkstra's algorithm [Cormen et al. 2005]. As this optimization is based on an iterative minimization of the maximal node betweenness, we must also calculate the number of paths passing through each node for this initial SP routing table. In Ref. [Newman 2001] the betweenness b_i of the node i is defined as the sum of all the fractional paths that pass through that node. In other words, degenerated paths are considered. Therefore, the number of times that an information packet passes through the node i on its way from a source node s to a destination node d is computed as follows: the source node s is assigned a weight $w = 1$ and then the weight of every node along each path is split evenly among its predecessors in the routing table. Thus, the weight of a vertex i represents the number of distinct paths from the source vertex to i. The betweenness of the node i is then calculated as $b_i = 1 + \sum_j b_j(w_i/w_j)$, where the first term is the contribution of the path (s, i) and the second term takes into account the contribution derived from all the neighbors j immediately below the vertex i. However, for the present optimization algorithm we follow the convention of considering only one path for each pair of nodes (s, i). Therefore, the probability of choosing certain path is equally distributed between all possible degenerated paths. To illustrate the betweenness calculation, we present an schematic picture in Fig. 7.3.

Once the initial SP protocol and the corresponding betweenness are calculated, we proceed to optimize the table of the $N(N-1)/2$ routing paths. To unequivocally identify them, we assign to every path (i, j) a label $\mathcal{L}$ as follows

---

[1] Nevertheless, we have also performed the study on networks with $\lambda = 4.5$ finding no qualitative difference in the final results.

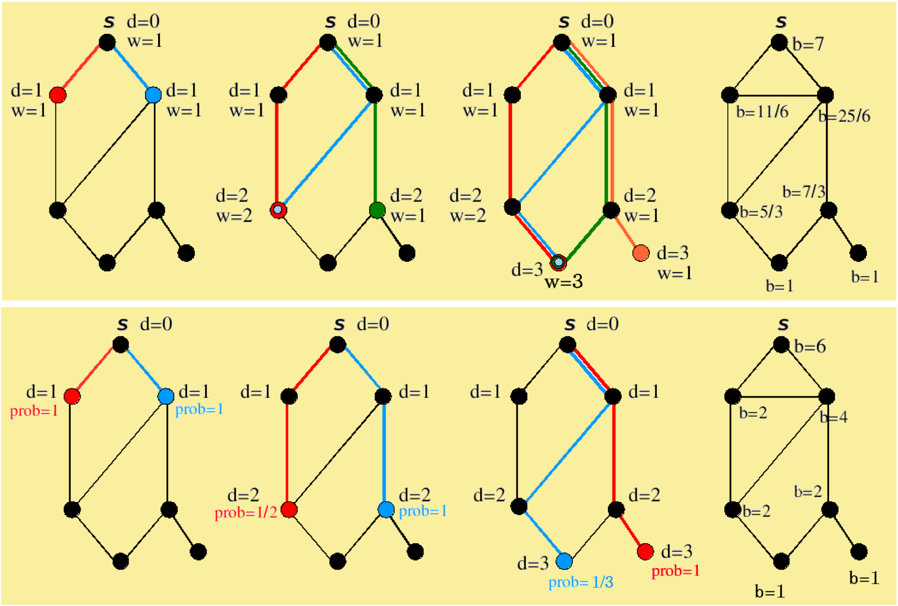

Figure 7.3: Calculation of betweenness for nodes at distance d from the source node s. *Top:* All degenerated SP from s to every node are considered. Each node is assigned a weight w that represents the number of distinct paths touching it. The centrality b of a node is then defined as the sum of all fractional paths that pass through that node. *Bottom:* only one shortest-path is considered to connect each node to the source s. When several w degenerated paths are possible, one of them is chosen with probability $prob = 1/w$.

$$\mathcal{L}(i,j) = (i-1)N - \frac{(i-1)i}{2} + j - i\,, \tag{7.4}$$

where $i = \min(i,j)$ and N is the network size. Since we are dealing with non directed graphs we have $\mathcal{L}(i,j) = \mathcal{L}(j,i)$. An illustrative interpretation of Eq. (7.4) is shown in Fig. 7.4 for a system of size $N = 5$. For every node i we store the labels of the b_i paths passing through it. Up to this point we have our initial SRP unequivocally described since we know the path labels assigned to each node and the link connections of the graph [2].

---

[2] This statement will be strictly valid if there are no triangular connections involved in the paths definition. However, the networks built with the uncorrelated configurational model [Catanzaro et al. 2005] exhibit an average cluster coefficient that decreases with the system size as $\langle C \rangle \sim N^{2-\lambda}$ for SF networks with $P(k) \sim k^{-\lambda}$. Therefore, the presence of triangular connections in our graphs is negligible for large enough networks.

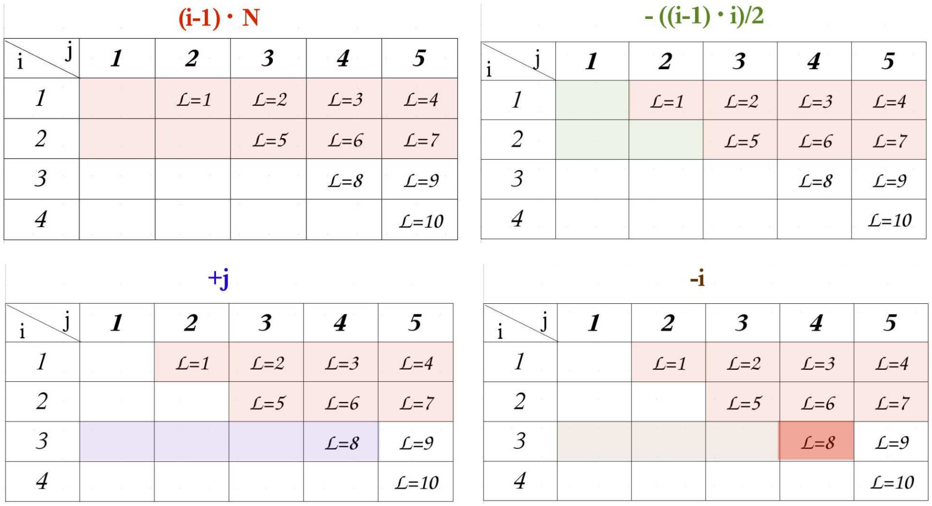

(i-1) · N

i \ j	1	2	3	4	5
1		$\mathcal{L}$=1	$\mathcal{L}$=2	$\mathcal{L}$=3	$\mathcal{L}$=4
2			$\mathcal{L}$=5	$\mathcal{L}$=6	$\mathcal{L}$=7
3				$\mathcal{L}$=8	$\mathcal{L}$=9
4					$\mathcal{L}$=10

- ((i-1) · i)/2

i \ j	1	2	3	4	5
1		$\mathcal{L}$=1	$\mathcal{L}$=2	$\mathcal{L}$=3	$\mathcal{L}$=4
2			$\mathcal{L}$=5	$\mathcal{L}$=6	$\mathcal{L}$=7
3				$\mathcal{L}$=8	$\mathcal{L}$=9
4					$\mathcal{L}$=10

+j

i \ j	1	2	3	4	5
1		$\mathcal{L}$=1	$\mathcal{L}$=2	$\mathcal{L}$=3	$\mathcal{L}$=4
2			$\mathcal{L}$=5	$\mathcal{L}$=6	$\mathcal{L}$=7
3				$\mathcal{L}$=8	$\mathcal{L}$=9
4					$\mathcal{L}$=10

-i

i \ j	1	2	3	4	5
1		$\mathcal{L}$=1	$\mathcal{L}$=2	$\mathcal{L}$=3	$\mathcal{L}$=4
2			$\mathcal{L}$=5	$\mathcal{L}$=6	$\mathcal{L}$=7
3				$\mathcal{L}$=8	$\mathcal{L}$=9
4					$\mathcal{L}$=10

Figure 7.4: Label assignment for path $(i = 3, j = 4)$ in a system of size $N = 5$. There are 10 paths (i, j) labeled $\mathcal{L} = 1, 2, ..., N(N-1)/2$ according to Eq. (7.4). The path $(3, 4)$ has assigned the label $\mathcal{L}(3, 4) = 8$. The panels show the different constributions of Eq. (7.4) to the path label.

To carry out the optimization we repeat, in an iterative way, the following steps:

- The node m with the highest betweenness is selected.
- One of the paths, $\mathcal{L}$, passing through m is chosen at random. $\mathcal{L}$ must not start or finish at m, let us refer to its initial and final nodes as i and j.
- An alternative to $\mathcal{L}$ between i and j is searched trying to keep the distance as short as possible without passing through m. If there is no such alternative, the path remains unchanged.

An schematic illustration of these rules is shown in the panels a) and b) of Fig. 7.5. In the sketch, a path passing through the node with the highest betweenness, represented as an square, is deviated to an alternative route avoiding it. It is worth noting again the usefulness of degenerated paths. The constraint of alternative paths as short as possible means in practice that, if another choice of equal extension exists, the path will never be increased in length. The method takes advantage of the possible degeneracy of the paths in length to reorder the protocol and ease the traffic

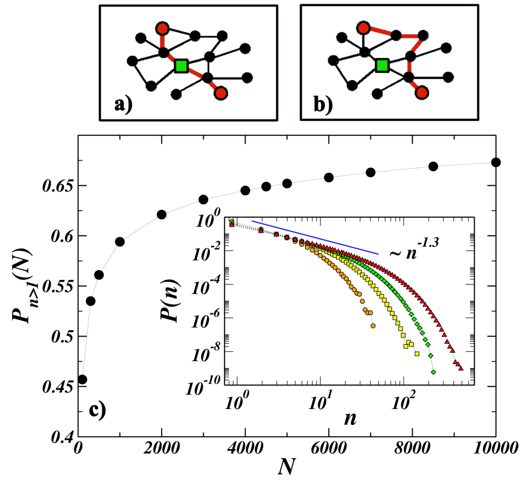

Figure 7.5: The sketches a) and b) illustrate the way in which the method optimizes the protocol by selecting another path that must be either of the same length or the shortest alternative to the original one. In c), the probability of finding alternative length-degenerate paths, $P_{n>1}$, for the SP protocol is displayed as a function of the network size N. In the inset: histogram for the number n of degenerate alternatives for each path in the SP protocol. The different curves correspond to the following network sizes: $N = 10^2$ (circles), 5×10^2 (squares), 2×10^3 (diamonds) and 10^4 (triangles).

passing through the maximal betweenness node. The paths can thus be only one of two possibilities: the SP configuration or the shortest alternative to them.

The important role played by the length degeneracy can be observed in Fig. 7.5c. There, the probability of having n alternative paths for a SP configuration, $P_{n>1}(N)$, is displayed as a function of the size of the network. $P_{n>1}(N)$ consistently grows with N, becoming higher than 65% for the largest graphs that we have considered $N = 10^4$. In the inset, the distribution of the number of degenerated paths, $P(n)$, is also shown for four network sizes. Note that $P_{n>1} = \sum_{n=2}^{\infty} P(n)$.

This considerable presence of degenerated paths gives us the chance to achieve the proposed compromise between minimization of maximal centrality and short distances. In the following, we will study how our extremal optimization algorithm affects the different features of the protocols.

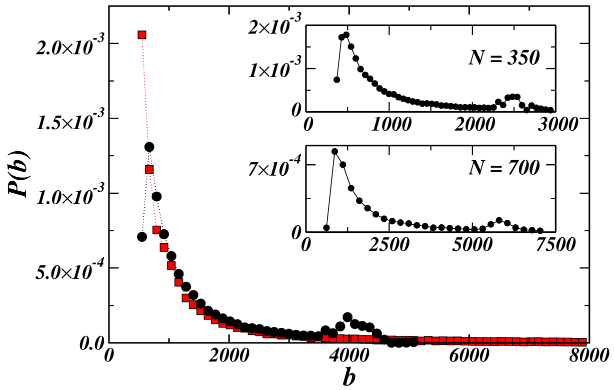

Figure 7.6: Betweenness distribution for a $N = 500$ system. The (black) circles correspond to the stationary distribution reached with our optimization method while the (red) squares are for the initial SP protocol. In the inset, the stationary betweenness distributions of the method for other two network sizes $N = 350$ and $N = 700$.

7.3 Betweenness distribution

In this section, we will discuss the results concerning the betweenness of the nodes and how it behaves after the optimization method is employed. After some iterations of the method the betweenness distribution, $P(b)$, reaches a stationary form that can be seen in Fig. 7.6. The highlight task here is to compare this stationary distribution with the initial SP betweenness distribution. From Ref. [Goh et al. 2001, Barthélemy 2003] we know that the SP protocol produces a power-law of the betweenness distribution $P(b)$ with an exponent that depends on the exponent λ of the degree distribution. This is in agreement with the distribution plotted in Fig. 7.6. We observe that the protocols resulting from our optimization method show the tail of this initial distribution $P(b)$ collapsed into a peak at high values of the betweenness. Also the region of low b suffers a slight variation, although the functional form of $P(b)$ in the intermediate regions seems largely unaffected. A change in the size of the network displaces the position of the peak but not the quality of the effects observed in the main plot of Fig. 7.6.

The peak induced in $P(b)$ by the optimization method at high values of b correlates with a decline of the maximum betweenness in the network. As we have discussed above, this betweenness, B, is crucial for the transport capability of a protocol, since it imposes an upper cutoff to the traffic the network is available to sustain before jamming [Arenas et al. 2001, Ohira and Sawatari 1998, Solé and Valverde 2001]. The scaling of B with the network size, N, can be seen thus as a measure of

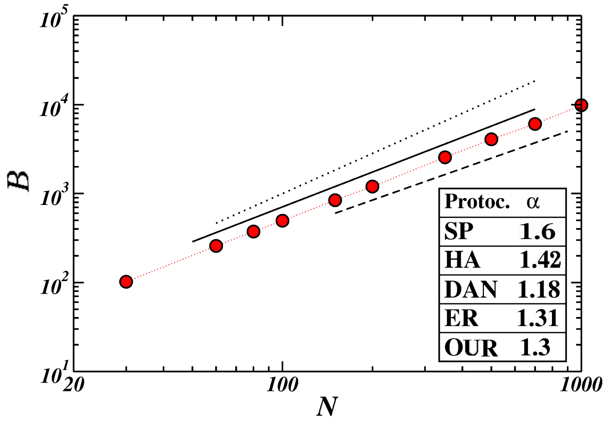

Figure 7.7: The maximum betweenness, B, as a function of the network size N for the optimized protocol (the scale of the axis are in log-log representation). Lines are shown as a reference scaling with exponent 1.3 (solid), 1.2 (dashed), and 1.5 (dotted). In the table, scaling exponents α obtained with different optimization methods are listed. The initials correspond to Shortest-Path (SP) [Danila et al. 2006], Hub-Avoidance (HA) [Sreenivasan et al. 2007], Danila's method (DAN) [Danila et al. 2006], Efficient Routing (ER) [Yan et al. 2006] , and our own method (OUR).

the scalability of a protocol. The faster B grows with N, the less useful the protocol will be for large networks. In Fig. 7.7 we plot the average maximal betweenness in the stationary state of our optimized protocol as a function of the network size. We find a power-law increase with a functional form $B \sim N^{\alpha}$ and $\alpha^{OUR} \approx 1.3$. This value of α must be compared with the results encountered for other protocols or other protocol optimization methods presented in the introduction of the chapter. In the same figure, we have also included a table with the exponents α for other methods. It is specially interesting the comparison with the original SP protocol $\alpha^{SP} \approx 1.6$ or with the best of the optimization methods listed (Danila's method) with $\alpha^{DAN} \approx 1.18$ [Danila et al. 2006]. Our optimization method, without deviating substantially from the SP protocol, as the length of the paths is concerned, produces a very acceptable value of the exponent α.

7.4 Path Length

Although our optimization is mainly based on a minimization of the maximal node betweenness, a compromise between optimization and short-distances is necessary to obtain an efficient routing protocol. A protocol that elongates the paths too much is not useful for network communications. Commonly, there exists a nonzero probability of losing a packet in every communication between two servers. The longer the paths become, the higher is the probability of missing information. This loss can attain a point at which most of the paths are not functioning and the network may suffer from disruptions. On the other hand, longer paths lead to longer "ping" times, with the corresponding delay in processing information.

In this section we will focus on studying how the length of the paths of the protocol changes when the optimization method is applied to the protocol. In Fig. 7.8, we have plotted the path length distribution $P(\ell)$ for the original Shortest Path protocol and for the stationary regime of the protocols obtained with our optimization method on a network of size $N = 10^3$. As can be seen, the center of the distribution has slightly displaced but its shape remains essentially invariant. In order to quantify the displacement of the center of $P(\ell)$ with the system size, we have represented in the panel b) of Fig. 7.8 the ratio between the average length of the paths in our method and that calculated with the SP protocol. The curve is monotonically decreasing with N, and for large systems it moves very slowly toward unity or a value close to it. This means that, as the network becomes larger, the lengths of our paths become closer to shortest-paths.

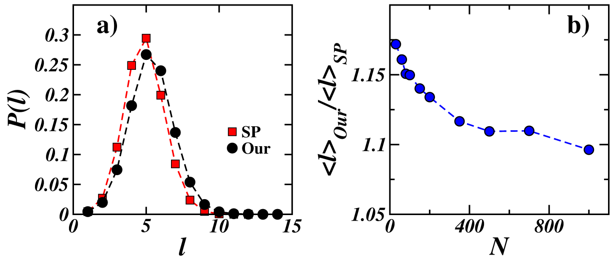

Figure 7.8: In a), paths length distribution for a network of size $N = 1000$. In the figure, the results of the protocols obtained with our optimization method can be compared with the initial SP. In b), the ratio between the average length of the paths in the two protocols (ours and SP) is visualized as a function of the network size.

As occurs with B, the scaling of the average length of the paths, $\langle \ell \rangle$, with the system size is also important. In Figure (7.9), we show how $\langle \ell \rangle$ behaves with increasing network size. In ultra-small scale-free networks with $2 < \lambda < 3$, as the ones we use, the SP protocol $\langle \ell_{SP} \rangle$ is expected to grow as $\log(\log(N))$ [Cohen and Havlin 2003]. We cannot numerically test this formula for many decades in N but within the limited range of values we can explore the relation seems to hold.

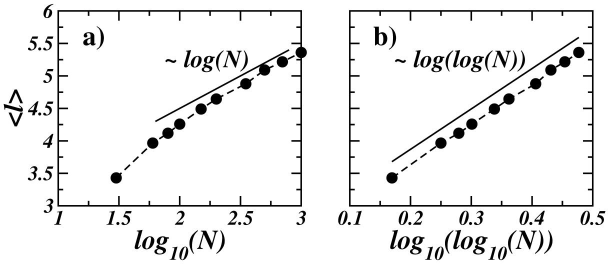

Figure 7.9: The average path length, $\langle l \rangle$, of the protocols we obtain as a function of the network size. It can be seen that the fit b) to a $\log(\log(N))$ functional form approaches better the results from the simulation than a single $\log(N)$ in a).

Finally, as explained above, we underline that the paths of our optimized SRP can be only in two states: either the SP configuration or the shortest alternative to them in the case that the expelled path from the highest betweenness node does not exhibit degeneration. Such a two-state configuration recalls many physical systems in which the components can be in the ground state or being excited by thermal (stochastic) fluctuations and end up in higher energy levels. To confirm such a picture, we have plotted in Fig. 7.10 the cumulative distribution, $C_>(R) = \int_R^\infty dR'\, P(R')$, of the ratios $R = \ell_{stat}/\ell_{SP}$, where ℓ_{stat} corresponds to the length of each path in an stationary configuration of the optimized protocol and ℓ_{SP} is the length of the corresponding path in the initial SP configuration. As can be seen, the probability for the paths to be below a certain excited level R decays rapidly as an exponential function. In the present example, the characteristic ratio of such exponential decay is around 0.55, which makes extremely unlikely for any path to suffer a large stretching out of its SP length. However, we expect that such characteristic ratio may depend on the topology of the network employed; whether it is scale-free or not, and, if it is, also on the exponent of the degree distribution.

7.5 Weighted networks

Up to this point we have considered graphs with indistinguishable links. However, as we mentioned in the previous chapter, for many applications in transport optimization it is useful to consider connections with different qualities. This is something that can be observed in many real communication networks. For instance, in an airline network the quality of the links could represent the cost of the flights in terms of money or time. In the Internet this difference represents the variability of capacities or bandwidths of the links between computers. Mathematically speaking, the quality

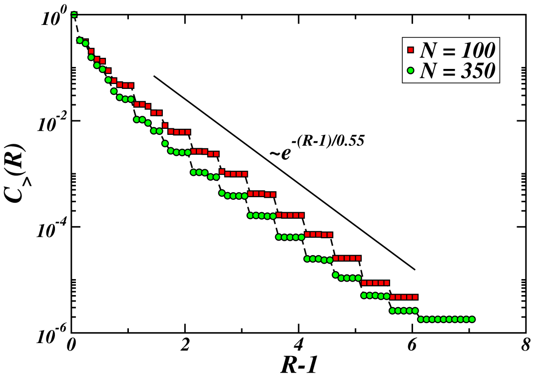

Figure 7.10: Cumulative distribution of the ratio between the longitudes of the paths obtained with our protocol optimization method and the length of the corresponding original SP for scale-free networks $P(k) \sim k^{-2.5}$. The distribution becomes step-like due to the discrete character of the length.

of a connection is represented by a scalar variable attached to each link that is known as weight w. The presence of weighted links alters the definition of distance. The *effective* length of a given path between two nodes is not determined only by the number of links that belong to it, but it is rather given by the sum of the weights of those links. Therefore, to optimize the routing protocol between all the pairs of nodes the concept of short-path has to be reconsidered. Instead of the shortest in the sense of number of links, it may be important to find the path with the lowest weight from source to destination. These paths are often referred to as *optimal paths* in the literature [Porto et al. 1999, Braunstein et al. 2003, Park et al. 2004, Kalisky et al. 2005, Wu et al. 2006].

Protocols based on optimal paths (OP) exhibit a very particular scaling with the network size [Braunstein et al. 2003, Kalisky et al. 2005]. Depending on the level of randomness of the weights of connections, the system can be either strongly or weakly disordered. In the former case, the fluctuations on the weight are so large that the weight along the paths is controlled by the edge with the largest weight, while in the weak disorder case the responsibility is distributed between the links that constitute the path. For SF networks with degree distribution $P(k) \sim k^{-\lambda}$ and $2 < \lambda < 3$ the average length of the optimal paths scales as $\langle \ell_{opt} \rangle \sim \log(N)$ for weak disorder, while a scaling $\langle \ell_{opt} \rangle \sim (\log(N))^{\lambda-1}$ has been proposed for the strong disorder case. However, in both cases and particularly for $2 < \lambda < 3$, the scaling of B with N does not change too much with respect to unweighted graphs [Goh et al. 2001, Barthélemy 2003, Goh et al. 2005]. Here we will focus only on the weak disorder case since it is the only one in which it makes sense to search for an alternative protocol to the OP, the cost of doing so in the strong disorder limit would diverge with the size of the graph.

One of the positive aspects of our protocol optimization is that its generalization for weighted graphs is straightforward: at each step, a path $\mathcal{L}$ passing through the node with highest betweenness is randomly selected to be redirected. Now the alternative path to avoid this node is searched trying to keep the cost as low as possible (such cost is understood as the sum of all the weights along the path since we are in the weak disorder limit). As before, if there is no alternative, the path remains invariant. In the following, we will study the performance of the stationary protocols produced by this method on Reed-Molloy graphs with $\lambda = 2.5$ and with two possible functional forms for the weight distribution: either an exponential $P(w) \sim e^{-w/w_c}$ or a power-law distribution $P(w) \sim w^{-\beta}$. In order to keep the results comparable for both distributions, we fix the parameter w_c to obtain a similar average weight as in the power-law distribution. In the data shown, this will be $w_c = 2$ and $\beta = 2.5$.

The scaling of B as a function of the network size is shown in Fig. 7.11 for both types of weight distributions. The application of the optimization method produces a significant improvement in B with respect to the OP protocol. For the range of system sizes shown in the figure, this means a factor 3 or even higher. Also, the exponent α of the optimized protocols is close to 1.4 while that of the original OP protocols was about 1.56.

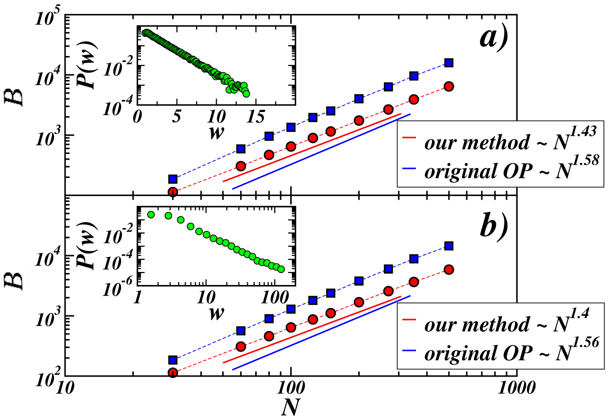

Figure 7.11: Dependence of B with the system size for weighted graphs. The (red) circles are the results for the protocols of our method and the (blue) squares are for the original OP protocol. The weight distribution for a) is an exponential $P(w) \sim e^{-w/2}$, and for b) is the power-law $P(w) \sim w^{-2.5}$, as can be seen in the insets for networks of size $N = 500$.

One can wonder then what is the price to pay for such an improvement. In networks with continuous values of the weights, as the ones we deal with, the degeneracy on the weight of the alternative paths is extremely unlikely. Strictly speaking thus, there is always a price to pay, although it could be a small one. To answer this question, we have plotted in Fig. 7.12 how the average weight of the paths scales with N for protocols obtained with our method and for the corresponding OP. We show these results for both exponential and power-law distributed weights. Similarly to what occurred with the path lengths in the unweighted case, we find that the average weight is slightly higher but not extremely so. Also the ratio between the average weight of the paths of our optimized protocol and that of the initial OP protocol decreases for increasing network sizes and slowly moves toward a value close to one. Furthermore, even though it is not shown in the figure, the shape of the distribution of the weight of the paths remains almost unaltered by the optimization of the protocols.

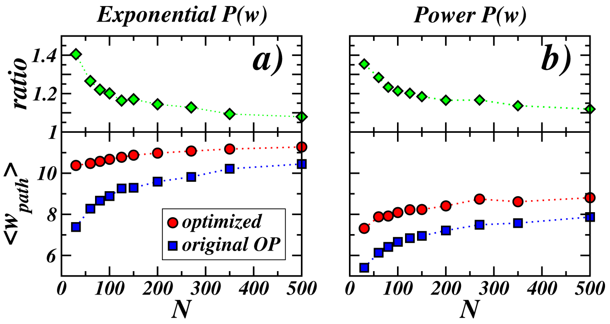

Figure 7.12: Comparison between the average weight of the paths, $\langle w_{path} \rangle$, in the original OP protocol and in the optimized protocols with our method. The curves in a) correspond to weighted graphs with an exponentially decaying weight distribution, while those in b) have a power-law weight distribution.

7.6 Discussion and Conclusion

Traffic flow in networks, and particularly jamming and its dynamical relation to the network structure, has become a topic of intense investigation in the last few years. To outperform the transport capacity of such communicating networks, the routing protocol - which defines the paths between all pairs of nodes - may be optimized in order to avoid congestion.

In this chapter we have introduced our own protocol optimization algorithm that is applicable to both weighted or unweighted graphs. Our aim is not to produce a fast or computational ambitious algorithm to improve protocols but to explore how much a slight variation on the Shortest Path (or Optimal Path) protocol can be compatible with an acceptable improvement of the protocol. The method we propose exploits the paths degeneracy or the close-weight alternatives to minimize the maximal node betweenness, B. If the resulting protocol is considered as the routing table of a traffic model based on packet flow, this would imply a maximization of the packet insertion rate at which jamming occurs. This will immediately increase the amount of information (capacity) that the communication network can handle without jamming.

We observe that the scalability of the SP (or OP) betweenness is significantly improved with our algorithm, while the length (or weight) of the paths remains almost invariant. An iterative application of the algorithm collapses the power law tail of the initial betweenness distribution into a peak, but keeps the length distribution practically unaffected. The power-law dependence of the maximal node betweenness with the system size, $B \sim N^{\alpha}$, is thus improved as compared with the initial SP protocol, $\alpha_{SP} \approx 1.6$, to the stationary optimized protocol, $\alpha_{OUR} \approx 1.3$. This exponent, which can be considered as a measure of the algorithm optimality, is comparable with the method proposed by Danila et al. [2006] for which they obtain $\alpha_{DAN} \approx 1.18$. Danila's method is the best performing protocol, as information capacity is concerned, but does not explicitly take into account the increase of path lengths and the corresponding worsening of the ping times. Our algorithm is optimal in the sense that it performes very well by producing a slow growth of the maximal betweenness, while the routing paths are kept as close as possible from the initial SP (or OP) protocol. This strongly suggests that our algorithm may be the best option for some practical applications.

APPENDIX

A Mean-field approach of the Sznajd model

In this appendix we detail the calculations of the analysis provided in Sec. 5.1.1. We consider the simplified "two over one" version of the Sznajd model, in which two randomly taken agents are able, if they are in consensus, to convince another randomly chosen agent. The system consists of N individuals where N^+ and N^- are the number of agents supporting the $(+)$ and the $(-)$ position, respectively (with $N^+ + N^- = N$). In terms of the total magnetization of the system, $m = (N^+ + N^-)/N$, the number of agents reads $N^\pm = N(1 \pm m)/2$.

The master equation is a gain-loss equation for the probability of the system to have magnetization m, which reads

$$\frac{\partial P(m,t)}{\partial t} = \int [W(m|m')P(m',t) - W(m'|m)P(m,t)]dm' \qquad \text{(A.1)}$$

where $W(m|m')$ is the transition probability per unit time from m' to m (and viceversa).

In our model a pair of agents is chosen at random at each time step, and depending on their agreement they are able to convince a third one. Thus the probability of having (N^+, N^-) agents at time t includes all the possible contributions

$$\begin{aligned} P(N^+, N^-, t) &= Q_A(N^+ - 1, N^- + 1 \to N^+, N^-)P(N^+ - 1, N^- + 1, t-1) + \\ &+ Q_B(N^+ + 1, N^- - 1 \to N^+, N^-)P(N^+ + 1, N^- - 1, t-1) + \\ &+ Q_C(N^+, N^- \to N^+, N^-)P(N^+, N^-, t-1) \,, \end{aligned} \tag{A.2}$$

where the transition probabilities, Q, depend on the probability of choosing each agent with $(+)$ or $(-)$ opinion

$$\begin{aligned} Q_A &= \Big(\frac{N^+ - 1}{N}\Big) \cdot \Big(\frac{N^+ - 2}{N - 1}\Big) \cdot \Big(\frac{N^- + 1}{N - 3}\Big) = [+ + -] \\ Q_B &= \Big(\frac{N^- - 1}{N}\Big) \cdot \Big(\frac{N^- - 2}{N - 1}\Big) \cdot \Big(\frac{N^+ + 1}{N - 3}\Big) = [- - +] \\ Q_C &= [+ + +] + [+ - +] + [+ - -] + [- + +] + [- + -] + [- - -] \,. \end{aligned} \tag{A.3}$$

In the thermodynamic limit $N \gg 1$ such quantities can be approached (in terms of the magnetization m) as

$$\begin{aligned} Q_A(m - \frac{2}{N} \to m) &= \frac{1}{8}\Big[1 - \Big(m - \frac{2}{N}\Big)^2\Big]\Big[1 + \Big(m - \frac{2}{N}\Big)\Big] \\ Q_B = (m + \frac{2}{N} \to m) &= \frac{1}{8}\Big[1 - \Big(m + \frac{2}{N}\Big)^2\Big]\Big[1 - \Big(m + \frac{2}{N}\Big)\Big] \\ Q_C = (m \to m) &= 1 - Q_A - Q_B = 1 - \frac{1}{4}(1 - m^2) \,. \end{aligned} \tag{A.4}$$

yielding the master equation

$$\begin{aligned} P(m, t) &= Q_A(m - \frac{2}{N} \to m)\; P\Big(m - \frac{2}{N}, t - 1\Big) + \\ &+ Q_B(m + \frac{2}{N} \to m)\; P\Big(m + \frac{2}{N}, t - 1\Big) + \\ &+ Q_C(m \to m)\; P\Big(m, t - 1\Big) \,. \end{aligned} \tag{A.5}$$

In order to properly achieve the continuous limit ($\frac{1}{N} \ll 1$) we expand $P(m \pm \frac{2}{N})$ and $Q(m \pm \frac{2}{N} \to m)$ around m up to the second order in $(1/N)$:

$$\begin{aligned} P(m \pm \frac{2}{N}, t) &\approx P(m, t) \pm \frac{2}{N}\frac{\partial}{\partial m}P(m, t) + \frac{1}{2}\Big(\frac{2}{N}\Big)^2 \frac{\partial^2}{\partial m^2}P(m, t) + O\Big(\frac{1}{N^3}\Big) \\ Q_A(m - \frac{2}{N} \to m) &\approx \frac{1}{8}(1 - m^2)(1 + m) - \frac{2}{N}\frac{1}{8}[1 - 2m - 3m^2] - \frac{1}{8}\Big(\frac{2}{N}\Big)^2(1 + 3m) + O\Big(\frac{1}{N^3}\Big) \\ Q_B(m + \frac{2}{N} \to m) &\approx \frac{1}{8}(1 - m^2)(1 - m) - \frac{2}{N}\frac{1}{8}[1 + 2m - 3m^2] - \frac{1}{8}\Big(\frac{2}{N}\Big)^2(1 - 3m) + O\Big(\frac{1}{N^3}\Big) \end{aligned} \tag{A.6}$$

Then, rescaling the time as $t = 2N\tau$ we finally obtain the FPE up to second order in $(1/N)$ [*cf.* Eq. (5.1)]

$$\frac{\partial}{\partial\tau}P(m,\tau) = - \frac{\partial}{\partial m}\Big[m(1-m^2)P(m,\tau)\Big] + \left(\frac{1}{2N}\right)\frac{\partial^2}{\partial m^2}\Big[(1-m^2)P(m,\tau)\Big] \,. \tag{A.7}$$

Now we include the effect of the social temperature by introducing some probability $(1-p)$ that the procedural rules of the model are not fulfilled (with the agent to be updated adopting the opposite opinion that the one assigned by the rules).

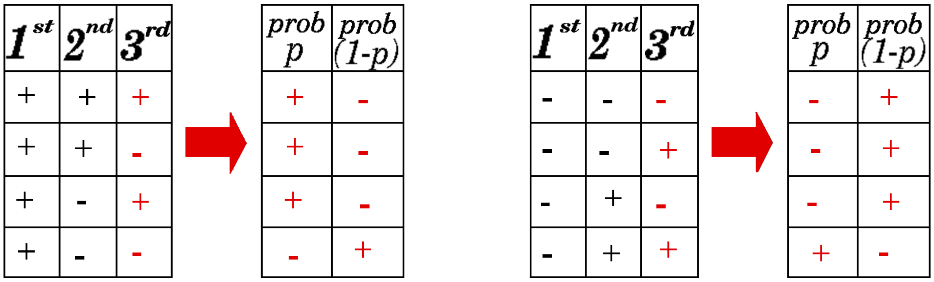

1st	2nd	3rd	prob p	prob (1-p)
+	+	+	+	-
+	+	-	+	-
+	-	+	+	-
+	-	-	-	+

1st	2nd	3rd	prob p	prob (1-p)
-	-	-	-	+
-	-	+	-	+
-	+	-	-	+
-	+	+	+	-

Figure A.1: The model rules read that the pair of chosen agents are able to convince the third one if they are in agreement between themselves, and otherwise nothing happens. This scheme shows all the possible choices when the possibility of not fulfilling such rules is considered with probability $(1-p)$.

Thus the contributions that need to be taken into account in the master equation are

$$Q_A\left(m-\frac{2}{N}\to m\right) = \frac{p}{8}\Big[1+\Big(m-\frac{2}{N}\Big)\Big]^2\Big[1-\Big(m-\frac{2}{N}\Big)\Big] + \frac{(1-p)}{4}\Big[1+\Big(m-\frac{2}{N}\Big)\Big]\Big[1-\Big(m-\frac{2}{N}\Big)\Big]^2 + \frac{(1-p)}{8}\Big[1-\Big(m-\frac{2}{N}\Big)\Big]^3 \tag{A.8}$$

$$Q_B\left(m+\frac{2}{N}\to m\right) = \frac{p}{8}\Big[1-\Big(m+\frac{2}{N}\Big)\Big]^2\Big[1+\Big(m+\frac{2}{N}\Big)\Big] + \frac{(1-p)}{4}\Big[1-\Big(m+\frac{2}{N}\Big)\Big]\Big[1+\Big(m+\frac{2}{N}\Big)\Big]^2 + \frac{(1-p)}{8}\Big[1+\Big(m+\frac{2}{N}\Big)\Big]^3 \tag{A.9}$$

and

$$Q_C(m\to m) = 1 - Q_A - Q_B \,. \tag{A.10}$$

We again expand these functions around $(m \pm \frac{2}{N}) \approx m$ up to the second order in $(1/N)$ to approach the continuous limit $(\frac{1}{N} \ll 1)$. In this case, the general formulation of the master equation given in Eq. (A.5) yields the FPE in presence of contrarians [*cf.* Eq. (5.2)]

$$\begin{aligned}\frac{\partial}{\partial \tau} P_p(m,\tau) = & - \frac{\partial}{\partial m}\Big\{\Big[(6p-5)m-(2p-1)m^3\Big]P_p(m,\tau)\Big\} \\ & + \left(\frac{1}{2N}\right)\frac{\partial^2}{\partial m^2}\Big\{\Big[3-2p-(2p-1)m^2\Big]P_p(m,\tau)\Big\}, \qquad \text{(A.11)}\end{aligned}$$

where time has been again rescaled as $t = 2N\tau$.

Upon reaching this point, we can obtain from Eq. (A.11) the stationary probability distribution function (PDF) for the system to have magnetization m. The Fokker-Planck equation, which has a general form $\frac{\partial P}{\partial t} = -\frac{\partial}{\partial m}[A(m)P(m,t)] + \frac{1}{2}\frac{\partial^2}{\partial m^2}[B(m)P(m,t)]$, can be broken up in a continuity equation for the probability density

$$\frac{\partial P(m,t)}{\partial t} + \frac{\partial}{\partial m} J(m,t) = 0 \; , \qquad \text{(A.12)}$$

with the current $J(m,t) = A(m)P(m,t) - \frac{1}{2}\frac{\partial}{\partial m}[B(m)P(m,t)]$.

The PDF is given by $\partial P_{stat}/\partial t = 0$ that implies $\frac{\partial J(m,t)}{\partial m} = 0$, and particularly $J(m,t) = 0$. This implies

$$\left[A(m) - \frac{1}{2}\frac{\partial B(m)}{\partial m}\right]\left[\frac{1}{2}B(m)\right]^{-1} = \frac{\partial P_{stat}(m)/\partial m}{P_{stat}(m)} \; . \qquad \text{(A.13)}$$

Integrating such an expression and taking the exponential form we arrive at

$$P_{stat}(m) \approx \exp\left\{\int_{-1}^{m} \frac{2A(m')}{B(m')} dm' - \ln B(m)\right\} \qquad \text{(A.14)}$$

In our case, we extract from Eq. (A.11) the following terms for the current

$$\begin{aligned} A(m) &= [(6p-5)m-(2p-1)m^3] \\ B(m) &= N^{-1}[3-2p-(2p-1)m^2] \qquad \text{(A.15)}\end{aligned}$$

that yields

$$P_p^{stat}(m) \approx \exp\left\{2N\int_{-1}^{m} \frac{(6p-5)u(2p-1)u^3}{3-2p-(2p-1)u^2}\, du + \ln\left[\frac{N}{3-2p-(2p-1)m^2}\right]\right\} . \qquad \text{(A.16)}$$

This PDF can be expressed in terms of an effective potential as $P_p^{stat}(m) \approx e^{-V_{eff}}$. In order to analyze the stability of such stationary solution for varying p, we consider the condition $\frac{\partial V_{eff}}{\partial m} = 0$ to obtain the potential minima

$$\frac{\partial V_{eff}}{\partial m} \approx \frac{(6p-5)m-(2p-1)m^3}{3-2p-(2p-1)m^2} = 0 \text{ , which implies} \left\{ \begin{array}{l} m = 0 \\ m_{\pm} = \pm\sqrt{\frac{6p-5}{2p-1}} \text{ ,} \end{array} \right. \tag{A.17}$$

in doing so the second term in V_{eff} has been not considered as it increases slower than the former one with the system size N, and can be neglected.

APPENDIX

B

Publications list

(1) de la Lama, M. S., López, J. M., and Wio, H. S. (2005). Spontaneous emergence of contrarian-like behaviour in an opinion spreading model. *Europhys. Lett.* 72 : 851-857

(2) Wio, H. S., de la Lama, M. S., and López, J. M. (2006). Contrarian-like behaviour and system size stochastic resonance in an opinion spreading model. *Physica A* 371 : 108-111

(3) de la Lama, M. S., Szendro, I. G., Iglesias, J. R., and Wio, H. S. (2006). Van Kampen's expansion approach in an opinion formation model. *Eur. Phys. J. B,* 51 : 435-442 [Erratum. *ibid.* 58:221 (2007)]

(4) de la Lama, M. S., López, J. M., Ramasco, J. J., and Rodríguez, M. A. *(submitted to J. Stat. Mech.)*. Activity statistics of a forced elastic string in a disordered medium.

(5) de la Lama, M. S., Ramasco, J. J., López, E., and Boettcher, S. *(to be submitted to Phys. Rev. E)*. Optimization of transport protocols on random networks with path length constraints.

APPENDIX

C

List of Abbreviations

DPRM	-	Directed Polymer in Random Media
DPD	-	Directed Percolation Depinning
ER	-	Erdös-Rényi graph
EW	-	Edwards-Wilkinson universality class
FPE	-	Fokker-Planck Equation
FRG	-	Functional Renormalization Group
KPZ	-	Kardar-Parisi-Zhang universality class
mct	-	Monte-Carlo time
OP	-	Optimal-Path
PDF	-	Probability Distribution Function
QEW	-	Quenched Edwards-Wilkinson universality class
QKPZ	-	Quenched Kardar-Parisi-Zhang universality class
RB	-	Random-Bond disorder
RF	-	Random-Field disorder
RG	-	Renormalization Group Theory
SF	-	Scale-Free network
SP	-	Shortest-Path
SRP	-	Static Routing Protocol
VM	-	Voter Model

APPENDIX

D

Resumen en Castellano

Uno de los aspectos más fascinantes del mundo que nos rodea es la gran variedad de escalas a las que tienen lugar los diversos fenómenos. En muchos casos esta diversidad pone de manifiesto la estructura *fractal* de la Naturaleza y podemos hablar entonces de *fenómenos complejos*, en los que eventos de diferentes magnitudes no pueden analizarse de manera independiente. Dicha complejidad emerge como un fenómeno cooperativo a escalas microscópicas, que produce un complejo comportamiento macroscópico caracterizado por correlaciones de largo alcance e invarianza de escala. Aparecen así conceptos como *leyes de escalado*, *universalidad* y *renormalización*, pilares fundamentales dentro de la *Física Estadística*.

El abanico de fenómenos complejos es muy amplio, y abarca sistemas de muy diversas disciplinas que van desde la Física más "ortodoxa" hasta la Biología, Sociología, Geología e, incluso, Economía. Esta Tesis se centra en fenómenos complejos extendidos en el espacio. En concreto hemos focalizado nuestra labor en tres grandes temas que constituyen importantes focos de interés dentro de la Mecánica Estadística: *Crecimiento de Interfases*, *Sociofísica* y *Redes Complejas*. A continuación presentamos la estructura de la Tesis, que se ha dividido en tres partes independientes correspondiendo con los temas previamente señalados.

La primera parte se centra en Dinámica de Interfases. A modo de introducción, en el Capítulo 2 se definen los conceptos de *fractal* y *escalado dinámico*. Se describen las magnitudes básicas empleadas en la caracterización del crecimiento interfacial así como los distintos tipos de escalado definidos en la literatura [Ramasco et al. 2000]. Asimismo, se introducen las principales clases de universalidad con desorden térmico, conocidas como EW [Edwards and Wilkinson 1982] y KPZ [Kardar et al. 1986], describiendo sus correspondientes ecuaciones de crecimiento así como algunos modelos discretos.

En el Capítulo 3 particularizamos al crecimiento de interfases elásticas en presencia de desorden congelado o *quenched disorder*. Dicha particularización es de gran interés, ya que describe fenómenos tan diversos como la dinámica de los vórtices de campo magnético en un superconductor de tipo-II [Blatter et al. 1994] o el corrimiento de dominios magnéticos en un ferromagneto [Lemerle et al. 1998, Repain et al. 2004]. En la primera parte del capítulo introducimos al lector en este tipo de fenómenos en los que el desorden sólo depende de la posición de la interfase. Atendiendo a su correlación espacial dicho desorden puede ser de corto alcance (*random bond*) o largo alcance (*random field*). Además, atendiendo a la fuerza de empuje, f, y la temperatura, T, la interfase elástica describe diferentes regímenes estacionarios: *estática* o *equilibrio* ($f = 0$), *depinning* ($T = 0$ y $f = f_c$) y *creep* ($f \ll f_c$ y $T \gtrsim 0$).

En la segunda parte de este capítulo analizamos la relajación hacia el estado estacionario de una interfase unidimensional forzada en presencia de desorden de tipo random-field y fluctuaciones térmicas. La dinámica de relajación de la interfase elástica ya ha sido previamente abordada desde el punto de vista teórico empleando aproximaciones de Campo Medio y Grupo de Renormalización [Ioffe and Vinokur 1987, Nattermann 1987, Vinokur et al. 1996, Cugliandolo et al. 1996, Chauve et al. 2000, Balents and Le Doussal 2004, Schehr and Le Doussal 2004]. Sin embargo, la aplicación de estos resultados a sistemas de bajas dimensiones es difícil y, especialmente en lo que concierne a observaciones experimentales, análisis numéricos puede ser de gran utilidad [Schehr and Le Doussal 2004; 2005, Rosso and Krauth 2002, Kolton et al. 2005b; 2006]. Nosotros consideramos la condición ($f \ll f_c$) y observamos, mediante simulaciones de un modelo de autómata celular inspirado en [Leschhorn 1993], cómo el sistema relaja en los distintos rangos de temperatura. La discretitud de nuestro modelo nos permite construir patrones espacio-temporales de la actividad en los distintos puntos de la interfase y llevar a cabo un novedoso análisis de las correlaciones de los mismos a partir de las distribuciones de intervalos temporales y espaciales entre puntos activos. Relacionamos, además, estas variables locales con variables globales de la dinámica como la velocidad de la interfase y sus correlaciones. Observamos tres regímenes de relajación diferenciados atendiendo a la intensidad de las fluctuaciones térmicas. A altas temperaturas dichas fluctuaciones dominan sobre el desorden (clase de universalidad EW) y las distribuciones de intervalos espacio-temporales entre eventos o puntos activos describen decaimientos exponenciales. A bajas temperaturas encontramos un régimen cuya dinámica puede describirse mediante los argumentos teóricos del creep. La interfase describe largos periodos de inactividad, correspondientes a estados metaestables o "quasi-pinned", seguidos de activaciones térmicas sobre las barreras de energía del equilibrio que producen avances coherentes a las escalas equilibradas de la misma. Acorde a esta descripción, observamos distribuciones potenciales de los intervalos espacio-temporales entre eventos. Sin embargo, a ultrabajas temperaturas observamos que los argumentos de la dinámica de creep no son aplicables debido a la relevancia que adquiere la asimetría de nuestra interfase forzada. Terminamos el capítulo con la inclusión en las simulaciones de correcciones no-lineales al orden más bajo.

La segunda parte de la Tesis versa sobre Sociofísica. Esta disciplina analiza, desde la Física de los Sistemas Complejos, diversos fenómenos sociales colectivos como la formación de opinión, propagación de tendencias culturales, cooperación entre grupos de individuos o evolución de los mercados. Sin pretender reproducir la realidad de una Sociedad difícilmente reproducible, este nuevo campo de la Mecánica Estadística analiza los patrones globales y autoorganizados que emergen del comportamiento "microscópico" de los individuos que la constituyen, y lo hace mediante simulaciones de modelos basados en agentes (ABM) y cálculo de ecuaciones maestras o de balance. En este trabajo nos centramos en fenómenos de formación de opinión. En el Capítulo 4 introducimos los diversos tipos de modelos de opinión presentes en la literatura, entre los que destacamos principalmente cuatro tipos: modelo del votante [Ben-Naim et al. 1996, Dornic et al. 2001, Krapivsky and Redner 2003], modelos de impacto social (modelo de Sznajd [2000]), modelos basados en la mayoría (modelo de Galam [1990]) y modelos contínuos (modelo de Deffuant et al. [2000]). En el Capítulo 5 presentamos dos trabajos en los que analizamos cómo la *temperatura social*, entendida como un parámetro de agitación colectiva fruto de la interacción de cada individuo con su entorno, puede afectar a los procesos de formación de opinión. En el primero de ellos consideramos un ABM de tipo Ising que reproduce la dinámica de Sznajd. Realizamos simulaciones en distintos tipos de redes (unidimensional, completamente conectada y de pequeño mundo), considerando el efecto de la temperatura social como una cierta probabilidad de que los individuos actúen de forma opuesta a las reglas establecidas del modelo. Observamos que dicho mecanismo introduce de forma dinámica un efecto tipo "contrarian", que pueden definirse como agentes que ejercen oposición constante a la mayoría [Galam 2004]. Observamos cierta temperatura crítica por encima de la cual el sistema, debido al efecto de dicha oposición constante, no es capaz de alcanzar un estado final de consenso. Corroboramos estos resultados numéricos mediante calculos analíticos de la ecuación maestra y de Fokker-Planck, que nos permite aproximar la distribución estacionaria de la magnetización del sistema para el caso de Campo Medio (equivalente al caso discreto de la red completamente conectada).

En la segunda parte de este capítulo consideramos otro ABM en el que el efecto de la temperatura se entiende como cierta probabilidad de que los agentes sufran cambios espontáneos de opinión. El modelo consiste en dos grupos de agentes con opiniones definidas, N_A y N_B, que sólo interaccionan con un tercer grupo de indecisos, N_I (de modo que el número total de agentes $N = N_A + N_B + N_I$). Debido a la posibilidad de cambios espontáneos, todos los grupos son estadísticamente estables y el sistema tiende hacia una única solución estacionaria, lo cual nos permite aplicar la aproximación de van Kampen [van Kampen 1981] en torno al número total de agentes, N. Partiendo de la ecuación maestra del sistema obtenemos las ecuaciones macroscópicas para la densidad de los distintos tipos de agentes, así como la ecuación de Fokker-Planck que describe las fluctuaciones en torno a la solución macroscópica. A partir de ellas analizamos los tiempos de relajación del sistema ante perturbaciones de la solución estacionaria y la variación de la dinámica ante modificaciones de los distintos parámetros que definen las interacciones entre agentes. Observamos interesantes fenómenos de reentrancia, en los cuales la dispersión de la PDF se invierte durante la evolución hacia el estado estacionario. Dicho efecto evidencia la necesidad de interpretar con precaución las encuestas realizadas a lo largo de, por ejemplo, un hipotético proceso electoral.

La tercera y última parte de la Tesis se ubica dentro del marco de las Redes Complejas. Esta reciente y activa disciplina de la Física Estadística estudia diversos sistemas que pueden ser representados mediante gráficas o redes, es decir, como un conjunto de *nodos* conectados mediante enlaces o *links*. Constituyen claros ejemplos Internet, redes neuronales o metabólicas, redes sociales, etc. En el Capítulo 6 proporcionamos una introducción al tema, en la que describimos el concepto de redes libres de escala o *scale-free*, los patrones de *asortatividad* y coeficiente de *clustering*, así como el fenómeno de pequeño mundo o *small-world*. En la última sección del capítulo hacemos una breve introducción a los distintos tipos de procesos que se pueden simular sobre redes complejas, para pasar a centrarnos en procesos de transporte en el siguiente capítulo.

En este último Capítulo 7, definimos un modelo general de transporte basado en la distribución de paquetes de información a través de caminos definidos entre los pares de nodos de la red (cuyo conjunto se denomina comúnmente “protocolo de enrutamiento”). En concreto nos centramos en el problema de optimización de dicho protocolo, entendiendo como tal la cantidad de información que el sistema es capaz de soportar antes de colapsar y atascarse (fenómeno de *jamming*). Esta optimización puede entenderse en términos de la minimización de la máxima centralidad o *betweenness*, esto es, del número de caminos que atraviesan el nodo más visitado, que en redes scale-free escala con el tamaño del sistema como $B \sim N^{1+\varepsilon}$. Tradicionalmente el protocolo definido mediante los caminos más cortos entre pares de nodos (*shortest-paths*) ha sido comúnmente empleado como protocolo óptimo. Sin embargo, varios estudios evidencian la falibilidad de dicho protocolo y presentan otros algoritmos para la optimización de protocolos de enrutamiento [Yan et al. 2006, Sreenivasan et al. 2007, Danila et al. 2006]. Continuando en esta línea de trabajo, nosotros proponemos un algoritmo basado en optimización extremal [Boettcher and Percus 2001] que, partiendo del protocolo *shortest-paths*, minimiza la betweeness máxima manteniendo los caminos entre nodos lo más cortos posible, esto es, en torno a la distibución de distancias internodales del protocolo inicial. A lo largo del capítulo analizamos las propiedades del protocolo estacionario que resulta al aplicar nuestro algoritmo en redes scale-free, con distribución de grados $P(k) \sim k^{-\lambda}$ y típicamente $\lambda = 2.5$. Observamos que, efectivamente, la cola de la distribución inicial de betweenness se concentra en un pico a valores moderados, mientras que la distribución de distancias apenas varía con respecto a la inicial. Esto hace que el escalado de la betweennes máxima, inicialmente $B_{SP}(\lambda = 2.5) \sim N^{1.6}$, se optimice hasta $B_{OUR}(\lambda = 2.5) \sim N^{1.3}$. Este resultado es comparable con el obtenido mediante el algoritmo presentado por Danila et al. [2006], en el que la minimización de la betweenness máxima está mejor lograda, $B_{DAN}(\lambda = 2.5) \sim N^{1.2}$, pero no se añade explícitamente la restricción de mínimas distancias. Los resultados mencionados hasta el momento se refieren únicamente a redes con links indistinguibles. En la última sección del capítulo aplicamos también el algoritmo en redes con pesos, es decir, redes cuyos links se caracterizan individualmente mediante un valor o *peso* acorde a una distribución dada. En este caso el concepto de *shortest-path* torna a *optimal-path*, el camino entre dos nodos cuyo peso total es el mínimo posible. Analizamos los resultados para el caso de desorden débil, en la que la dispersión de los pesos es pequeña y el peso total de los caminos no está dominado por un único enlace. Consideramos dos tipos de distribuciones de pesos diferentes: exponencial y potencial. En ambos casos observamos de nuevo una disminución de la betweennes máxima respecto al protocolo inicial de *optimal-path*, mientras que la razón entre el peso medio de los caminos inicial y final tiende a la unidad según aumenta el tamaño del sistema.

Bibliography

Complex Systems (Introduction)

Albert, R. and Barabási, A.-L. (2002). Statistical mechanics of complex networks. *Rev. Mod. Phys.*, 74:47.

Anderson, P. (1972). More is different. *Science*, 177:393.

Barabási, A.-L. and Stanley, H. (1995). *Fractal Concepts in Surface Growth*. Cambridge University Press, Cambridge.

Bornholdt, S. and Schuster, H. G., editors (2003). *Handbook of Graphs and Nertworks*. Willey-VCH.

Castellano, C., Fortunato, S., and Loretto, V. (2007). Statistical physics of social dynamics. *arXiv:0710.3256v1 [physics.soc-ph].*

Domb, C. and Hunter, D. L. (1965). On critical behaviour of ferromagnets. *Proc. Phys. Soc.*, 86:1147.

Fama, E. F. (1970). Efficient capital markets: A review of theory and empirical work. *Journal of Finance*, 25:383.

Fisher, M. E. (1974). The renormalization group in the theory of critical phenomena. *Rev. Mod. Phys.*, 46:597–616.

Gutenberg, B. and Richter, C. F. (1944). Frequency of earthquakes in California. *Bull. Seismol. Soc. Am.*, 34:185.

Guzzo, L., Iovino, A., Chincarini, G., Giovanelli, R., and Haynes, M. P. (1991). Scale-invariant clustering in the large-scale distribution of galaxies. *Astrophys. Journal*, 382:L5–L9.

Kadanoff, L. P., Götze, W., Hamblen, D., Hecht, R., Lewis, E. A. S., Palciauskas, V. V., Rayl, M., Swift, J., Aspnes, D., and Kane, J. (1967). Static phenomena near critical points: Theory and experiment. *Rev. Mod. Phys.*, 39(2):395–431.

Labini, F. S., Gabrielli, A., Montuori, M., and Pietronero, L. (1996). Finite size effects on the galaxy number counts: Evidence for fractal behavior up to the deepest scale. *Physica A*, 226:195.

Liu, Y., Gopikrishnan, P., Cizeau, P., Meyer, M., Peng, C.-K., and Stanley, H. E. (1999). Statistical properties of the volatility of price fluctuations. *Phys. Rev. E*, 60(2):1390–1400.

Lux, T. and Marchesi, M. (1999). Scaling and criticality in a stochastic multi-agent model of a financial market. *Nature*, 397:498.

Martínez, V. J. and Coles, P. (1994). Correlations and scaling in the qdot redshift survey. *Astrophys. Journal*, 437:550.

Newman, M. E. J. (2003). The structure and function of complex networks. *SIAM Review*, 45:167.

Pietronero, L. (2008). Complexity ideas from condensed matter and statistical physics. *Europhys. News*, 39:26.

Pietronero, L. and Labini, F. S. (2004). Statistical physics for complex cosmic structures. *Adv. in Solid State Phys.*, 44:375.

Pigolotti, S., Flammini, A., Marsili, M., and Maritan, A. (2005). Species lifetime distribution for simple models of ecologies. *PNAS*, 102:15747.

Scaramella, R., Guzzo, L., Zamorani, G., Zucca, E., Balkowski, C., Blanchard, A., Cappi, A., Cayatte, V., Chincarini, G., Collins, C., Fiorani, A., Maccagni, D., MacGillivray, H., Maurogordato, S., Merighi, R., Mignoli, M., Proust, D., Ramella, M., Stirpe, G. M., and Vettolani, G. (1998). The eso slice project [esp] galaxy redshift survey - v. evidence for a $d = 3$ sample dimensionality. *Astron. Astrophys.*, 334:404.

Sneppen, K., Bak, P., Flyvbjerg, H., and Jensen, M. H. (1995). Evolution as a self-organized critical phenomenon. *Proc. Natl. Acad. Sci. USA*, 92:5209.

Stanley, H. (1971). *Introduction to Phase Transitions and Critical Phenomena*. Oxford University, New York.

Stanley, H. R., Amaral, L., Buldyrev, S., Havlin, S., Leschhorn, H., Maass, P., Salinger, M. A., and Stanley, H. E. (1996). Scaling behaviour in the growth of companies. *Nature*, 379:804.

Takayasu, M. and Takayasu, H. (2003). Self-modulation processes and resulting generic 1/f fluctuations. *Physica A*, 324:101.

Vicsek, T. (1989). *Fractal Growth Phenomena*. World Scientific, Singapore and New Jersey.

Widom, B. (1965). Surface tension and molecular correlations near critical point. *J. Chem. Phys.*, 43:3892.

Wilson, K. G. and Kogut, J. (1974). The renormalization group and the ε expansion. *Phys. Rep*, 12:75.

Interface Growth (Part I)

Amar, J. G. and Family, F. (1990). Numerical solution of a continuum equation for interface growth in 2+1 dimensions. *Phys. Rev. A*, 41(6):3399–3402.

Amaral, L. A. N., Barabási, A.-L., Buldyrev, S. V., Harrington, S. T., Havlin, S., Sadr-Lahijany, R., and Stanley, H. E. (1995). Avalanches and the directed percolation depinning model: Experiments, simulations, and theory. *Phys. Rev. E*, 51(5):4655–4673.

Amaral, L. A. N., Barabási, A.-L., and Stanley, H. E. (1994). Universality classes for interface growth with quenched disorder. *Phys. Rev. Lett.*, 73(1):62–65.

Baiod, R., Kessler, D., Ramanlal, P., Sander, L., and Savit, R. (1988). Dynamical scaling of the surface of finite-density ballistic aggregation. *Phys. Rev. A*, 38(7):3672–3679.

Balents, L. and Le Doussal, P. (2004). Broad relaxation spectrum and the field theory of glassy dynamics for pinned elastic systems. *Phys. Rev. E*, 69(6):061107.

Ballestad, A., Ruck, B. J., Adamcyk, M., Pinnington, T., and Tiedje, T. (2001). Evidence from the surface morphology for nonlinear growth of epitaxial gaas films. *Phys. Rev. Lett.*, 86(11):2377–2380.

Barabási, A.-L. and Stanley, H. (1995). *Fractal Concepts in Surface Growth.* Cambridge University Press, Cambridge.

Blatter, G., Feigel'man, M. V., Geshkenbein, V. B., Larkin, A. I., and Vinokur, V. M. (1994). Vortices in high-temperature superconductors. *Rev. Mod. Phys.*, 66(4):1125–1388.

Bruinsma, R. and Aeppli, G. (1984). Interface motion and nonequilibrium properties of the random-field ising model. *Phys. Rev. Lett.*, 52(17):1547–1550.

Buldyrev, S. V., Barabási, A.-L., Caserta, F., Havlin, S., Stanley, H. E., and Vicsek, T. (1992). Anomalous interface roughening in porous media: Experiment and model. *Phys. Rev. A*, 45(12):R8313–R8316.

Canet, L. and Moore, M. (2007). Universality classes of the kardar-parisi-zhang equation. *Phys. Rev. Lett.*, 98:200602.

Castellano, C., Marsili, M., and Pietronero, L. (1998). Nonperturbative renormalization of the kardar-parisi-zhang growth dynamics. *Phys. Rev. Lett.*, 80(16):3527–3530.

Cates, M. E. and Ball, R. C. (1988). Statistics of a polymer in a random potential, with implications for a nonlinear interfacial growth model. *J. Phys. France*, 49:2009–2018.

Chakrabarti, A. and Toral, R. (1989). Numerical study of a model for interface growth. *Phys. Rev. B*, 40(16):11419–11421.

Chauve, P., Giamarchi, T., and Le Doussal, P. (2000). Creep and depinning in disordered media. *Phys. Rev. B*, 62(10):6241–6267.

Cohen, L. F. and Jensen, H. J. (1997). Open questions in the magnetic behaviour of high-temperature superconductors. *Rep. Prog. Phys.*, 60:1581.

Colaiori, F. and Moore, M. A. (2001). Upper critical dimension, dynamic exponent, and scaling functions in the mode-coupling theory for the kardar-parisi-zhang equation. *Phys. Rev. Lett.*, 86(18):3946–3949.

Cugliandolo, L. F., Kurchan, J., and Le Doussal, P. (1996). Large time out-of-equilibrium dynamics of a manifold in a random potential. *Phys. Rev. Lett.*, 76(13):2390–2393.

Devillard, P. and Stanley, H. E. (1989). Scaling properties of eden clusters in three and four dimensions. *Physica A*, 160(3):298–309.

Dong, M., Marchetti, M. C., Middleton, A. A., and Vinokur, V. (1993). Elastic string in a random potential. *Phys. Rev. Lett.*, 70(5):662–665.

Doussal, P. L. and Wiese, K. J. (2003). Functional renormalization group at large n for disordered elastic systems, and relation to replica symmetry breaking. *Phys. Rev. B*, 68(17):174202.

Duemmer, O. and Le Doussal, P. (2007). Chaos in the thermal regime for pinned manifolds via functional RG. *arXiv:0709.1378v1 [cond-mat.dis-nn]*.

Eden, M. (1961). *Proceedings of the Fourth Berkeley Symposium of Mathematical Statistics and Probability*. California Press, Berkeley.

Edwards, S. F. and Wilkinson, D. R. (1982). The surface statistics of a granular aggregate. *Proc. R. Soc. Lond A*, 381:17.

Family, F. (1986). Scaling of rough surfaces: effects of surface diffusion. *J. Phys. A*, 19:L441.

Family, F. (1990). Dynamic scaling and phase transitions in interface growth. *Physica A*, 168:561.

Family, F. and Vicsek, T. (1985). Scaling of the active zone in the eden process on percolation networks and the ballistic deposition model. *J. Phys. A*, 18:L75.

Fisher, D. S. (1986). Interface fluctuations in disordered systems: $5-\epsilon$ expansion and failure of dimensional reduction. *Phys. Rev. Lett.*, 56(18):1964–1967.

Fisher, D. S. and Huse, D. A. (1988). Equilibrium behavior of the spin-glass ordered phase. *Phys. Rev. B*, 38(1):386–411.

Fuchs, D. T., Zeldov, E., Tamegai, T., Ooi, S., Rappaport, M., and Shtrikman, H. (1998). Possible new vortex matter phases in $bi2sr2cacu2o8$. *Phys. Rev. Lett.*, 80(22):4971–4974.

Galluccio, S. and Zhang, Y.-C. (1995). Driven interfaces in quenched disorder at critical depinning. *Phys. Rev. E*, 51(3):1686–1689.

Garel, T. and Orland, H. (1997). Directed polymers in a random medium: A variational approach. *Phys. Rev. B*, 55(1):226–230.

Grüner, G. (1988). The dynamics of charge-density waves. *Rev. Mod. Phys.*, 60(4):1129–1181.

Guo, H., Grossmann, B., and Grant, M. (1990). Kinetics of interface growth in driven systems. *Phys. Rev. Lett.*, 64(11):1262–1265.

Halpin-Healy, T. (1989). Diverse manifolds in random media. *Phys. Rev. Lett.*, 62(4):442–445.

Halpin-Healy, T. and Zhang, Y.-C. (1995). Kinetic roughening phenomena, stochastic growth, directed polymers and all that. aspects of multidisciplinary statistical mechanics. *Phys. Reports*, 254:215.

Huse, D. A. and Henley, C. L. (1985). Pinning and roughening of domain walls in ising systems due to random impurities. *Phys. Rev. Lett.*, 54(25):2708–2711.

Huse, D. A., Henley, C. L., and Fisher, D. S. (1985). Huse, henley, and fisher respond. *Phys. Rev. Lett.*, 55(26):2924.

Ioffe, L. B. and Vinokur, V. M. (1987). Dynamics of interfaces and dislocations in disordered media. *J. Phys. C*, 20:6149.

Jensen, H. (1985). The fate of the elastic string: roughening near the depinning threshold. *J. Phys. A*, 28:1861.

Jullien, R. and Botet, R. (1985). Scaling properties of the surface of the eden model in d=2, 3, 4. *J. Phys. A*, 18:2279.

Kardar, M. (1985). Roughening by impurities at finite temperatures. *Phys. Rev. Lett.*, 55(26):2923.

Kardar, M., Parisi, G., and Zhang, Y.-C. (1986). Dynamic scaling of growing interfaces. *Phys. Rev. Lett.*, 56(9):889–892.

Kardar, M. and Zhang, Y.-C. (1987). Scaling of directed polymers in random media. *Phys. Rev. Lett.*, 58(20):2087–2090.

Kardar, M. and Zhang, Y.-C. (1989). Transfer matrix simulations of 2d-interfaces in three-dimensional random media. *Europhys. Lett.*, 8:233.

Kolton, A. B., Rosso, A., and Giamarchi, T. (2005a). Creep motion of an elastic string in a random potential. *Phys. Rev. Lett.*, 94(4):047002.

Kolton, A. B., Rosso, A., and Giamarchi, T. (2005b). Nonequilibrium relaxation of an elastic string in a random potential. *Phys. Rev. Lett.*, 95(18):180604.

Kolton, A. B., Rosso, A., Giamarchi, T., and Krauth, W. (2006). Dynamics below the depinning threshold in disordered elastic systems. *Phys. Rev. Lett.*, 97:057001.

Krug, J. (1987). Scaling relation for a growing interface. *Phys. Rev. A*, 36(11):5465–5466.

Krug, J. (1991). 1/f noise for driven interfaces. *Phys. Rev. A*, 44(2):R801–R804.

Larkin, A. and Ovchinnikov, Y. (1979). Pinning in type ii superconductors. *J. Low Temp. Phys.*, 34:409.

Le Doussal, P., Wiese, K., Raphael, E., and Golestanian, R. (2006). Can non-linear elasticity explain contact-line roughness at depinning? *Phys. Rev. Lett.*, 96:015702.

Lemerle, S., Ferré, J., Chappert, C., Mathet, V., Giamarchi, T., and Le Doussal, P. (1998). Domain wall creep in an ising ultrathin magnetic film. *Phys. Rev. Lett.*, 80(4):849–852.

Leschhorn, H. (1993). Interface depinning in a disordered medium-numerical results. *Physica A*, 195:324.

Leschhorn, H. (1996). Anisotropic interface depinning: Numerical results. *Phys. Rev. E*, 54(2):1313–1320.

Leschhorn, H. and Tang, L.-H. (1993). Comment on ''elastic string in a random potential''. *Phys. Rev. Lett.*, 70(19):2973.

Mandelbrot, B. (1998). *The fractal geometry of Nature*. W. H. Freeman, New York.

Maslov, S., Paczuski, M., and Bak, P. (1994). Avalanches and $1f$ noise in evolution and growth models. *Phys. Rev. Lett.*, 73(16):2162–2165.

Meakin, P., Ramanlal, P., Sander, L. M., and Ball, R. C. (1986). Ballistic deposition on surfaces. *Phys. Rev. A*, 34(6):5091–5103.

Mézard, M. and Parisi, G. (1991). Replica field theory for random manifolds. *J. Phys. I*, 1:809.

Moser, K., Wolf, D., and Kertész, J. (1991). Numerical solution of the kardar-parisi-zhang equation in one, two and three dimensions. *Physica A*, 178:215.

Müller, M., Gorokhov, D. A., and Blatter, G. (2001). Velocity-force characteristics of a driven interface in a disordered medium. *Phys. Rev. B*, 63(18):184305.

Narayan, O. and Fisher, D. S. (1993). Threshold critical dynamics of driven interfaces in random media. *Phys. Rev. B*, 48(10):7030–7042.

Nattermann, T. (1987). Interface roughening in systems with quenched random impurities. *Europhys. Lett.*, 4:1241.

Nattermann, T. (1990). Scaling approach to pinning: Charge density waves and giant flux creep in superconductors. *Phys. Rev. Lett.*, 64(20):2454–2457.

Nattermann, T., Shapir, Y., and Vilfan, I. (1990). Interface pinning and dynamics in random systems. *Phys. Rev. B*, 42(13):8577–8586.

Nattermann, T., Stepanow, S., Tang, L.-H., and Leschhorn, H. (1992). Dynamics of interface depinning in a disordered medium. *J. Phys. II (France)*, 2:1483.

Nattermann, T. and Tang, L.-H. (1992). Kinetic surface roughening. i. the kardar-parisi-zhang equation in the weak-coupling regime. *Phys. Rev. A*, 45(10):7156–7161.

Neshkov, N. (2000). Reinterpretation of a kardar-parisi-zhang equation-based classification. *Phys. Rev. E*, 61(5):6023–6026.

Paruch, P., Giamarchi, T., and Triscone, J.-M. (2005). Domain wall roughness in epitaxial ferroelectric $pbzr0.2ti0.8o3$ thin films. *Phys. Rev. Lett.*, 94(19):197601.

Plischke, M. and Rácz, Z. (1984). Active zone of growing clusters: Diffusion-limited aggregation and the eden model. *Phys. Rev. Lett.*, 53(5):415–418.

Ponson, L., Bonamy, D., and Bouchaud, E. (2006). Two-dimensional scaling properties of experimental fracture surfaces. *Phys. Rev. Lett.*, 96:035506.

Ramasco, J. J., López, J. M., and Rodríguez, M. A. (2000). Generic dynamic scaling in kinetic roughening. *Phys. Rev. Lett.*, 84(10):2199–2202.

Ramasco, J. J., López, J. M., and Rodríguez, M. A. (2006). Glassy dynamics, aging and temperature-induced avalanches in interface pinning at finite temperatures. *Europhys. Lett.*, 76:554.

Repain, V., Bauer, M., Jamet, J. P., Ferré, J., Mougin, A., Chappert, C., and Bernas, H. (2004). Creep motion of a magnetic wall: Avalanche size divergence. *Europhys. Lett.*, 68:460.

Rosso, A. and Krauth, W. (2002). Roughness at the depinning threshold for a long-range elastic string. *Phys. Rev. E*, 65(2):025101.

Schehr, G. and Le Doussal, P. (2004). Aging in the glass phase of a two-dimensional random periodic elastic system. *Phys. Rev. Lett.*, 93(21):217201.

Schehr, G. and Le Doussal, P. (2005). Functional renormalization for pinned elastic systems away from their steady states. *Europhys. Lett.*, 71:290.

Scheidl, S. and Vinokur, V. M. (1996). Hysteretic creep of elastic manifolds. *Phys. Rev. Lett.*, 77(23):4768–4771.

Schwartz, M. and Edwards, S. F. (1992). Nonlinear deposition: A new approach. *Europhys. Lett.*, 20:301–305.

Sibani, P. and Dall, J. (2003). Log-poisson statistics and full aging in glassy systems. *Europhys. Lett.*, 64:8.

Sibani, P. and Jensen, H. (2004). How a spin glass remembers; memory and rejuvenation from intermittency data: an analysis of temperature shifts. *J. Stat. Mech.*, P10013.

Sibani, P. and Littlewood, P. B. (1993). Slow dynamics from noise adaptation. *Phys. Rev. Lett.*, 71(10):1482–1485.

Sneppen, K. (1992). Self-organized pinning and interface growth in a random medium. *Phys. Rev. Lett.*, 69(24):3539–3542.

Sneppen, K. and Jensen, M. H. (1993). Sneppen and jensen reply. *Phys. Rev. Lett.*, 70(24):3833.

Szendro, I., López, J., and Rodríguez, M. (2008). Dynamics of perturbations in disordered chaotic systems. *Phys. Rev. E*, 78:036202.

Tang, L.-H., Kardar, M., and Dhar, D. (1995). Driven depinning in anisotropic media. *Phys. Rev. Lett.*, 74(6):920–923.

Tang, L.-H. and Leschhorn, H. (1992). Pinning by directed percolation. *Phys. Rev. A*, 45(12):R8309–R8312.

Tybell, T., Paruch, P., Giamarchi, T., and Triscone, J.-M. (2002). Domain wall creep in epitaxial ferroelectric $pb(zr0.2ti0.8)o3$ thin films. *Phys. Rev. Lett.*, 89(9):097601.

Vicsek, T. (1989). *Fractal Growth Phenomena*. World Scientific, Singapore and New Jersey.

Vinokur, V. M., Marchetti, M. C., and Chen, L.-W. (1996). Glassy motion of elastic manifolds. *Phys. Rev. Lett.*, 77(9):1845–1848.

Wolf, D. E. and Kertész, J. (1987). Surface width exponents for three- and four-dimensional eden growth. *Europhys. Lett.*, 4:651.

Young, A. P. (1998). *Spin Glasses and Random Fields*. World Scientific, Singapore and New Jersey.

Sociophysics (Part II)

Abrams, D. M. and Strogatz, S. H. (2003). Linguisticsmodelling the dynamics of language death. *Nature*, 424:900.

Axelrod, R. (1997). The dissemination of culture: A model with local convergence and global polarization. *J. Conflict. Resolut.*, 41(2):203.

Axelrod, R. and Hamilton, W. (1981). The evolution of cooperation. *Science*, 211(2):1390.

Axelrod, R. and Hamilton, W. (2005). *The evolution of Ethnocentrism*. Interscience, New York, NY, USA.

Babinec, P. (1997). Stochastic resonance in the weidlich model of public opinion formation. *Phys. Lett. A*, 225:179.

Barahona, M. and Pecora, L. M. (2002). Synchronization in small-world systems. *Phys. Rev. Lett.*, 89(5):054101.

Baxter, G. J., Blythe, R. A., Croft, W., and McKane, A. J. (2006). Utterance selection model of language change. *Phys. Rev. E*, 73:046118.

Behera, L. and Schweitzer, F. (2003). On spatial consensus formation: Is the sznajd model different from a voter model? *Int. J. Mod. Phys C.*, 14(10):1331.

Ben-Naim, E., Frachebourg, L., and Krapivsky, P. L. (1996). Coarsening and persistence in the voter model. *Phys. Rev. E*, 53(4):3078–3087.

Bernardes, A. T., Stauffer, D., and Kertész, J. (2002). Election results and the sznajd model on barabasi network. *Eur. Phys. J. B*, 25:123.

Bordogna, C. M. and Albano, E. (2007). Statistical methods applied to the study of opinion formation models: a brief overview and results of a numerical study of a model based on the social impact theory. *J. Phys.-Condens Mat.*, 19:065144.

Castellano, C., Fortunato, S., and Loretto, V. (2007). Statistical physics of social dynamics. *arXiv:0710.3256v1 [physics.soc-ph].*

Castellano, C., Marsili, M., and Vespignani, A. (2000). Nonequilibrium phase transition in a model for social influence. *Phys. Rev. Lett.*, 85(16):3536–3539.

Castellano, C., Vilone, D., and Vespignani, A. (2003). Incomplete ordering of the voter model on small-world networks. *Europhys. Lett.*, 63(1):153.

Chen, P. and Redner, S. (2005). Majority rule dynamics in finite dimensions. *Phys. Rev. E*, 71(3):036101.

Deffuant, G., Neau, D., Amblard, F., and Weisbuch, G. (2000). Mixing beliefs among interacting agents. *Adv. Comp. Sys.*, 3:87.

Dornic, I., Chaté, H., Chave, J., and Hinrichsen, H. (2001). Critical coarsening without surface tension: The universality class of the voter model. *Phys. Rev. Lett.*, 87(4):045701.

Fortunato, S. (2004). The sznajd consensus model with continuous opinions. *arXiv:cond-mat/0407353v1 [cond-mat.stat-mech].*

Galam, S. (1990). Social paradoxes of majority rule voting and renormalization group. *J. Stat. Phys.*, 61:943.

Galam, S. (2002). Minority opinion spreading in random geometry. *Eur. J. Phys. B*, 25:403.

Galam, S. (2003). Modelling rumors: the no plane pentagon french hoax case. *Physica A*, 320:571.

Galam, S. (2004). Contrarian deterministic effects on opinion dynamics: the hung elections scenario. *Physica A*, 333:453.

Galam, S. (2005). Local dynamics vs. social mechanisms: A unifying frame. *Europhys. Lett.*, 70:705.

Galam, S., Gefen, Y., and Shapir, Y. (1982). Sociophysics: a new approach of sociological collective behavior. *J. Math. Sociology*, 9:1.

Galam, S. and Moscovici, S. (1991). Towards a theory of collective phenomena - consensus and attitude changes in groups. *Eur. J. Soc. Psychol.*, 21:49.

Holyst, J. A., Kacperski, K., and Schweitzer, F. (2001). Social impact models of opinion dynamics. *Ann. Rev. Comp. Phys.*, 9:253.

Hong, H., Choi, M. Y., and Kim, B. J. (2002). Synchronization on small-world networks. *Phys. Rev. E*, 65(2):026139.

Klimek, P., Lambiotte, R., and Thurner, S. (2007). Opinion formation in laggard societies. *arXiv:0706.4058v1 [physics.soc-ph].*

Kohring, G. A. (1996). Ising models of social impact: The role of cumulative advantage. *J. de Phys. I*, 6:301.

Krapivsky, P. L. (1992). Kinetics of monomer-monomer surface catalytic reactions. *Phys. Rev. A*, 45(2):1067–1072.

Krapivsky, P. L. and Redner, S. (2003). Dynamics of majority rule in two-state interacting spin systems. *Phys. Rev. Lett.*, 90(23):238701.

Kuperman, M. and Zanette, D. (2002). Stochastic resonance in a model of opinion formation on small-world networks. *Eur. Phys. J. B*, 26:387.

Laguna, M., Abramson, G., and Zanette, D. (2003). Vector opinion dynamics in a model for social influence. *Physica A*, 329:459.

Latané, B. (1981). The psychology of social impact. *American Psychologist*, 36:343.

Ligget, T. M. (1985). *Interacting particle systems*. Spriger Verlag, New york, NY, USA.

Milroy, L. (1960). *Language and social networks*. Basil Blackwell, Oxford and New York, USA.

Mira, J. and Paredes, A. (2005). Interlinguistic similarity and language death dynamics. *Europhys. Lett.*, 69:1031.

Mobilia, M. and Redner, S. (2003). Majority versus minority dynamics: Phase transition in an interacting two-state spin system. *Phys. Rev. E*, 68:046106.

Moreira, A. A., Andrade, J. S., and Stauffer, D. (2001). Sznajd social model on square lattice with correlated percolation. *Int. J. Mod. Phys. C*, 12:39.

Neumann, J. V. (1966). *Theory of self-Reproducing Automata*. Illinois Univ. Press, Champaign, IL,USA.

Patriarca, M. and Leppänen, T. (2004). Modeling language competition. *Physica A*, 338:296.

Reynolds, C. W. (1987). Flocks, herds, and schools: A distributed behavioral model. *J. Computer Graphics*, 21:4.

Sánchez, J. R. (2004). A modified one-dimensional sznajd model. *arXiv:cond-mat/0408518v1 [cond-mat.stat-mech].*

Schat, C., Abramson, G., and Wio, H. S. (1991). Effusion of a dilute gas revisited - vankampen expansion. *Am. J. Phys.*, 59:357.

Schneider, J. J. (2004). The influence of contrarians and opportunists on the stability of a democracy in the sznajd model. *Int. J. Mod. Phys. C*, 15:659.

Schulze, C. (2003). Long-range interactions in sznajd consensus model. *Physica A*, 324:717.

Slanina, F. and Lavicka, H. (2003). Analytical results for the sznajd model of opinion formation. *Eur. Phys. J. B*, 35:279.

Sousa, A. O. (2005). Consensus formation on a triad scale-free network. *Physica A*, 348:701.

Stauffer, D. (2002). Percolation and galam theory of minority opinion spreading. *Int. J. Mod. Phys. C*, 13(7):975.

Stauffer, D., Castello, X., Eguiluz, V., and San Miguel, M. (2007). Microscopic abrams-strogatz model of language competition. *Physica A*, 374:835.

Stauffer, D. and Martins, J. S. (2004). Simulation of galam's contrarian opinions on percolative lattices. *Physica A*, 334:558.

Stauffer, D. and Schulze, C. (2005). Microscopic and macroscopic simulation of competition between languages. *Physics of Life Reviews*, 2:89.

Stauffer, D., Sousa, A. O., and De Oliveira, M. (2000). Generalization to square lattice of sznajd sociophysics model. *Int. J. Mod. Phys. C*, 11:1239.

Sutherland, W. (2003). Parallel extinction risk and global distribution of languages and species. *Nature*, 423:276.

Sznajd-Weron, K. and Sznajd, J. (2000). Opinion evolution in closed community. *Int. J. Mod. Phys. C*, 11(6):1157.

Sznajd-Weron, K. and Sznajd, J. (2005). Who is left, who is right? *Physica A*, 351:593.

Tessone, C. J., Toral, R., Amengual, P., Wio, H. S., and San Miguel, M. (2004). Neighborhood models of minority opinion spreading. *Eur. Phys. J. B.*, 39:535.

Ulam, S. (1960). *A collection of mathematical problems*. Interscience, New York, NY, USA.

van Kampen, N. (1981). *Stochastic Processes in Physics and Chemistry*. North Holland, Amsterdam.

Vazquez, F., Kaprivsky, P., and Redner, S. (2003). Constrained opinion dynamics: freezing and slow evolution. *J. Phys. A*, 36:L61.

Vazquez, F. and Redner, S. (2004). Ultimate fate of constrained voters. *J. Phys. A*, 37:8479.

Vazquez, F. and Redner, S. (2007). Non-monotonicity and divergent time scale in axelrod model dynamics. *Europhys. Lett.*, 78(1):18002.

Wang, W.-Y. and Minett, J. (2005). The invasion of language: emergence, change and death. *Trends in ecology and Evolution*, 20:263.

Watts, D. and Strogatz, S. (1998). Collective dynamics of 'small-world' networks. *Nature*, 393:440.

Weidlich, W. (1971). Statistical description of polarization phenomena in society. *Br. J. Math. Statis. Phychol.*, 24:251.

Weidlich, W. (1991). Physics and social-science - the approach of synergetics. *Phys. Rep*, 204:1.

Weidlich, W. (2002). *Sociodynamics-A systematic approach to mathematical modelling in social sciences*. Taylor & Francis, London.

Networks (Part III)

Abramson, G. and Kuperman, M. (2001). Social games in a social network. *Phys. Rev. E*, 63(3):030901.

Adamic, L. A., Lukose, R. M., and Huberman, B. A. (2003). Local search in unstructured networks. In Bornholdt, S. and Schuster, H. G., editors, *Handbook of Graphs and Nertworks*, pages 295–316. Willey-VCH.

Albert, R. and Barabási, A.-L. (2002). Statistical mechanics of complex networks. *Rev. Mod. Phys.*, 74:47.

Albert, R., Jeong, H., and Barabási, A.-L. (1999). Internet - diameter of the world-wide web. *Nature*, 401:130.

Amaral, L. A. N., Scala, A., Barthélémy, M., and Stanley, E. (2000). Classes of small-world networks. *PNAS*, 97:11149.

Arenas, A., Díaz-Guilera, A., and Guimera, R. (2001). Communication in networks with hierarchical branching. *Phys. Rev. Lett.*, 86:3196.

Arenas, A., Fernández, A., Fortunato, S., and Gómez, S. (2008). Motif-based communities in complex networks. *J. Phys. A*, 41:224001.

Barabási, A.-L. (2003). Emergence of scaling in complex networks. In Bornholdt, S. and Schuster, H. G., editors, *Handbook of Graphs and Nertworks*, pages 69–82. Willey-VCH.

Barabási, A.-L. and Albert, R. (1999). Emergence of scaling in random networks. *Science*, 286:509.

Barahona, M. and Pecora, L. M. (2002). Synchronization in small-world systems. *Phys. Rev. Lett.*, 89(5):054101.

Barrat, A. and Weigt, M. (2000). On the properties of small-world network models. *Eur. J. Phys. B*, 13:547.

Barrat, A. and Zecchina, R. (1999). Time scale separation and heterogeneous off-equilibrium dynamics in spin models over random graphs. *Phys. Rev. E*, 59(2):R1299–R1302.

Barthélemy, M. (2003). Comment on universal behavior of load distribution in scale-free networks. *Phys. Rev. Lett.*, 91(18):189803.

Barthélémy, M. and Amaral, L. A. N. (1999). Small-world networks: Evidence for a crossover picture. *Phys. Rev. Lett.*, 82(15):3180–3183.

Bilke, S. and Peterson, C. (2001). Topological properties of citation and metabolic networks. *Phys. Rev. E*, 64(3):036106.

Boettcher, S. and Percus, A. G. (2001). Optimization with extremal dynamics. *Phys. Rev. Lett.*, 86(23):5211–5214.

Bollobás, B. and Riordan, O. M. (2003). Mathematical results on scale-free random graphs. In Bornholdt, S. and Schuster, H. G., editors, *Handbook of Graphs and Nertworks*, pages 1–32. Willey-VCH.

Bornholdt, S. and Schuster, H. G., editors (2003). *Handbook of Graphs and Nertworks*. Willey-VCH.

Braunstein, L. A., Buldyrev, S. V., Cohen, R., Havlin, S., and Stanley, H. E. (2003). Optimal paths in disordered complex networks. *Phys. Rev. Lett.*, 91(16):168701.

Callaway, D. S., Newman, M. E. J., Strogatz, S. H., and Watts, D. J. (2000). Network robustness and fragility: Percolation on random graphs. *Phys. Rev. Lett.*, 85(25):5468–5471.

Cassi, D. (1996). Local vs average behavior on inhomogeneous structures: Recurrence on the average and a further extension of mermin-wagner theorem on graphs. *Phys. Rev. Lett.*, 76(16):2941–2944.

Catanzaro, M., Boguñá, M., and Pastor-Satorras, R. (2005). Generation of uncorrelated random scale-free networks. *Phys. Rev. E*, 71(2):027103.

Cohen, R., Erez, K., ben Avraham, D., and Havlin, S. (2001). Breakdown of the internet under intentional attack. *Phys. Rev. Lett.*, 86(16):3682–3685.

Cohen, R. and Havlin, S. (2003). Scale-free networks are ultrasmall. *Phys. Rev. Lett.*, 90(5):058701.

Cormen, T., Leiserson, C., Rivest, R., and Stein, C. (2005). *Introduction to Algorithms*. McGraw-Hill, Boston, MA, USA.

Danila, B., Yu, Y., Marsh, J. A., and Bassler, K. E. (2006). Optimal transport on complex networks. *Physical Review E (Statistical, Nonlinear, and Soft Matter Physics)*, 74(4):046106.

Dezső, Z. and Barabási, A.-L. (2002). Halting viruses in scale-free networks. *Phys. Rev. E*, 65(5):055103.

Ebel, H. and Bornholdt, S. (2002). Coevolutionary games on networks. *Phys. Rev. E*, 66(5):056118.

Erdős, P. and Rényi, A. (1959). On random graphs - I. *Publicationes Mathematicae*, 6:290.

Erdős, P. and Rényi, A. (1960). The evolution of random graphs. *Publications of the Mathematical Institute of the Hungarian Academy of Sciences*, 5:17.

Everitt, B. (1974). *Cluster Analysis*. John Wiley, New York, NY, USA.

Ferrer i Cancho, R. and Solé, R. V. (2001). The small world of human language. *Proc. Roy. Soc., London*, 268:2261.

Goh, K.-I., Kahng, B., and Kim, D. (2001). Universal behavior of load distribution in scale-free networks. *Phys. Rev. Lett.*, 87(27):278701.

Goh, K.-I., Noh, J. D., Kahng, B., and Kim, D. (2005). Load distribution in weighted complex networks. *Phys. Rev. E*, 72(1):017102.

Guimerà, R., Arenas, A., Díaz-Guilera, A., and Giralt, F. (2002a). Dynamical properties of model communication networks. *Phys. Rev. E*, 66(2):026704.

Hong, H., Choi, M. Y., and Kim, B. J. (2002). Synchronization on small-world networks. *Phys. Rev. E*, 65(2):026139.

Jacobson, V. (1988). Congestion avoidance and control. *Comp. Comm. Rev.*, 18:314.

Jeong, H., Mason, S. P., Oltvai, S. N., and Barabási, A.-L. (2001). Lethality and centrality in protein networks. *Nature*, 411:41.

Kalisky, T., Braunstein, L. A., Buldyrev, S. V., Havlin, S., and Stanley, H. E. (2005). Scaling of optimal-path-lengths distribution in complex networks. *Phys. Rev. E*, 72(2):025102.

Keeling, M. (1999). The effects of local spatial structure on epidemiological invasions. *Proc. Roy. Soc. Lond. B*, 266:859–869.

Kim, B. J., Trusina, A., Holme, P., Minnhagen, P., Chung, J. S., and Choi, M. Y. (2002a). Dynamic instabilities induced by asymmetric influence: Prisoners' dilemma game in small-world networks. *Phys. Rev. E*, 66(2):021907.

Kim, J., Krapivsky, P. L., Kahng, B., and Redner, S. (2002b). Infinite-order percolation and giant fluctuations in a protein interaction network. *Phys. Rev. E*, 66(5):055101.

Kleinberg, J. M. (2000). Navigation in a small world - it is easier to find short chains between points in some networks than others. *Nature (London)*, 406:845.

Kleinberg, J. M., Kumar, R., Raghavan, P., Rajagopalan, S., and Tomkins, A. (1999). *Proc. Internac. Conf. on Combinatorics and Computing. Lecture Notes in Computer Science.* Springer, Berlin.

Kottos, T. and Smilansky, U. (1997). Quantum chaos on graphs. *Phys. Rev. Lett.*, 79(24):4794–4797.

Krapivsky, P. L. and Redner, S. (2001). Organization of growing random networks. *Phys. Rev. E*, 63(6):066123.

Krapivsky, P. L. and Redner, S. (2005). Network growth by copying. *Phys. Rev. E*, 71(3):036118.

Kuperman, M. and Abramson, G. (2001). Small world effect in an epidemiological model. *Phys. Rev. Lett.*, 86(13):2909–2912.

Lago-Fernández, L. F., Huerta, R., Corbacho, F., and Sigüenza, J. A. (2000). Fast response and temporal coherent oscillations in small-world networks. *Phys. Rev. Lett.*, 84(12):2758–2761.

Lancichinetti, A., Fortunato, S., and Radicchi, F. (2008). Benchmark graphs for testing community detection algorithms. *Phys. Rev. E*, 78:046110.

Liljeros, F., Edling, C. R., Amaral, L. A. N., Stanley, H. E., and Aberg, Y. (2001). The web of human sexual contacts. *Nature*, 411:907.

Maslov, S. and Sneppen, K. (2002). Specificity and stability in topology of protein networks. *Science*, 296:910.

Maslov, S., Sneppen, K., and Zaliznyal, A. (2004). Pattern detection in complex networks: Correlation profile of the internet. *Physica A*, 333:529.

Milgram, S. (1967). Small-world problem. *Psychol. Today*, 1:61.

Molloy, M. and Reed, B. (1995). A critical-point for random graphs with a given degree sequence. *Random Structures and Algorithms*, 6:161.

Moukarzel, C. F. (1999). Spreading and shortest paths in systems with sparse long-range connections. *Phys. Rev. E*, 60(6):R6263–R6266.

Nagel, K. and Paczuski, M. (1995). Emergent traffic jams. *Phys. Rev. E*, 51(4):2909–2918.

Nagel, K. and Schreckenberg, M. (1992). A cellular automaton model for freeway traffic. *Journal de Physique I*, 2:2221.

Newman, M. E. J. (2001). Scientific collaboration networks. ii. shortest paths, weighted networks, and centrality. *Phys. Rev. E*, 64(1):016132.

Newman, M. E. J. (2002). Assortative mixing in networks. *Phys. Rev. Lett.*, 89(20):208701.

Newman, M. E. J. (2003). The structure and function of complex networks. *SIAM Review*, 45:167.

Newman, M. E. J. (2008). The physics of networks. *Physics Today*, Nov.:33.

Newman, M. E. J., Strogatz, S. H., and Watts, D. J. (2001). Random graphs with arbitrary degree distributions and their applications. *Phys. Rev. E*, 64(2):026118.

Ohira, T. and Sawatari, R. (1998). Phase transition in a computer network traffic model. *Phys. Rev. E*, 58(1):193–195.

Park, K., Lai, Y.-C., and Ye, N. (2004). Characterization of weighted complex networks. *Phys. Rev. E*, 70(2):026109.

Pastor-Satorras, R., Vázquez, A., and Vespignani, A. (2001). Dynamical and correlation properties of the internet. *Phys. Rev. Lett.*, 87(25):258701.

Pastor-Satorras, R. and Vespignani, A. (2001). Epidemic spreading in scale-free networks. *Phys. Rev. Lett.*, 86(14):3200–3203.

Pastor-Satorras, R. and Vespignani, A. (2003). Epidemics and immunization in scale-free networks. In Bornholdt, S. and Schuster, H. G., editors, *Handbook of Graphs and Nertworks*, pages 111–128. Willey-VCH.

Pollner, P., Palla, G., and Vicsek, T. (2006). Preferential attachment of communities: The same principle, but a higher level. *Europhys. Lett.*, 73:478.

Porto, M., Schwartz, N., Havlin, S., and Bunde, A. (1999). Optimal paths in disordered media: Scaling of the crossover from self-similar to self-affine behavior. *Phys. Rev. E*, 60(3):R2448–R2451.

Price, D. J. S. (1976). A general theory of bibliometric and other cumulative advantage processes. *J. Amer. Soc. Inform. Sci.*, 27:292.

Ravasz, E. and Barabási, A.-L. (2003). Hierarchical organization in complex networks. *Phys. Rev. E*, 67(2):026112.

Sánchez, A. D., López, J. M., and Rodríguez, M. A. (2002). Nonequilibrium phase transitions in directed small-world networks. *Phys. Rev. Lett.*, 88(4):048701.

Soffer, S. N. and Vázquez, A. (2005). Network clustering coefficient without degree-correlation biases. *Phys. Rev. E*, 71(5):057101.

Solé, R. V. and Pastor-Satorras, R. (2003). Complex networks in genomics and proteomics. In Bornholdt, S. and Schuster, H. G., editors, *Handbook of Graphs and Nertworks*, pages 145–167. Willey-VCH.

Solé, R. V. and Valverde, S. (2001). Information transfer and phase transitions in a model of internet traffic. *Physica A*, 289:595.

Sreenivasan, S., Cohen, R., López, E., Toroczkai, Z., and Stanley, H. E. (2007). Structural bottlenecks for communication in networks. *Physical Review E (Statistical, Nonlinear, and Soft Matter Physics)*, 75(3):036105.

Tlalka, M., Hensman, D., Darrah, P. R., Watkinson, S. C., and Fricker, M. D. (2003). Noncircadian oscillations in amino acid transport have complementary profiles in assimilatory and foraging hyphae of phanerochaete velutina. *New Phytol.*, 158:325.

Vazquez, A., Flammini, A., and Maritan, A. Vespignani, A. (2003). Modeling of protein interaction networks. *ComPlexUs*, 1.

Vázquez, A., Pastor-Satorras, R., and Vespignani, A. (2002). Large-scale topological and dynamical properties of the internet. *Phys. Rev. E*, 65(6):066130.

Watts, D. and Strogatz, S. (1998). Collective dynamics of 'small-world' networks. *Nature*, 393:440.

Watts, D. J., Dodds, P. S., and Newman, M. E. J. (2002). Identity and search in social networks. *Science*, 296:1302.

Weigt, M. and Hartmann, A. K. (2001). Typical solution time for a vertex-covering algorithm on finite-connectivity random graphs. *Phys. Rev. Lett.*, 86(8):1658–1661.

Wu, Z., Braunstein, A., Colizza, V., Cohen, R., Havlin, S., and Stanley, H. E. (2006). Optimal paths in complex networks with correlated weights: The worldwide airport network. *Phys. Rev. E*, 74:056104.

Yan, G., Zhou, T., Hu, B., Fu, Z.-Q., and Wang, B.-H. (2006). Efficient routing on complex networks. *Physical Review E (Statistical, Nonlinear, and Soft Matter Physics)*, 73(4):046108.

Zhanga, Z. and Zhou, S. (2007). Correlations in random apollonian network. *Physica A*, 380:621.